JETP Letters, Vol. 73, No. 5, 2001, pp. 209–213. Translated from Pis'ma v Zhurnal Éksperimental'noĭ i Teoreticheskoĭ Fiziki, Vol. 73, No. 5, 2001, pp. 243–247.

Self-Organization and 1/*f* Noise in Granular Superconductors

S. L. Ginzburg and N. E. Savitskaya

Institute of Nuclear Physics, Russian Academy of Sciences, Gatchina, Leningradskaya region, 188300 Russia

Received February 5, 2001

The interplay between the widespread phenomena such as 1/*f* noise and self-organization of the critical state is studied both theoretically and by computer simulation using a model of multijunction SQUID exposed to an external magnetic field. It is demonstrated that the spectra of the average current in the systems of different size exhibit a broad region of 1/*f* noise limited only by the system size. However, the coexistence of 1/*f* noise and self-organization of the critical state was observed only in one two-dimensional system. © *2001 MAIK "Nauka/Interperiodica".*

PACS numbers: 74.40.+k; 05.65.+b

1/*f* noise is known to be among the most abundant phenomena in nature. It is present in the spectra of diversified processes such as quasar light, river flow, music, speech, electrotechnical measurements, etc. However, in spite of its abundance, the origin of this phenomenon is still not clearly understood. To explain it, the concept of self-organized criticality (SOC) was suggested in [1].

According to this concept, giant dissipative dynamical systems consisting of a large number of mutually interacting elements are capable of accumulating small external perturbations to come, under their action, to the critical state. Every new perturbation removes the system from the state it came to and initiates a dynamical process (avalanche) that releases a part of the energy so that the system reenters the critical state, whose local characteristics, however, strongly fluctuate. Such systems never attain equilibrium but undergo transitions from one metastable critical state to another. The set of such metastable states mutually transforming via avalanches is called the self-organized critical state. A power-low distribution of the avalanche sizes in the system is considered the mathematical criterion for self-organization.

This type of behavior is also widespread in nature and occurs, in particular, in geological systems, where the earthquake intensity distribution also obeys the power law; in biology (population growth dynamics); etc. For this reason, the originators of the SOC concept have advanced the assumption that complex natural sources of 1/*f* noise are in the self-organized critical state.

However, subsequent investigations have revealed that the spectra of main characteristics in the standard mathematical models of self-organized systems such as the sandpile model [1, 2] or model [3] show the $1/f^{\alpha}$ dependence, where α is usually close to two. Nevertheless, because of the relative simplicity of these mathematical models, they have come into use as basic models for simulating systems with 1/*f* noise. For example, a modification of the perturbation rules gave rise to 1/*f* noise in a quasi-one-dimensional sandpile model [4] or in the nonconservative model [5]. However, in all these cases the critical state of the system was not self-organized. Therefore, the question of interplay between self-organization and 1/*f* noise is still open, so that a search for the systems in which these two phenomena can coexist is being continued, because it may clarify the mechanisms responsible for the 1/*f* noise.

Earlier, we demonstrated [6–10] that granular superconductors with the large parameter $V \sim j_c a^3/\Phi_0$ (a is the grain size, j_c is the critical current density in the intergrain junctions, and Φ_0 is the magnetic flux quantum) represent an interesting example of systems with self-organization. Due to their physical properties, these systems can be used for studying the self-organization phenomena under conditions that are physically unreasonable for the previously suggested systems with SOC but are natural to granular superconductors. This allowed us to assume that granular superconductors are precisely the ones which can be used for studying the interplay between 1/*f* noise and self-organization.

The purpose of this work was to study the above interplay for the critical state of a multijunction SQUID exposed to an increasing external magnetic field. For each avalanche appearing in the critical state of the system, we examined its characteristics such as the integrated avalanche voltage, which is an analogue of the avalanche size in the SOC models, and the average current at the end of the avalanche. In addition to the distribution of integrated voltages, the interavalanche current correlations were also considered. A detailed study of the systems differing in size has shown that the spectra of average current in the quasi-one-dimensional

0021-3640/01/7305-0209$21.00

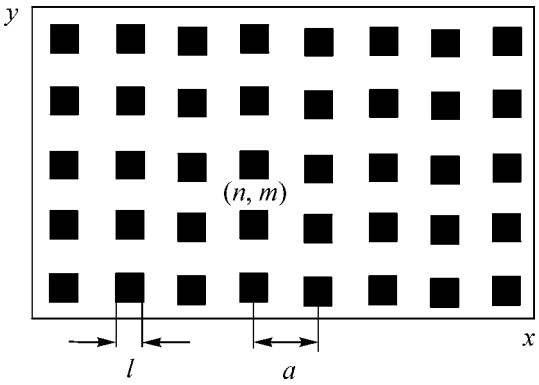

Fig. 1. (x, y) Cross section of a two-dimensional multijunction SQUID.

case exhibit a broad region of $1/f$ noise limited only by the system size. However, the critical state is not self-organized in this case. As for the two-dimensional case, $1/f$ noise and self-organization were found to coexist in the system.

The multijunction SQUID considered in this work consists of two superconducting plates connected together by Josephson junctions at the sites of an $N \times M$ lattice. The junction size l is much smaller than the lattice spacing a (Fig. 1). The external magnetic field H^{ext} is aligned with the y axis. The current in this geometry flows along the z axis. The system of equations for the gauge-invariant phase differences $\varphi_{n,m}$ at the junctions with coordinates (na, ma) can be written based on the equation for a large Josephson junction [11]. Using the resistive model of a Josephson junction without thermal fluctuations [12], we obtain the following dimensionless system of equations:

$$V\sin\varphi_{n,m} + \tau\frac{d\varphi_{n,m}}{dt} = \varphi_{n+1,m}$$

$$+ \varphi_{n-1,m} + \varphi_{n,m-1} + \varphi_{n,m+1} - 4\varphi_{n,m},$$

$$n \neq 1, N; \quad m \neq 1, M;$$

$$V\sin\varphi_{1,m} + \tau\frac{d\varphi_{1,m}}{dt} = \varphi_{2,m} + \varphi_{1,m-1}$$

$$+ \varphi_{1,m+1} - 3\varphi_{1,m} - \frac{4\pi\lambda_L a}{\Phi_0}H^{\text{ext}}_{1,m},$$

$$m \neq 1, M;$$

$$V\sin\varphi_{N,m} + \tau\frac{d\varphi_{N,m}}{dt} = \varphi_{N-1,m} + \varphi_{N,m-1} \quad (1)$$

$$+ \varphi_{N,m+1} - 3\varphi_{N,m} + \frac{4\pi\lambda_L a}{\Phi_0}H^{\text{ext}}_{N,m},$$

$$m \neq 1, M;$$

$$V\sin\varphi_{N,M} + \tau\frac{d\varphi_{N,M}}{dt}$$

$$= \varphi_{N-1,M} + \varphi_{N,M-1} - 2\varphi_{N,M} + \frac{4\pi\lambda_L a}{\Phi_0}H^{\text{ext}}_{N,M},$$

$$V = \frac{2\pi j_c}{j_\varphi}, \quad j_\varphi = \frac{\Phi_0}{8\pi l^2\lambda_L}, \quad \tau = \frac{\Phi_0}{\rho_0 j_\varphi},$$

where j_c is the critical current density, λ_L is the London penetration depth, Φ_0 is the magnetic flux quantum, ρ_0 is the surface resistance of the junction, and $j_{en,m}$ is the density of the injection current.

One can see from these equations that the increasing external magnetic field induces a negative current at the left boundary of the system and a positive current of the same magnitude at its right boundary. We assume in this work that currents of opposite signs are not injected into all junctions of the left and right boundaries simultaneously but every time into a single randomly chosen junction at each of the boundaries; i.e., $H^{\text{ext}}_{1,m_0} = H^{\text{ext}}_{N,m_1} = H^{\text{ext}}$, where m_0 and m_1 are random independent variables, and $H^{\text{ext}}_{1,m} = H^{\text{ext}}_{N,m} = 0$ for all $m \neq m_0$ and m_1. It should also be noted that the system is closed; i.e., the current is conserved.

This system, together with the method of perturbation described above, was analyzed in detail in [8, 10], where it was demonstrated that, although the system is closed, its critical state is self-organized.

We studied this system by computer simulation using the Eulerian scheme with a step of $dt = 0.01$ and $V = 40$ in the regime that is ordinarily applied to systems with self-organization. Starting with the state for which all $\varphi_i = 0$, we perturbed the system by increasing the magnetic field. The injection of a current into the system initiated an avalanche, which manifested itself as a voltage pulse. Every next injection was done only after the system had come to the metastable state.

After a certain transient period, the system attained its critical state. The latter represented a set of metastable states in which the junction currents in the right part of the system were positive and close to the critical value while the currents in the left part were negative and close to the negative critical value. The junction currents fluctuated upon the transition from one metastable state to another, but the structure of the critical state remained unchanged.

For each avalanche in the critical state, we calculated a current averaged over the "positive" part of the

system at the end of the avalanche

$$z_i = \frac{1}{N_1 M}\sum_{n=N_1}^{N}\sum_{m=1}^{M} z^{st}_{n,m}(t_{ei}),$$
$$z^{st}_{n,m} = V/2\pi\sin\varphi_{n,m}(t_{ei}), \quad (2)$$

where t_{ei} is the time of the end of the ith avalanche and $N_1 = (N-1)/2 + 2$. We also calculated a voltage averaged over the positive part of the system and integrated over the avalanche time to obtain the quantity analogous to the avalanche size in the previously considered models with SOC:

$$U_i = \frac{\Phi_0}{2\pi N_1 M}\sum_{n=N_1}^{N}\sum_{m=1}^{M}[\varphi_{n,m}(t_{ei}) - \varphi_{n,m}(t_{bi})], \quad (3)$$

where t_{bi} is the time of the beginning of the ith avalanche.

We characterized the system by the probability density $\rho(U)$ of integrated voltages

$$\rho(U) = \langle\delta(U - U_i)\rangle, \quad (4)$$

and by the spectral densities $S_z(f)$ of average currents [13]

$$S_z(f) = 2\sum_{j=-\infty}^{\infty} D_z(j)e^{-i2\pi fj}, \quad (5)$$

$$D_z(j) = \langle z_i z_{i+j}\rangle - \langle z\rangle^2. \quad (6)$$

Here, $\langle\ldots\rangle$ stands for the averaging over the avalanche number i.

It should be emphasized once more that the correlation functions and, hence, the spectral densities of the quantities are taken with respect to the avalanche number i rather than to time t; i.e., we consider the interavalanche correlations in the system. The importance of these characteristics was discussed in [7].

We considered our system for different M and N equal to 43. The magnitude of a current injected per one step into the right and left boundaries is unity unless otherwise stated. The results are presented in the figures.

As was already shown in [1], neither self-organization nor $1/f$ noise is present in the one-dimensional case ($M = 1$). After each perturbation, the system reenters the same (the only) critical state and the avalanches are either of zero or of a certain fixed size U_0. The spectra in this case are delta-shaped.

We next considered the quasi-one-dimensional case $N \gg M$. It is seen from the figures that the spectral densities of average current have a broad region of $1/f$ noise limited only by the system size M. In particular, it was maximal for $M = 2$ (Fig. 2b). However, self-organization did not occur in these cases and only a finite set of avalanches with fixed sizes and quasi-periodic behavior was observed (Fig. 2a).

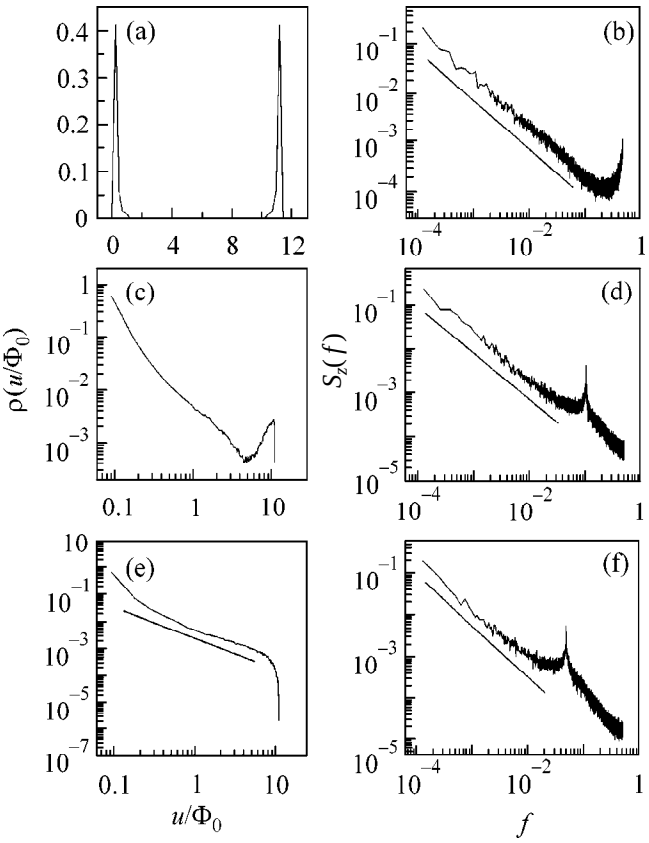

Fig. 2. Results of computer simulation of the systems with different M and $N = 43$. (a) Probability density $\rho(u/\Phi_0)$ for $M = 2$. (b) Spectral density of the average current for $M = 2$; the slope of the straight line $\alpha = -1.00$. (c) Probability density $\rho(u/\Phi_0)$ for $M = 10$. (d) Spectral density of the average current for $M = 10$; the slope of the straight line $\alpha = -1.05$. (e) Probability density $\rho(u/\Phi_0)$ for $M = 21$; the slope of the straight line $\alpha_1 = -1.01$. (f) Spectral density of the average current for $M = 21$; the slope of the straight line $\alpha = -1.05$.

As M further increased ($N > M$), avalanches of different sizes appeared in the system, but $1/f$ noise persisted (Figs. 2c, 2d).

It is seen in Figs. 2e and 2f that the system becomes self-organized, with the persistence of $1/f$ noise, at $M = (N-1)/2$. We already observed this situation in [8], but did not analyze it in more detail.

To demonstrate pictorially what the presence of $1/f$ noise means, we also calculated, in addition to the spectral density $S_z(f)$, the interavalanche correlation function $D_z(j)$ for the average current [Eq. (6)]. Figures 3a, 3b, and 3c show the $D_z(j)$ function for different M. In all cases, the oscillations with a frequency of $1/M$ are clearly seen and produce a peak at this frequency in the spectral functions of the process. In all cases considered, an exceedingly slow logarithmic decrease is the most prominent feature of the correlation functions. For instance, $D_z(j) \approx D_z(0)/(1 + 0.33\ln(j))$ for $M = 2$; i.e., $D_z(j) \approx D_z(0)/3$ for $j = 10^3$.

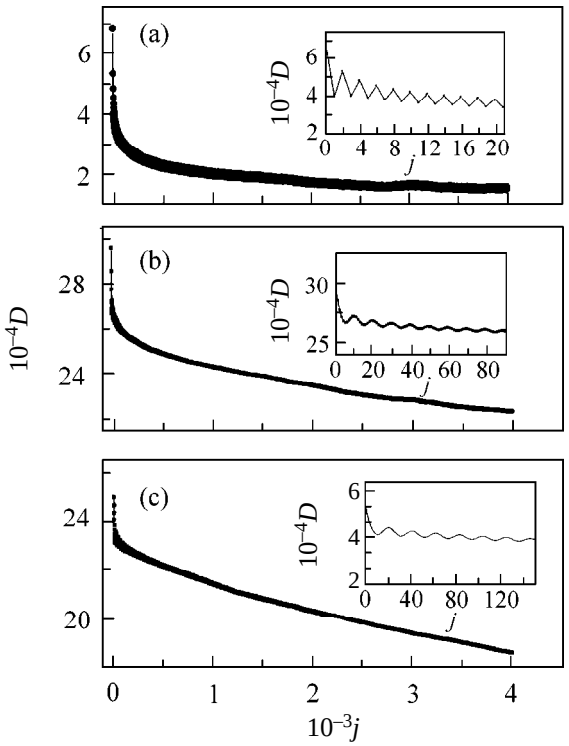

Fig. 3. Interavalanche correlation functions for the average current in the systems with different M and $N = 43$; $M =$ (a) 2, (b) 10, and (c) 21. Insets: enlarged fragments of $D_z(j)$; oscillations with frequency $f = 1/M$ are clearly visible.

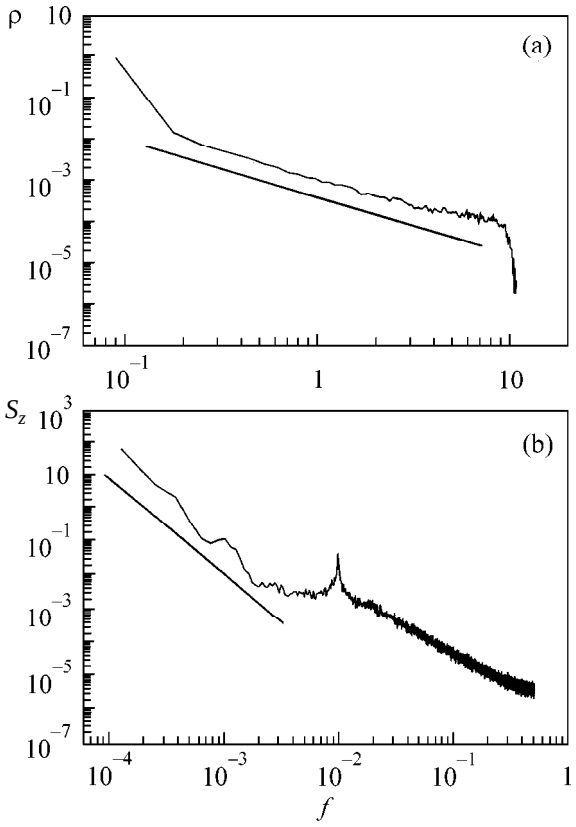

Fig. 4. Results of computer simulation of the 43×21 system; the magnitude of the current injected into each boundary is 0.2. (a) Probability density $\rho(u/\Phi_0)$; the slope of the straight line $\alpha = -1.01$. (b) Spectral density of the average current; the slope of the straight line $\alpha_1 \approx -2.8$.

Thus, it is seen from the figures that the z_i values for the metastable states separated by thousands of avalanches strongly correlate with each other. Moreover, not only the z_i values but also the overall structure of these states change slowly, as was already pointed out in [4]. Therefore, the system possesses a long-time memory, which is to say that mixing is absent in the system and it is nonergodic.

Note in conclusion that the coexistence of $1/f$ noise and self-organization in the system is highly unstable against variations in the method of external action. For example, $1/f$ noise disappears, whereas the self-organization is retained upon a change in the magnitude of the current injected into the boundaries (Fig. 4).

In summary, this work presents a detailed study of the interavalanche correlations of the average current and voltage in the critical state of multijunction $N \times M$ SQUIDs exposed to an increasing external magnetic field. The main results can be formulated as follows.

In all cases considered, the spectra of average current exhibit a broad region of $1/f$ noise limited only by the system size M, indicating the presence of long-time interavalanche correlations in the system, i.e., its nonergodicity.

The self-organized critical state was observed for one two-dimensional system with integer addition. The coexistence of $1/f$ noise and self-organization in the same system is highly unstable against the variations of external conditions, suggesting that these two phenomena are mutually exclusive in practice.

We thank O.V. Gerashchenko and M.A. Pustovoĭt for valuable remarks. This work was supported by the Russian Foundation for Basic Research (project no. 99-02-17545), the Scientific Council of the "Superconductivity" direction of the program "Topical Directions in Physics of Condensed Media" (project no. 96021 "Profile"), the subprogram "Statistical Physics" of the State Scientific and Technical program "Physics of Quantum and Wave Processes" (project no. VIII-3), the State program "Neutron Studies of Matter," and (in part) the Russian Foundation for Basic Research (project no. 00-15-96610).

REFERENCES

1. P. Bak, C. Tang, and K. Wisenfeld, Phys. Rev. Lett. **59**, 381 (1987).
2. D. Dhar, Phys. Rev. Lett. **64**, 1613 (1990).
3. Y.-C. Zhang, Phys. Rev. Lett. **63**, 470 (1989).
4. S. Maslov, C. Tang, and Y.-C. Zhang, Phys. Rev. Lett. **83**, 2449 (1999).

5. P. De Los Rios and Y.-C. Zhang, Phys. Rev. Lett. **82**, 472 (1999).
6. S. L. Ginzburg, Zh. Éksp. Teor. Fiz. **106**, 607 (1994) [JETP **79**, 334 (1994)].
7. S. L. Ginzburg, M. A. Pustovoit, and N. E. Savitskaya, Phys. Rev. E **57**, 1319 (1998).
8. S. L. Ginzburg and N. E. Savitskaya, Pis'ma Zh. Éksp. Teor. Fiz. **69**, 119 (1999) [JETP Lett. **69**, 133 (1999)].
9. S. L. Ginzburg and N. E. Savitskaya, Pis'ma Zh. Éksp. Teor. Fiz. **68**, 688 (1998) [JETP Lett. **68**, 719 (1998)].
10. S. L. Ginzburg and N. E. Savitskaya, Zh. Éksp. Teor. Fiz. **117**, 227 (2000) [JETP **90**, 202 (2000)].
11. O. I. Kulik and I. K. Yanson, *Josephson Effect in the Superconducting Tunnel Structures* (Nauka, Moscow, 1970).
12. K. K. Likharev, *Introduction to the Dynamics of Josephson Junctions* (Nauka, Moscow, 1985).
13. J. Bendat and A. Piersol, *Random Data. Analysis and Measurement Procedures* (Wiley, New York, 1986; Mir, Moscow, 1989).

Translated by V. Sakun

JETP Letters, Vol. 73, No. 5, 2001, pp. 214–218. Translated from Pis'ma v Zhurnal Éksperimental'noĭ i Teoreticheskoĭ Fiziki, Vol. 73, No. 5, 2001, pp. 248–252.

Rozhdestvenski Hooks in Two-Photon Parametric Light Scattering

D. Yu. Korystov, S. P. Kulik, and A. N. Penin

Faculty of Physics, Moscow State University, Vorob'evy gory, Moscow, 119899 Russia

Received February 8, 2001

The interference of spontaneous parametric radiation was observed from two nonlinear crystals separated by a macroscopic layer of a linear substance and excited by a common pump beam. In the presence of strong dielectric dispersion in the layer, the frequency–angular spectra display features analogous to the Rozhdestvenski hooks. The hook wavelength corresponds to the compensation of group velocity dispersions in the nonlinear crystals and the layer. *© 2001 MAIK "Nauka/Interperiodica".*

PACS numbers: 42.50.Dv; 42.70.Mp

By now, a number of experimental procedures are known for the observation of the interference of two-photon (biphoton) radiation in either the second or fourth order in field [1]. Such an interference underlies many effects in quantum optics [2]. Because of the lack of adequate classical analogues of the biphoton states of the electromagnetic field, two-photon interference (TI) has found a purely quantum interpretation. Indeed, some experimentally detected quantities have values that are basically unattainable in the classical experiments. At the same time, a qualitative comparison of the classical and quantum optical interference effects reveals many common regularities. In some cases, the known analogues serve as the only "bridges" connecting the quantum and classical worlds at a level of interpretation of the experimental results [3].

In this work, the distortion effect observed in the interference pattern at frequencies close to the absorption band of a layer placed between two crystals spontaneously radiating photon pairs is discussed. Such distortions are caused by a phenomenon that was first employed by Rozhdestvenski in 1912 in his hook method. This elegant method was later used for the accurate quantitative investigation of anomalous dispersion in metal vapors [4].

Spontaneous parametric light scattering (SPS) in crystals with quadratic susceptibility is a source of two-photon radiation [5]. The SPS can be interpreted as resulting from the decay of pump photons with frequency ω_p into pairs of correlated photons with frequencies ω_s and ω_i, according to the scheme $\hbar\omega_p \longrightarrow \hbar\omega_s + \hbar\omega_i$, in a crystal with quadratic susceptibility $\chi^{(2)}$. In the case of a homogeneous crystal and a plane monochromatic pump wave, the spontaneous radiation of photon pairs occurs predominantly in the directions determined by the stationarity $\omega_s + \omega_i - \omega_p = 0$ and spatial homogeneity $\Delta\mathbf{k} \equiv \mathbf{k}_s + \mathbf{k}_i - \mathbf{k}_p = 0$ conditions [$\mathbf{k}_j$ ($j = s$, i, and p) are the wave vectors of the signal (s), idler (i), and pump (p) modes inside the crystal]. These expressions, called matching conditions, together with the dispersion law $\omega(\mathbf{k})$ of the crystal, define the relation $\theta_s = \theta_s(\omega_s)$ between the frequencies and angles of the scattered radiation. The presence of spatial inhomogeneity in the scattering volume materially alters the frequency–angular SPS spectrum.

Let the biphotons be emitted from two identical plane nonlinear crystals separated by a layer of a transparent substance (Fig. 1). Then the dependence of the scattering line shape (i.e., of the normalized intensity) on the scattering angle and frequency is determined from the condition

$$g_0(\theta_s, \omega_s) = \left[\frac{\sin(\delta/2)}{\delta/2}\cos\left(\frac{\delta+\delta'}{2}\right)\right]^2, \qquad (1)$$

where δ and δ' are the wave detunings in the nonlinear crystal and the layer, respectively,

$$\begin{aligned}\delta(\omega_s, \theta_s) &= \Delta L = (k_p - k_s - k_i)L,\\ \delta'(\omega_s, \theta_s) &= \Delta' L' = (k'_p - k'_s - k'_i)L',\end{aligned} \qquad (2)$$

θ_s is the angle inside the crystal, and k_j and k'_j are the projections of the wave vectors onto the direction perpendicular to the layers. Equation (1) is derived without regard for absorption in the intermediate layer. The function $g(\theta_s, \omega_s)$ is proportional to the square of the modulus of the biphoton amplitude

$$\left|F_{k_s k_i}\right|^2 = g(\theta_s, \omega_s)\left\{\frac{2\pi}{c}E_p m L \chi^{(2)}\right\}^2 \omega_s \omega_i,$$

which determines the contribution of the two-photon Fock's states to the wave function of the SPS field for a given pump field E_p [6] ($m = 2$ is the number of nonlinear crystals). Equation (1) describes the TI effect in the

second order in field [7]; the phase incursions of all three modes in the intermediate layer L' modulate the line shape following the law $\cos^2[(\delta + \delta')/2]$. According to Eq. (1), spontaneous radiation is fully suppressed for some frequencies and angles. Since the dispersion properties of the intermediate layer influence only the modulation multiplier, the TI can be used for determining the dispersion law for the substance placed between the crystals [8, 9]. The distinguishing feature of such spectroscopy is that the scattering intensity is determined by the nonlinear SPS process, whereas the interference modulation is driven by the phase incursion in the layer, where, in the general case, $\chi^{(2)} = 0$; i.e., the substance may be linear.

By expressing the wave detunings δ and δ' explicitly in terms of frequencies and angles [8], one can determine the condition under which the slopes of the interference maxima ($\delta + \delta' = 2\pi m$) are zero, i.e., $\partial\vartheta_s/\partial\omega_s = 0$, where ϑ is the external (observed) scattering angle:

$$\frac{\partial\vartheta_s}{\partial\omega_s} = \frac{(\tau_s - \tau_i) + (\tau_s' - \tau_i')}{\vartheta_s\left(\frac{\omega_s}{c}\right)^2\left\{L\left(\frac{1}{k_s} + \frac{1}{k_i}\right) + L'\left(\frac{1}{k_s'} + \frac{1}{k_i'}\right)\right\}} = 0. \quad (3)$$

Condition (3) is derived in the approximation of small scattering angles ($\vartheta_s \ll 1$) and without regard for the anisotropy of the group and phase velocities in the nonlinear crystals. In the noncolinear scattering regime ($\vartheta_s \neq 0$), the derivative $\partial\vartheta_s/\partial\omega_s$ is zero if

$$(\tau_s - \tau_i) + (\tau_s' - \tau_i') = 0. \quad (4)$$

Here, $\tau_s = L/u_s$, $\tau_i = L/u_i$, $\tau_s' = L'/u_s'$, and $\tau_i' = L'/u_i'$ have the sense of times of the signal- and idler-photon transition across the nonlinear crystal (τ_q) and the intermediate layer (τ_q') and $u_q = d\omega_q/dk_q$ ($u_q' = d\omega_q/dk_q'$) are the corresponding group velocities ($q = s$ and i).

When detecting the SPS by the crossed-dispersion method [10], the output of the spectral instrument provides a two-dimensional intensity distribution of the scattered radiation in the $\{\omega_s, \vartheta_s\}$ coordinates [see Eq. (1)]. In these coordinates, the interference pattern has a form of alternating fringes with slopes determined by the dispersion of the nonlinear crystals and intermediate layer. The interference maximum forms a hook if the fringe slopes become zero ($\partial\vartheta_s/\partial\omega_s = 0$). The dispersions of the group velocities in the nonlinear crystals and intermediate layer are compensated at the corresponding frequencies of the signal (ω_s) and idler ($\omega_i = \omega_p - \omega_s$) waves; i.e., the differences in the times of signal and idler photon transitions through the crystal and the layer coincide in magnitude and are opposite in sign: $\Delta\tau = -\Delta\tau'$. The slope increases in the range of strong dispersion in the substance, i.e., near the absorption bands. If the nonlinear crystals are transparent over a broad spectral range for all three frequencies while the layer is transparent in the range of signal and pump waves but has resonances of dielectric constant at idler frequencies (in the IR range), then the interference pattern will reflect a change in the dispersion of idler waves in the intermediate layer. The specific feature of the TI is that the absorption in the layer between the crystals, which increases as the frequency approaches resonance, does not diminish the integrated intensity of the scattered radiation. In this case, only the interference visibility is reduced and in the limit where the absorption coefficient becomes of the order of the layer reciprocal thickness $\alpha_i' \approx 1/L'$ the visibility tends to zero [11]. The expression for the scattering line shape, with allowance made for the absorption at the idler frequencies, takes the form

$$g_1(\theta_s, \omega_s) = \sin c^2\left(\frac{\delta}{2}\right)\left(\frac{1 + e^{-\alpha_i' L'}\cos(\delta + \delta')}{2}\right). \quad (5)$$

As follows from Eq. (5), by the visibility is meant the $e^{-\alpha_i' L'}$ function. The unity in the second multiplier in Eq. (5) appears because of the spontaneous nature of the TI effect.

The frequency–angular TI spectra and their features are physically similar to the interference patterns obtained by Rozhdestvenski. In his hook method, the two-dimensional interference spectra are also recorded by using the crossed-dispersion method, when the pattern at the interferometer output is that which is projected onto the entrance slit of the spectrograph. The substance under study is placed in one of the interferometer arms and glass plates of different thicknesses

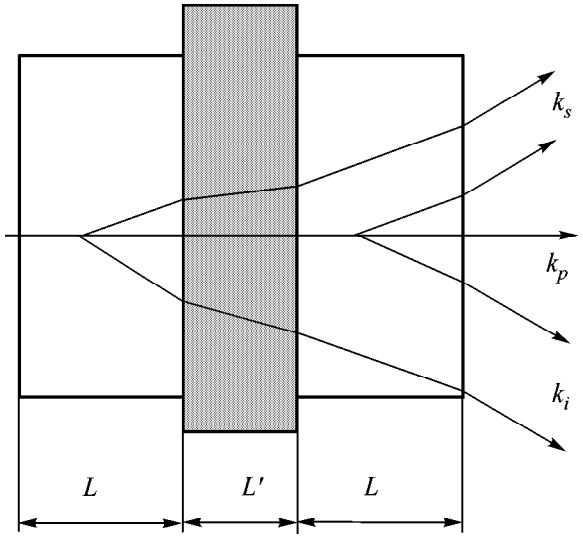

Fig. 1. Diagram of a nonlinear interferometer. Two optically nonlinear crystals of thickness L are separated by a layer of the optically linear substance L' and are excited by a common pump beam.

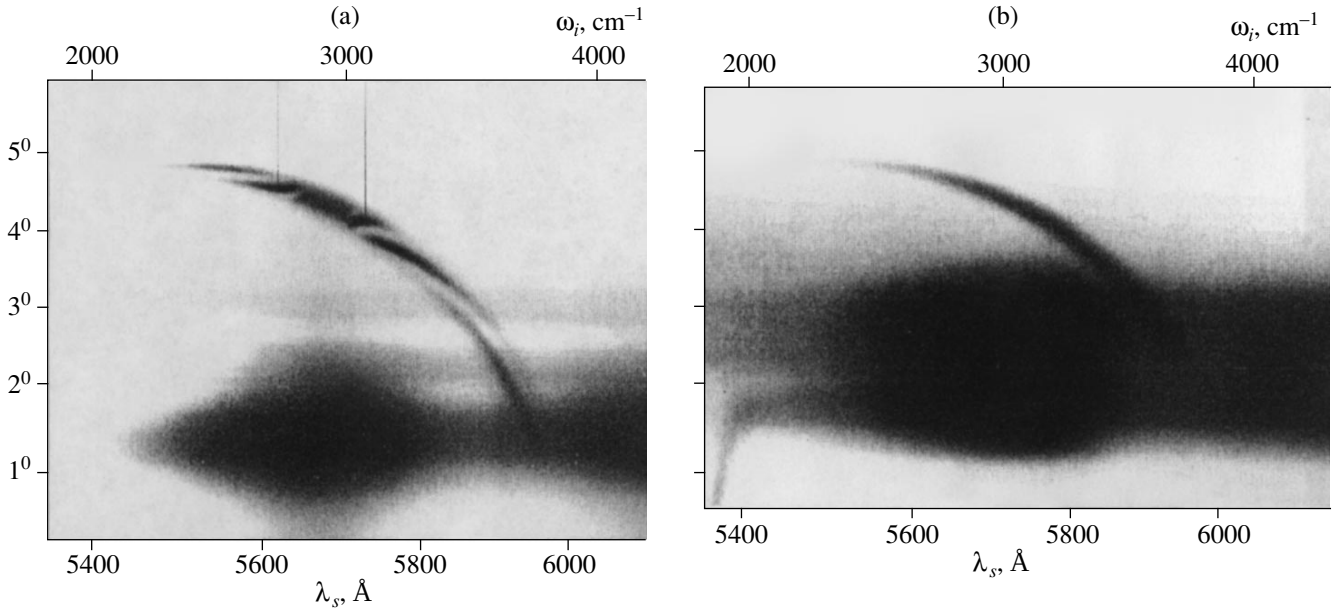

Fig. 2. The frequency–angular SPS spectra: (a) two $LiNBO_3$ crystals (L = 440 μm) are separated by a layer (L' = 50 μm) of paraffin oil; hooks are indicated by the lines parallel to the angular axis; (b) one $LiNBO_3$ crystal.

are placed in the other. *Because the dispersion strongly varies near the absorption band of the substance under study, there will always be a wavelength for which the action of the substance is exactly compensated by the action of a glass plate, so that the slope of the interference curve will pass through zero at this point; to the left of this wavelength, the curves go down and, to the right, they go up (or vice versa), thus forming a hook, whose position can be accurately measured on the wavelength scale* [12]. Of course, the Rozhdestvenski method deals with the linear effect, i.e., with the compensation of light velocities in different substances at the same frequency under the condition of broadband illumination of the interferometer. The requirement on the frequency corresponding to the hook top can be expressed in terms of the group and phase delay times in the substance and plate:

$$(\tau'_{gr} - \tau_{gr}) + (\tau'_{vac} - \tau_{vac}) = 0. \quad (6)$$

Here, $\tau_{gr} = L(d\omega/dk)^{-1}$, $\tau_{vac} = L/c$, $\tau'_{vac} = L'/c$, and $\tau'_{gr} = L'(d\omega/dk')^{-1}$ are the group delay times in the substance (of length L) and the plate (of length L'). As in Eq. (3), the small-angle approximation $\theta_m \ll 1$ is used, where m is the order of interference. Therefore, for the hook to appear in the Rozhdestvenski method, it is necessary that the difference in group delays $\tau'_{gr} - \tau_{gr}$ in the substance and plate coincide in magnitude with the difference in group (phase) delays $\tau'_{vac} - \tau_{vac}$ in the vacuum and be of the opposite sign to it.

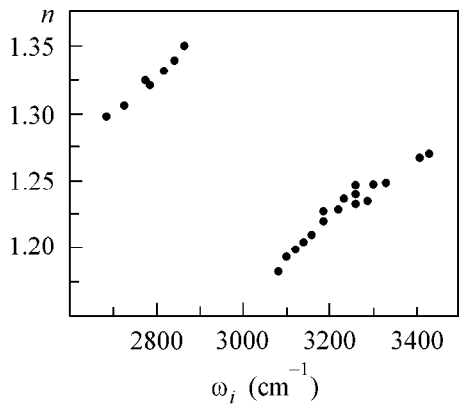

Fig. 3. Frequency-dependent refraction index of paraffin oil in the vicinity of the ω_0 = 2950 cm^{-1} band as derived from the TI spectra.

A comparison of Eqs. (4) and (6) shows that in both cases the hooks can be observed only if the dispersion of the substance under study is compensated. With TI, the differences in the transition times of the signal and idler photons in the nonlinear crystal and the intermediate layer are compensated. In the Rozhdestvenski method, the dispersion of the substance appears as a difference in the group delay times in the studied and reference substances relative to the delays in the vacuum. The following important feature of two-photon interferometry is noteworthy: although the recording is in the visible region, the contribution to the interference

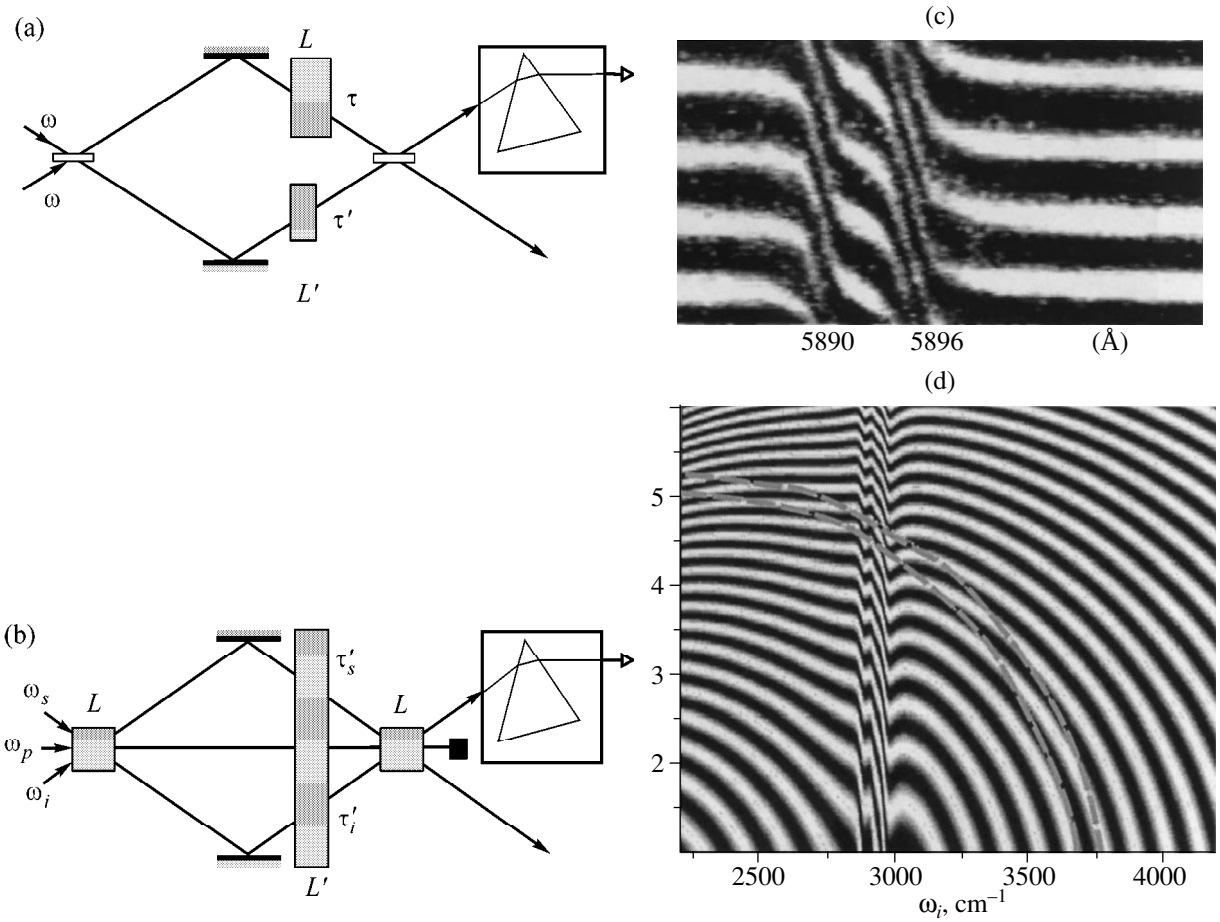

Fig. 4. Qualitative comparison of the (a, c) hook method and (b, d) two-photon interferometry. (a, b) Schemes of the respective interferometers. (c, d) Observed interference patterns: (c) taken from [4] and (d) calculated TI modulation function for $L = 440$ μm and $L' = 50$ μm. The envelope $\sin c^2(\delta/2)$ restricting the observed frequency–angular TI spectrum is shown by the dotted line.

pattern is determined by the group delay at a conjugated frequency lying in the IR range.

In the experiment, the SPS was excited in two thin (L = 440 μm) lithium niobate crystals arranged in tandem and exposed to a common argon laser beam. These crystals are transparent over a wide range (0.4–5.0 μm) and their parametric scattering spectra are well understood. The gap between the crystals was filled with a layer of paraffin oil. The layer thickness was varied within $1 < L' < 50$ μm. The oil has an isolated absorption band at a frequency of 2950 cm^{-1} with a width of 95 cm^{-1}. The photograph of a fragment of the frequency–angular TI spectrum of the crystal–oil–crystal system is given in Fig. 2a. For comparison, the SPS spectrum of one of the lithium niobate crystals is shown in Fig. 2b (L = 440 μm), i.e., in the absence of TI. The resonance-induced distortion of a monotonic progression of the TI orders is clearly seen near 2950 cm^{-1} (signal wavelength λ_s = 5700 Å). The visibility of the interference pattern within the absorption line width is close to zero. In this frequency range, the spontaneous radiation from two crystals is independent, because the idler photons are absorbed in the gap. A sharp change in the slope of the interference maxima occurs in close vicinity of the resonance. It is in this range that the oil refraction index $n'(\omega_i)$ strongly depends on frequency. For some frequencies ($\omega_i \approx 3105$ and 2805 cm^{-1}), the slope of the orders is zero and hooks (indicated by lines) appear in the spectra: the differences in the times of transition through the lithium niobate and paraffin oil coincide for the signal and idler photons. By varying the thickness L' of the gap between the crystals, one can, according to Eq. (4), shift the hooks on the frequency axis, as it also happens in the Rozhdestvenski method. It is notable that the zero slope of the interference orders can be observed away from the resonance as well, because the compensation is also possible in the case of a weak dispersion variation in the substance, but the hooks are then widely extended on the frequency scale.

The TI spectra were used to calculate the $n'(\omega_i)$ dependence for mineral oil. Using the data on the dispersion $n(\omega)$ in lithium niobate [13] at frequencies $\omega_{i1} \approx 3105$ cm^{-1} (λ_{s1} = 5752 Å) and $\omega_{i2} \approx 2805$ cm^{-1}

(λ_{s2} = 5654 Å), where the hooks are observed (see Fig. 2a), the differences in the group delay times in oil were determined from Eq. (4). They proved to be $\tau'_{s1} - \tau'_{i1}$ = 330 fs and, respectively, $\tau'_{s2} - \tau'_{i2}$ = 312 fs. After measuring the oil dispersion in the visible range by the prism method, Eq. (5) was used to find the group velocities on different sides of the resonance frequency ω_0 = 2950 cm^{-1}: $u'_1(\omega_{i1}) \approx u'_2(\omega_{i2}) = (8.3 \pm 0.5) \times 10^9$ cm/s. These data agree, within the experimental error, with the results obtained by estimating u' from the measured $n'(\omega_i)$ dependence (Fig. 3).

In conclusion, let us turn to Fig. 4, where the two methods are pictorially compared with each other. The schemes of linear and nonlinear interferometers [14] are shown in Figs. 4a and 4b. The intermediate layer (L') is an analogue of the substance under study (of length L') and the nonlinear crystals (L) are analogues of the compensation plates (of length L). The respective delays are shown by the shaded rectangles. The frequency–angular TI spectra and the Rozhdestvenski interference patterns borrowed from [4] are shown in Figs. 4c and 4d. For clarity, only the modulation TI component $\cos^2[(\delta + \delta')/2]$ is shown, without taking into account the envelope $\sin c^2(\delta L/2)$ (shown by the dotted line). The qualitative similarity of both pictures confirms that the analogues are adequate. It should also be emphasized that the mechanism of formation of the frequency–angular TI spectra near the absorption bands of the intermediate substance has much in common with the formation of the polariton-scattering spectra observed in crystals without center of inversion [15].

We are grateful to A.N. Nozdryakov and S.V. Ivanchenko for assistance in obtaining the IR spectra. This work was supported by the Russian Foundation for Basic Research, project nos. 99-02-16418, 99-02-16419, and 00-15-96541.

REFERENCES

1. A. V. Burlakov, M. V. Chekhova, D. N. Klyshko, *et al.*, Phys. Rev. A **56**, 3214 (1997).
2. L. Mandel, Rev. Mod. Phys. **71**, S274 (1999).
3. D. N. Klyshko, Usp. Fiz. Nauk **164**, 1187 (1994) [Phys. Usp. **37**, 1097 (1994)].
4. D. S. Rozhdestvenskiĭ, *Works on Anomalous Dispersion of Metal Vapors* (Akad. Nauk SSSR, Moscow, 1951).
5. D. N. Klyshko, *Photons and Nonlinear Optics* (Nauka, Moscow, 1980).
6. A. V. Belinsky and D. N. Klyshko, Laser Phys. **2**, 112 (1992).
7. D. N. Klyshko, Zh. Éksp. Teor. Fiz. **104**, 2676 (1993) [JETP **77**, 222 (1993)].
8. D. Yu. Korystov, S. P. Kulik, and A. N. Penin, Kvantovaya Élektron. (Moscow) **30**, 922 (2000).
9. A. V. Burlakov, S. P. Kulik, A. N. Penin, and M. V. Chekhova, Zh. Éksp. Teor. Fiz. **113**, 1991 (1998) [JETP **86**, 1090 (1998)].
10. D. N. Klyshko, A. N. Penin, and B. F. Polkovnikov, Pis'ma Zh. Éksp. Teor. Fiz. **11**, 11 (1970) [JETP Lett. **11**, 5 (1970)].
11. A. V. Burlakov, Yu. B. Mamaeva, A. N. Penin, and M. V. Chekhova, Zh. Éksp. Teor. Fiz. (in press) [JETP (in press)].
12. G. S. Landsberg, *Optics* (Nauka, Moscow, 1976).
13. G. Kh. Kitaeva, K. A. Kuznetsov, I. I. Naumova, and A. N. Penin, Kvantovaya Élektron. (Moscow) **30**, 726 (2000).
14. It was demonstrated in [1] that the schemes shown in Figs. 1 and 4b are physically equivalent.
15. Yu. N. Polivanov, Usp. Fiz. Nauk **126**, 185 (1978) [Sov. Phys. Usp. **21**, 805 (1978)].

Translated by V. Sakun

JETP Letters, Vol. 73, No. 5, 2001, pp. 219–222. Translated from Pis'ma v Zhurnal Éksperimental'noĭ i Teoreticheskoĭ Fiziki, Vol. 73, No. 5, 2001, pp. 253–257.

Generation of Millimeter Radiation Due to Electric-Field-Induced Electron-Transit-Time Resonance in Indium Phosphide

L. E. Vorob'ev[1], S. N. Danilov[1], V. N. Tulupenko[2], and D. A. Firsov[1]

[1] *St. Petersburg State Technical University, ul. Politekhnicheskaya 29, St. Petersburg, 195251 Russia*
e-mail: LVor@twonet.stu.neva.ru

[2] *Donbass State Mechanical Engineering Academy, Kramatorsk, 343913 Ukraine*

Received January 31, 2001

The stimulated millimeter radiation from *n*-type indium phosphide was observed at $T = 4.2$ K in a strong electric field. The generation is due to the appearance of negative differential conductivity near the electron-transit-time resonance and electron bundling in momentum space in a strong electric field under conditions of low-temperature scattering from optical phonons. The dependence of the radiation frequency and intensity on the electric field was experimentally measured and the radiation spectrum is presented. The experimental data satisfactorily agree with the results of numerical simulations obtained previously by the Monte Carlo method. © *2001 MAIK "Nauka/Interperiodica"*.

PACS numbers: 72.20.Ht; 78.20.-e; 78.45.+h

1. Introduction. The charge-carrier momentum distribution function in relatively pure semiconductors becomes spike-shaped in strong electric fields under conditions of low-temperature charge-carrier scattering from optical phonons. In this regime, charge carriers execute cyclic motion in momentum space; they move almost ballistically in the passive energy region $\mathscr{E} < \hbar\omega_{PO}$ ($\mathscr{E}$ and $\hbar\omega_{PO}$ are the energies of charge carrier and optical phonon, respectively), emit optical phonon in the active region $\mathscr{E} > \hbar\omega_{PO}$, and then return to the vicinity of the $\mathscr{E} \approx 0$ point. The time of ballistic transition through the passive region in a field E is $\tau_{tr} = \sqrt{2m_e\hbar\omega_{PO}}/eE$, where m_e is the charge-carrier effective mass. The condition for the formation of a spike-shaped distribution is

$$\tau_{PO}^{+} \ll \tau_{tr} \ll \tau_p, \qquad (1)$$

where τ_{PO}^{+} is the optical-phonon emission time and τ_p is the scattering time in the passive energy (or momentum) region $\mathscr{E}(p) < \hbar\omega_{PO}$. The condition $\tau_{tr} \ll \tau_p$ can easily be fulfilled in weakly doped semiconductors at low temperatures. The scattering from acoustic lattice modes is then suppressed, while the impurity scattering is insignificant because of the weak doping. The inequality $\tau_{PO}^{+} \ll \tau_{tr}$ means the weak penetration of electrons (or holes) into the active region. Otherwise the charge carrier, after emission of a *PO* phonon, will have too high an initial energy in the passive region for the spike-shaped distribution to form.

If condition (1) is fulfilled, new effects may emerge such as the interband population inversion of hot holes in germanium in crossed electric and magnetic fields and the amplification of far-IR radiation [1]. In this case, population inversion between light- and heavy-hole subbands arises because of a difference in the motional dynamics of heavy and light holes in a certain range of electric and magnetic fields $\mathbf{E} \perp \mathbf{H}$ [1]. The population inversion was observed and quantitatively estimated in [2]. Shortly after, generation of far-IR radiation was obtained on the direct interband optical transitions of hot holes in germanium in crossed electric and magnetic fields [3, 4].

The realization of a spike-shaped hole distribution in germanium made it possible to develop a millimeter-range negative transverse effective mass heavy-hole maser [5]. Thus, the idea of designing a negative effective hole mass amplifier and generator (NEMAG) was implemented 25 years after it had been proposed by Krömer as early as 1959 [6].

The appearance of a high-frequency negative differential electron conductivity (NDC) near the transit-time-resonance frequency $\nu_{tr} = 1/\tau_{tr}$ in strong electric fields was predicted and theoretically considered in [7–9]. Equation (1) is the necessary condition for the occurrence of dynamic NDC. NDC appears due to electron transition and bundling about the main trajectory in momentum space. According to [7–9], the modulation of electron distribution can be caused both by the electron penetration into the active region at a relatively small depth $\mathscr{E} - \hbar\omega_{PO} \ll \hbar\omega_{PO}$ and by a relatively weak electron scattering in the passive region, with the NDC

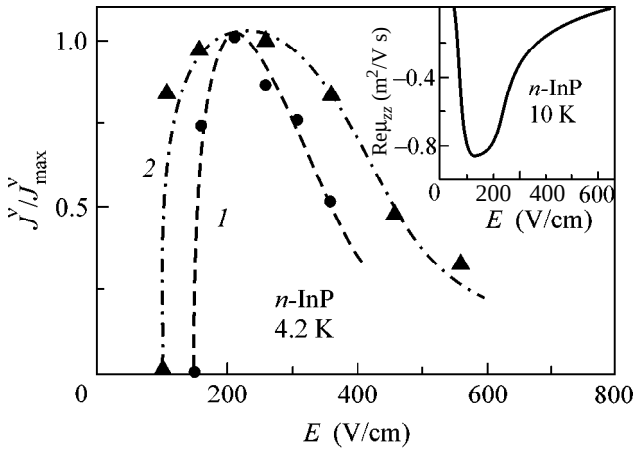

Fig. 1. Radiation detector signal as a function of the electric field in the *n*-type indium phosphide samples at 4.2 K. (*1*) Sample with electron concentration $N_e = 1 \times 10^{14}$ cm^{-3}; the Schottky diode detector. (*2*) Sample of different sizes (compared to sample *1*) with electron concentration $N_e = 3 \times 10^{14}$ cm^{-3}; the *n*-InSb detector. Inset: field dependence calculated in [11] for the dynamic negative mobility in InP with impurity concentration $N_i = 10^{15}$ cm^{-3}.

magnitude depending on the electron-scattering mechanism in the passive region [10]. According to [10], the scattering mechanisms whose probabilities decrease with increasing $\mathscr{E}$, e.g., impurity scattering, are most favorable to NDC.

A direct numerical Monte Carlo simulation of the electron motion in strong dc and high-frequency ac fields was carried out in [11] to demonstrate that the conditions for the occurrence of NDC in InP are more favorable than in GaAs and that the NDC magnitude in InP is several times larger than in a *p*-Ge cyclotron-resonance NEMAG.

In spite of the fact that more than 25 years have elapsed since the prediction of the NDC near the transit-time-resonance frequency, this phenomenon has not been observed until recently. This work reports the first results on the generation of millimeter radiation in the range of hot-electron-transit-time resonance. Although this phenomenon was observed in *n*-InP, an analogous phenomenon can be observed in other semiconductors as well. In particular, it was demonstrated in [12] that the NDC and the terahertz-range transit-time-resonance lasing can be obtained in *n*-GaN at appreciably higher frequencies in the range 0.2–3.0 THz (λ = 1.5 mm–100 μm).

2. Samples and experimental method. One of the samples of *n*-type indium phosphide was a $54 \times 8 \times 7$ mm parallelepiped with mutually perpendicular faces. The faces were plane-parallel to within one and a half of angular minute. Ohmic contacts were applied to two faces with sizes 54×7 mm. The cavity mirrors were formed by two gold-evaporated germanium (Ge : Au) plates with high-resistance at low temperatures. To provide radiation escape, one of the mirrors was smaller in size than the 7×8-mm crystal faces to which the mirrors were attached. Note that the cavity quality was not high because the transverse sizes of the sample were comparable with the radiation wavelength so that the diffraction losses were appreciable.

The Hall concentrations and mobilities measured at $T = 77$ K were, respectively, $N_e = 1 \times 10^{14}$ cm^{-3} and $\mu_H = 3 \times 10^4$ cm^2/(V s) for the first sample and $N_e = 3 \times 10^{14}$ cm^{-3} and $\mu_H = 3.3 \times 10^4$ cm^2/(V s) for the second sample. The duration of strong-field pulses was 2 μs.

The radiation wavelength was measured using a specially designed wavemeter with cavity tuning. *n*-Type indium antimonide or a Schottky semiconductor diode was used as a detector of millimeter radiation.

3. Experimental results and discussion. Figure 1 shows the normalized dependence of the detector signal on the electric field applied to the sample. Measurements were made using the Schottky diode for the first sample and the *n*-InSb detector for the second one. Since the radiation wavelength depends on the electric field, these curves reproduce the field dependence of the relative radiation intensity only approximately, with an accuracy requiring correction for the spectral sensitivity of the detectors. The field dependence of the dynamic differential electron mobility (a quantity proportional to NDC) in *n*-InP with concentration of ionized impurities $N_I = 10^{15}$ cm^{-3} (shown in the inset in Fig. 1) was calculated in [11] by the numerical Monte Carlo simulation of electron motion in strong dc and weak ac electric fields. The correlation between the calculated field dependence of the negative differential mobility and the field dependence of the detector signal is clearly seen.

Figure 2 shows the spectra of the detector (Schottky diode) signal measured by the wavemeter for the first *n*-InP sample in different electric fields. The widths of the stimulated emission lines were determined by the instrumental resolution.

Finally, the frequency of stimulated emission is plotted in Fig. 3 as a function of electric field for the first *n*-InP sample (dots). The field dependences calculated in [11] for the amplification frequency range (dashed lines) and the maximum amplification frequency (see Fig. 1) are shown in the same figure. The discordance between the experimental and calculated data at low frequencies can be due to the error in measuring frequency by the wavemeter in the long-wavelength range and to the voltage drop at contacts, which may affect the accuracy of field determination at weak currents.

Let us now estimate the region where condition (1) necessary for the occurrence of NDC is fulfilled. The scattering from the deformation acoustic (*DA*) lattice modes, impurity (*I*) scattering, and scattering from the polar optical (*PO*) lattice modes are the dominant elec-

tron-scattering mechanisms in the indium phosphide samples studied. According to [13], the probabilities of scattering by the *DA* and *PO* phonons are

$$w_{DA}^{+,-} = \frac{\pi \Xi^2 q^2}{V \rho \omega_{DA}(q)} \times \left\{ \begin{array}{c} N_q \delta[\mathscr{E}(\mathbf{k}') - \mathscr{E}(\mathbf{k}) - \hbar\omega_{DA}(q)] \\ (N_q + 1)\delta[\mathscr{E}(\mathbf{k}') - \mathscr{E}(\mathbf{k}) + \hbar\omega_{DA}(q)] \end{array} \right\}, \quad (2)$$

$$w_{PO}^{+,-} = \frac{4\pi e^2 \omega_{PO}(\varepsilon_\infty^{-1} - \varepsilon_0^{-1})}{V q^2} \times \left\{ \begin{array}{c} N_q \delta[\mathscr{E}(\mathbf{k}') - \mathscr{E}(\mathbf{k}) - \hbar\omega_{PO}(q)] \\ (N_q + 1)\delta[\mathscr{E}(\mathbf{k}') - \mathscr{E}(\mathbf{k}) + \hbar\omega_{PO}(q)] \end{array} \right\}, \quad (3)$$

$$\mathbf{k}' = \mathbf{k} \pm \mathbf{q},$$

where Ξ is the deformation potential; q is the phonon wave vector; ρ is the density; ω_{PO} and ω_{DA} are the frequencies of optical and acoustic lattice modes, respectively; $\omega_{DA} = v_l q$ (v_l is the sound velocity); ε_∞ and ε_0 are the high-frequency and the static dielectric constants of the crystal, respectively; $\mathbf{k}$ and $\mathbf{k}'$ are the electron wave vectors in the initial and final states, respectively; and $N_q = [\exp(\hbar\omega_{DA,\,PO}/k_BT) - 1]^{-1}$. The first rows in Eqs. (2) and (3) correspond to the phonon-absorption processes and the second rows are for the phonon-emission processes. The probability of scattering from the screened impurity potential $\varphi = (e/\varepsilon_0 r)\exp(-r/r_D)$, where r_D is the Debye screening radius $r_D = q_D^{-1} = (\varepsilon_0 k_B T_e/4\pi e^2 N_e)^{1/2}$, can easily be found:

$$w_I = \frac{32\pi^3 e^4}{V\varepsilon_0^2 \hbar} \frac{1}{[q_D^2 + (\mathbf{k}' - \mathbf{k})^2]^2} \delta[\mathscr{E}(\mathbf{k}') - \mathscr{E}(\mathbf{k})], \quad (4)$$

$$\mathbf{k}' = \mathbf{k} + \mathbf{q}.$$

Let us first find the electron–optical phonon collision frequency. Summing (integrating) in Eq. (3) over all $\mathbf{k}'$ (or $\mathbf{q}$) values, one obtains

$$W_{PO} = \tau_{PO}^{-1} = \frac{\sqrt{2} e^2 \omega_{PO} \sqrt{m_e}(\varepsilon_\infty^{-1} - \varepsilon_0^{-1})}{\hbar\sqrt{\mathscr{E}}} \times \left[N_q \ln \frac{\sqrt{\mathscr{E} + \hbar\omega_{PO}} + \sqrt{\mathscr{E}}}{\sqrt{\mathscr{E} + \hbar\omega_{PO}} - \sqrt{\mathscr{E}}} + (N_q + 1) \ln \frac{\sqrt{\mathscr{E}} + \sqrt{\mathscr{E} - \hbar\omega_{PO}}}{\sqrt{\mathscr{E}} - \sqrt{\mathscr{E} - \hbar\omega_{PO}}} \right], \quad (5)$$

where the first and the second terms in square brackets account for the processes with phonon absorption and emission, respectively. At low temperatures ($k_BT \ll \hbar\omega_{PO}$), $N_q \approx 0$ and only the second term can be kept in Eq. (5). The scattering with emission of optical phonons occurs only in the active energy region $\mathscr{E} > \hbar\omega_{PO}$.

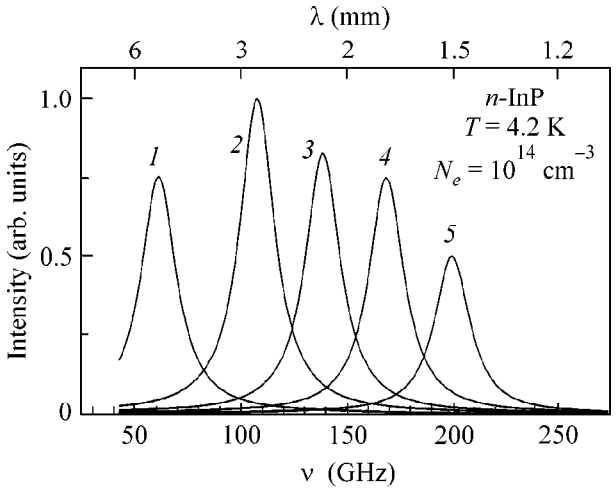

Fig. 2. Spectra of the detector signal (Schottky diode) for different electric fields: E = (*1*) 200, (*2*) 250, (*3*) 300, (*4*) 350, and (*5*) 400 V/cm.

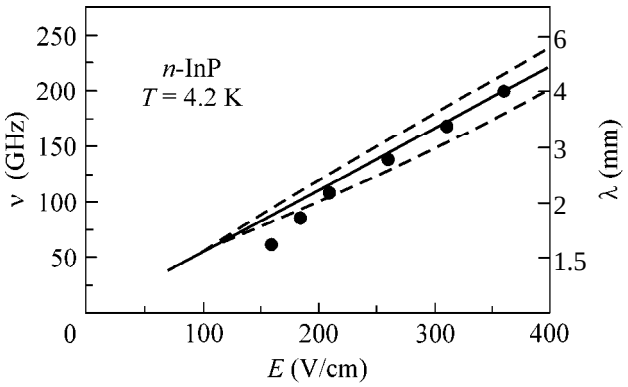

Fig. 3. Variation of the generation frequency with the field for *n*- InP sample *1* (dots). Field dependences calculated in [11] for the amplification frequency range (dashed lines) and the maximum NDC frequency are also shown.

In the passive region $\mathscr{E} < \hbar\omega_{PO}$, electron scattering with absorption and emission of acoustic phonons and impurity scattering should be taken into account. We will estimate the scattering probability (or frequency) only for the processes that can materially change the direction of the initial wave vector $\mathbf{k}$ (for the spike-shaped distribution, $\mathbf{k}$ is almost aligned with the field $\mathbf{E}$) and, thereby, break the spike-shaped electron-momentum distribution. The simplest estimates will be done under the assumption that a change in the $\mathbf{k}$ direction within an angle θ_0 ($\theta_0 \ll 90°$) has no dramatic effect on the direction of electron movement. We are now in a position to consider the total probability of scattering to all $\mathbf{k}'$ states beyond the cone with an angle of θ_0 between $\mathbf{k}$ and $\mathbf{k}'$ in k space. Summing (integrat-

ing) in Eqs. (2) and (4) over all **k**' states beyond this cone, we obtain

$$W_{DA} = \tau_{DA}^{-1} = \frac{\sqrt{2}\Xi^2 m_e^{3/2} k_B T \sqrt{\mathscr{E}}(1-\sin^2\theta_0)}{\pi\hbar^4 \rho v_l^2}, \quad (6)$$

$$W_I = \tau_I^{-1} = \frac{\pi e^4 N_I}{2\sqrt{2}\varepsilon_0^2 \sqrt{m_e}\mathscr{E}^{3/2}} \times \frac{(1-\sin^2\theta_0)}{(1+\mathscr{E}_D/4\mathscr{E})(\sin^2\theta_0 + \mathscr{E}_D/4\mathscr{E})}, \quad (7)$$

where $\mathscr{E}_D = \hbar^2 q_D^2/2m_e$ and N_I is the concentration of charged impurities. According to [14], the electron mobility $\mu = 3\times10^4$ cm^2/(V s) at $T = 77$ K is typical for the InP samples with a total concentration of charged impurities $N_I = N_D + N_A \approx (5\text{–}7)\times10^{15}$ cm^{-3}. Let us estimate Eqs. (6) and (7) for $\theta_0 = 30°$, $T = 4.2$ K, and $\mathscr{E} \approx \hbar\omega_{PO}/2$ and Eq. (5) for $\mathscr{E} = 1.5\hbar\omega_{PO}$ and the following InP parameters, taken from [15, 16]: $m_e = 0.078m_0$, $v_l = 5\times10^5$ cm/s, $\rho = 4.81$ g/cm^3, $\hbar\omega_{PO} = 43$ meV, $\varepsilon_0 = 12.5$, $\varepsilon_\infty = 9.52$, and $\Xi = 9$ eV. This gives $\tau_{DA} \approx 4\times10^{-10}$ s, $\tau_I \approx (0.7\text{–}1)\times10^{-11}$ s, and $\tau_{PO}^+ \approx 0.56\times10^{-11}$ s.

The generation in our samples sets in near $E = 200$ V/cm. For $E = 200$ V/cm, the transit time across the passive region is $\tau_{tr} = 10^{-11}$ s. Inasmuch as $\tau_{PO}^+ < \tau_{tr}$, electrons penetrate into the active region at a relatively small depth. It can be estimated from a simple relation:

$$\mathscr{E} = \frac{p^2}{2m_e} = \frac{[p_0 + eE\tau^+(\mathscr{E})]^2}{2m_e} = \hbar\omega_{PO}\left[1 + \frac{eE\tau^+(\mathscr{E})}{p_0}\right]^2. \quad (8)$$

Using Eq. (8), it is straightforward to find that the electron penetration depth into the active region is about $0.2\hbar\omega_0$ at $E = 200$ V/cm.

The impurity scattering dominates the passive region; i.e., $\tau_p \approx \tau_I$. According to the above estimate $\tau_p/\tau_{tr} \approx 0.7\text{–}1$, the inequality $\tau_p \gg \tau_{tr}$ is not fulfilled. The calculation in [11] was carried out for InP with $N_I = 10^{15}$ cm^{-3}. For a sample with such concentration, $\tau_I \approx 5\times10^{-11}$ s and the NDC, according to [11] (see inset in Fig. 1), appears at $E \approx 70$ V/cm. For such fields, $\tau_{tr} \approx 3\times10^{-11}$ s and $\tau_p/\tau_{tr} \approx 1.7$. Hence, the condition $\tau_p \gg \tau_{tr}$ is also poorly fulfilled. Nevertheless, the direct Monte Carlo computations [11] suggest the appearance of the NDC. Our investigation also testifies that the NDC appears and the generation sets in, despite the high impurity concentration in the samples studied.

4. Conclusions. In this work, the generation of millimeter radiation in *n*-type indium phosphide was observed in strong electric fields. The experimental data suggest that this phenomenon is caused by transit-time resonance. The generation is observed in a moderately doped samples, in which the condition for collisionless electron motion in the passive region is poorly fulfilled. One should expect the generation of a more intense radiation in the *n*-InP samples with concentration of charged impurities less than 5×10^{15} cm^{-3}.

This work was supported by the Ministry of Education of the Russian Federation.

REFERENCES

1. A. A. Andronov, V. A. Kozlov, L. S. Mazov, and V. N. Shastin, Pis'ma Zh. Éksp. Teor. Fiz. **30**, 585 (1979) [JETP Lett. **30**, 551 (1979)].
2. L. E. Vorob'ev, F. I. Osokin, V. I. Stafeev, and V. N. Tulupenko, Pis'ma Zh. Éksp. Teor. Fiz. **34**, 125 (1981) [JETP Lett. **34**, 118 (1981)].
3. L. E. Vorob'ev, F. I. Osokin, V. I. Stafeev, and V. N. Tulupenko, Pis'ma Zh. Éksp. Teor. Fiz. **35**, 360 (1982) [JETP Lett. **35**, 440 (1982)].
4. A. A. Andronov, I. V. Zverev, V. A. Kozlov, *et al.*, Pis'ma Zh. Éksp. Teor. Fiz. **40** (2), 69 (1984) [JETP Lett. **40**, 804 (1984)].
5. A. A. Andronov, A. M. Belyantsev, V. I. Gavrilenko, *et al.*, Pis'ma Zh. Éksp. Teor. Fiz. **40** (6), 221 (1984) [JETP Lett. **40**, 989 (1984)].
6. H. Krömer, Phys. Rev. **109**, 1856 (1958).
7. A. A. Andronov and V. A. Kozlov, Pis'ma Zh. Éksp. Teor. Fiz. **17**, 124 (1973) [JETP Lett. **17**, 87 (1973)].
8. Yu. V. Gulyaev and I. I. Chusov, Fiz. Tverd. Tela (Leningrad) **20**, 2637 (1978) [Sov. Phys. Solid State **20**, 1524 (1978)].
9. A. Matulis and A. Chenis, Zh. Éksp. Teor. Fiz. **77**, 1134 (1979) [Sov. Phys. JETP **50**, 572 (1979)].
10. E. V. Starikov and P. N. Shiktorov, Fiz. Tekh. Poluprovodn. (Leningrad) **17**, 2120 (1983) [Sov. Phys. Semicond. **17**, 1355 (1983)].
11. E. V. Starikov and P. N. Shiktorov, Litov. Fiz. Sb. **32** (4), 471 (1992).
12. E. Starikov, P. Shiktorov, V. Gruzinkas, *et al.*, IEEE Trans. Electron Devices **48** (3) (2001).
13. E. M. Conwell, *High Field Transport in Semiconductors* (Academic, New York, 1967; Mir, Moscow, 1970).
14. D. A. Anderson and N. Apsley, Semicond. Sci. Technol. **1**, 187 (1986).
15. K. Brennan and K. Hess, Solid-State Electron. **27**, 347 (1984).
16. *Handbook Series on Semiconductor Parameters*, Ed. by M. Levinstein, S. Rumyantsev, and M. Shur (World Scientific, Singapore, 1996), Vol. 1.

Translated by V. Sakun

JETP Letters, Vol. 73, No. 5, 2001, pp. 223–227. From Pis'ma v Zhurnal Éksperimental'noĭ i Teoreticheskoĭ Fiziki, Vol. 73, No. 5, 2001, pp. 258–262.

Formation of Shocks Related to Dust-Particle Charging in Complex Plasmas[1]

S. I. Popel[1], A. P. Golub'[1], T. V. Losseva[1], and R. Bingham[2]

[1] *Institute of Geosphere Dynamics, Russian Academy of Sciences, Leninskiĭ pr. 38-6, Moscow, 117334 Russia*

[2] *Rutherford Appleton Laboratory, Chilton, Didcot, Oxfordshire, OX 11 OQX, UK*

Received January 15, 2001

The nonstationary problem of the evolution of perturbation and its transformation into nonlinear wave structure in complex plasmas (multicomponent plasmas containing ions, electrons, charged microspheres or dust grains, and neutral gas) is considered. For this purpose, the model, which takes into account the variation of ion density and the ion-momentum dissipation due to dust-particle charging, as well as the source of plasma particles due to the ionization process, is developed. The model is appropriate for the description of laboratory experiments in complex plasmas and contains all basic mechanisms responsible for the formation of a new kind of shock waves which is related to the anomalous dissipation due to the dust-particle charging process. The consideration on the basis of this model allows us to obtain shock structures as a result of evolution of an initial perturbation and to explain the experimental value of the width of the ion acoustic shock-wave front, as well as the shock-wave speed. The solution of the problem of the evolution of perturbation and its transformation into a shock wave in complex plasmas opens up possibilities for description of the real phenomena like supernova explosions, as well as of the laboratory and active space and geophysical experiments. *© 2001 MAIK "Nauka/Interperiodica".*

PACS numbers: 52.27.Lw; 52.35.Tc

At present, a major portion of the investigations of plasmas is devoted to multicomponent plasmas containing electrons, ions, charged microspheres or dust grains, and neutral particles. The term "complex plasmas" is finding increasing use for such plasmas. Complex (dusty) plasma systems cannot usually survive in the absence of either external sources of electrons and ions or plasma particle fluxes from the regions where there is no dust. The fluxes of electrons and ions are absorbed by dust particles, which results in variable charges of the latter. The strong dissipativity of the complex plasma system originating from the dust-particle charging processes [1] points to the exceptional role of the dissipative structures (like shock waves) in complex plasmas.

Shock waves often arise in nature because of a balance between wave-breaking nonlinear and wave-damping dissipative forces. Collisional and collisionless shock waves can appear because of friction between the particles [2] and wave–particle interaction [3], respectively. In complex plasmas, the appearance of anomalous dissipation, which originates from charging processes, results in the possibility of the existence of a new kind of shock wave related to this dissipation. They are collisionless in the sense that they do not involve electron–ion collisions. However, in contrast to the classical collisionless shock waves, the dissipation due to dust charging involves interaction of the electrons and ions with the dust grains in the form of microscopic grain currents. The case when the shock waves related to the dust-particle charging process are rather intense corresponds to ion acoustic wave propagation. The basic theoretical results on ion acoustic shocks in complex plasmas are obtained in [4–8]. Recently, the first laboratory experimental results confirming the effect of negatively charged dust on ion acoustic shock formation have been obtained [7, 9]. The problem of shock waves in complex plasmas is considered now in the dusty plasma community as one of the key problems. The importance of shock waves in complex plasmas is associated, in particular, with different astrophysical and geophysical applications [5, 6, 10]. For example, the investigation of such shocks can be important for the description of the process of star and planet formation, shocks in supernova explosions, particle acceleration in shocks, for the explanation of the effects in active experiments which involve the release of gaseous substance in the Earth's ionosphere, etc.

In spite of the importance of shock structures in complex plasmas, the question of whether the evolution of an arbitrary perturbation leads to the formation of shocks in a charge-varying complex plasma is still an open question. All previous investigations dealt with steady-state or steady-state shocklike wave solutions. However, it is the solution of the problem of the evolution of perturbation and the possibility of its transformation into shock wave that can allow us to investigate in detail (with taking into account the charge-varying

[1] This article was submitted by the authors in English.

macroparticles) real phenomena like supernova explosions, as well as laboratory and active space experiments.

Furthermore, the main theoretical results which concern the ion acoustic shocks in complex plasmas are obtained in two ways:

(1) by using and solving the exact equation for dust-particle charge variation (see, e.g., [4]);

(2) by using a Korteweg–de Vries–Burgers equation with a dissipation coefficient proportional to the frequency of collisions between ions and dust particles (see, e.g., [7, 8]).

Both these approaches use the ion continuity equation with a zero right-hand side (see [4, 8]). This means that the total ion density is constant. This assumption for complex plasmas can be valid, e.g., if the ions and electrons entering the dust grain recombine into neutral atoms, which then reenter the plasma and reionize, thus preserving the number of ions and electrons. However, in most laboratory complex plasmas, this assumption is violated. As it has been mentioned, complex plasma systems cannot usually survive in the absence of either external sources of electrons and ions or plasma particle fluxes from the regions where there is no dust. In laboratory experiments, the external source of plasma particles is usually due to the ionization process. Thus, a more appropriate model for the description of laboratory experiments must include the effects of the variation of ion density and the ion-momentum dissipation due to dust-particle charging, as well as the source of plasma particles due to ionization process.

In this study, we develop a model based on a set of fluid equations, Poisson's equation, and a charging equation for dust, which takes into account the variation of ion density and the ion-momentum dissipation due to dust-particle charging, as well as the ionization process. This model is a nonstationary analogue of the model used for the description of dust voids (see [11]). We compare the computational results with the experimental data [9].

We assume that the following simplifying approximations are valid:

(1) the plasma can be considered as uniform and unmagnetized;

(2) the time scale corresponds to ion acoustic wave propagation;

(3) the dust-particle charge variation is solely due to the microscopic electron and ion grain currents originating from the potential difference between the plasma and the grain surface;

(4) the average radius a of the dust particles is much smaller than the electron Debye length λ_D, the spatial scale of the perturbations, and the distance between the plasma particles;

(5) the dust grains are negatively and heavily charged (with an absolute values that can exceed $10^3 e$, where $-e$ is the electron charge);

(6) the dust particles are massive ($m_i Z_d \ll m_d$, where m_i and m_d are the ion and dust masses and $q_d(x) = -Z_d e$ is the dust-particle average charge). Then the dust can be considered stationary, and its density n_d is constant in the ion acoustic time scale [12, 13];

(7) in the absence of perturbations, the quasineutrality condition $n_{i0} = n_{e0} + Z_d n_d$ (where $n_{e(i)}$ is the electron (ion) density, the subscript 0 denotes unperturbed quantities) holds;

(8) the ions are singly charged;

(9) the electron (T_e) and ion (T_i) temperatures are approximated to be spatially uniform;

(10) the orbit-limited probe model [14, 15] is valid;

(11) nonlinear waves propagate along the x axis.

Furthermore, we neglect any heat transfer processes that might influence the propagation and evolution of ion acoustic perturbation. As in [11], the most noteworthy approximation is that we do not include ion–neutral collisions, which would exert a drag force on the ions. They reduce the ion velocity, which affects the ion drag force on a dust particle, as well as the dust-particle charge. Neglect of the direct influence of neutrals on dust particles is justified by the consideration of ion acoustic time scales, so that the dust can be considered as stationary. Finally, we assume that in the absence of perturbations in plasmas the number of electrons and ions is constant due to competition of the processes of their recombination on dust particles and ionization.

In this case, the evolution equations for ion density n_i and velocity v_i take the form (cf. [11, 16])

$$\partial_t n_i + \partial_x(n_i v_i) = -\nu_{\rm ch} n_i + \nu_i n_e, \tag{1}$$

$$\partial_t(n_i v_i) + \partial_x(n_i v_i^2) = -\frac{e n_i}{m_i}\partial_x\varphi - \tilde{\nu} n_{0i} v_i, \tag{2}$$

where φ is the electrostatic potential, ν_i is the plasma ionization frequency, which increases exponentially with T_e and also depends on the atomic parameters of the neutral gas [17], $\nu_{\rm ch}$ is the frequency of ion recombination on dust particles,

$$\nu_{\rm ch} = \nu_q \frac{Z_{d0} d}{1 + Z_{d0} d} \frac{(T_i/T_e + z_0)}{z_0(1 + T_i/T_e + z_0)}, \tag{3}$$

$\nu_q = \omega_{pi}^2 a(1 + z_0 + T_i/T_e)/\sqrt{2\pi}\, v_{Ti}$ is the dust-particle charging frequency, $z = Z_d e^2/aT_e$, $d = n_{d0}/n_{e0}$, $\omega_{pi} = \sqrt{4\pi n_{i0} e^2/m_i}$ is the ion plasma frequency, $v_{Ti} = \sqrt{T_i/m_i}$ is the ion thermal speed, $\tilde{\nu}$ is the frequency characterizing a loss in ion momentum due to recombination on

dust particles and Coulomb elastic collisions between ions and dust,

$$\tilde{\nu} = \nu_q \frac{Z_{d0}d}{(1 + Z_{d0}d)z_0(1 + T_i/T_e + z_0)} \times\left(z_0 + \frac{4T_i}{3T_e} + \frac{2z_0^2 T_e}{3T_i}\Lambda\right), \quad (4)$$

$\Lambda = \ln(\lambda_{Di}/\max\{a, b\})$ is the Coulomb logarithm, λ_{Di} is the ion Debye length, and $b = Z_{d0}e^2/T_i$. Equations (3) and (4) for the values ν_{ch} and $\tilde{\nu}$ are valid for $v_i/c_s < 1$.

As in [11], the electron density is taken to be of the Boltzmann form with a constant electron temperature

$$n_e = n_{e0}\exp\left(\frac{e\varphi}{T_e}\right). \quad (5)$$

We also use the equations (see, e.g., [4])

$$\partial_{xx}^2\varphi = 4\pi e(n_e + Z_d n_d - n_i) \quad (6)$$

and

$$\partial_t q_d = I_e(q_d) + I_i(q_d) \quad (7)$$

for the electrostatic potential and the variation of the dust-particle charge, respectively. Here, the microscopic electron and ion grain currents (for equilibrium electrons and kinetic ions) are

$$I_e \approx -\pi a^2 e\left(\frac{8T_e}{\pi m_e}\right)^{1/2} n_e \exp\left(\frac{eq_d}{aT_e}\right) \quad (8)$$

and

$$I_i = \sqrt{\frac{\pi}{2}}a^2 v_{Ti} e n_i\left[2\exp\left(-\frac{v_i^2}{2v_{Ti}^2}\right) + \sqrt{2\pi}\frac{v_{Ti}}{v_i}\left(1 + \frac{v_i^2}{v_{Ti}^2} - \frac{2eq_d}{am_i v_{Ti}^2}\right)\mathrm{erf}\left(\frac{v_i}{\sqrt{2}v_{Ti}}\right)\right]; \quad (9)$$

m_e is the electron mass and erf(x) is the error function.

The set of Eqs. (1)–(7) describes the evolution of perturbation and its transformation into nonlinear wave structure. The only steady-state solution of this set of equations corresponds to the unperturbed plasma parameters. Thus, the evolution of perturbation within the ionization-source model can lead only to the appearance of a nonstationary nonlinear ion acoustic wave structure.

Let us consider the evolution of a nonmoving region with a constant enhanced ion density within the framework of the above (ionization-source) model. In this consideration, we apply the data close to those of the University of Iowa laboratory experiment [9].

This experiment was performed in a Q machine device that was modified to allow the introduction of dust grains into the plasma. The experiment was conducted with Cs^+ ions. The plasma parameters in the experiment were $T_e \approx T_i \approx 0.2$ eV, $n_{i0} \sim 10^6$–10^7 cm^{-3}, and $a \sim 0.1$–1 μm. The parameter $\epsilon Z_{d0} = n_{d0}Z_{d0}/n_{i0}$ was varied from 0 to 0.95. This corresponds to the variation of the parameter $Z_{d0}d$ from 0 to 19. The evolution of large-amplitude density pulses propagating in complex plasmas was investigated. In the presence of a substational component of negatively charged dust (when $\epsilon Z_{d0} \geq 0.75$; i.e., $Z_{d0}d \geq 3$) a sharpening up of the leading edge of the pulse as it propagates down the plasma column (shock formation) was observed.

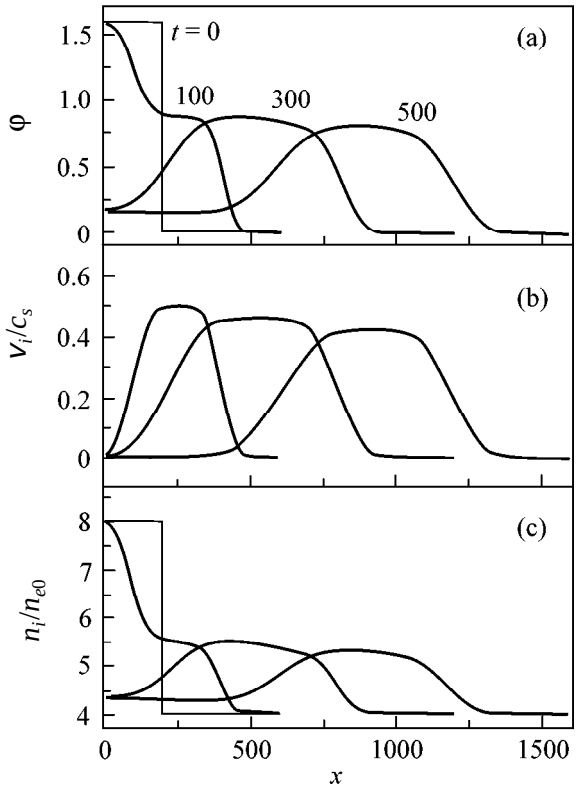

Fig. 1. The profiles of $\varphi(x)$, $v_i(x)/c_s$, and $n_i(x)/n_{e0}$ at $t = 100$, 300, and 500 showing the evolution of the initial perturbation obtained within the ionization-source model. The parameters are $Z_{d0}d = 3$, $T_e = T_i = 0.2$ eV, $a = 0.1$ μm, and $n_{e0} = 2.56 \times 10^6$ cm^{-3}. The initial normalized dust-particle charge number is $z_0 \approx 3.36$. The initial profiles ($t = 0$) of the potential φ and the normalized ion density n_i/n_{e0} are presented by the thin lines at the left of the figures.

The results of the calculations on the basis of the proposed ionization-source model, which describe the evolution of the initial nonmoving region with a constant enhanced ion density within the set of Eqs. (1)–(7) are given in Figs. 1 and 2. We use the normalization $x/\lambda_D \longrightarrow x$ for the spatial variable and $tc_s/\lambda_D \longrightarrow t$ for the time variable, where $c_s = \sqrt{T_e/m_i}$ is the ion acoustic speed. The plasma parameters are $Z_{d0}d = 3$, $T_e = T_i = 0.2$ eV, $a = 0.1$ μm, and $n_{e0} = 2.56 \times 10^6$ cm^{-3}. The ini-

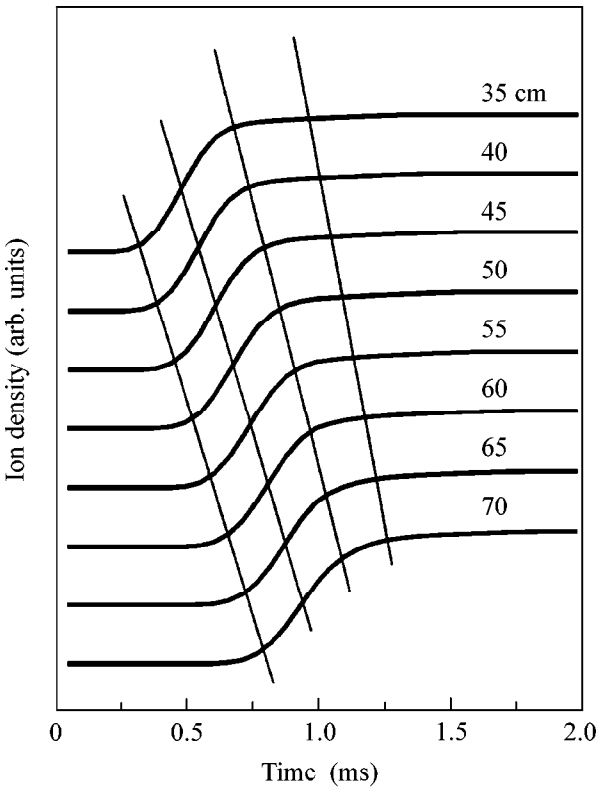

Fig. 2. Ion density vs. time for different axial positions from the grid. The parameters are the same as in Fig. 1. The profiles of the perturbations are shown by bold lines. The sets of thin lines indicate some steepening (shock formation).

tial ion density in the perturbation is two times larger than the background one, which corresponds to the case of Fig. 2b in [9]. The initial charge of the dust particles is the equilibrium one in the absence of wave perturbations ($z_0 \approx 3.36$). Figures 1a–1c show the profiles of the potential $\varphi(x)$, the ion speed normalized to the ion acoustic speed, and the ion density n_i normalized to the unperturbed electron density n_{e0} at the instants of time $t = 100$, 300, and 500. The initial profiles ($t = 0$) of the potential φ and the normalized ion density n_i/n_{e0} are presented by thin lines at the left of the corresponding figures. We see that the relationship $v_i/c_s < 1$ remains valid in the process of the evolution of the perturbation. Thus, the use of Eqs. (3) and (4) for the values ν_{ch} and $\tilde{\nu}$ is justified.

From Figs. 1a–1c, we see that the evolution of an intense initial nonmoving region with a constant enhanced ion density results in an appearance of a shock wave structure. For $t > 200$, the speed of the structure is approximately constant ($M \approx 1.94$). The width of the shock front is on the order of $\Delta\xi \sim 100\lambda_D \sim$ 20 cm. This value is in good agreement with the theoretical estimate [6] $\Delta\xi \sim c_s/\nu_q$ for the width of the front of shocks related to dust-particle charging. For comparison with the data of the experiment [9], we have to find the width of the front calculated in terms of the time variables $\Delta\xi/Mc_s \sim 0.3$ ms. This value corresponds to the observed one (see Fig. 2b in [9]). Thus, the proposed ionization-source model allows one to obtain shock structures as a result of the evolution of an initial perturbation and to explain the width of the shock front. This means that the shocks observed in [9] are related to the anomalous dissipation due to the dust-particle charging process.

Figure 2 is constructed by analogy with Fig. 2b in [9]. It shows the dependence of the ion density on time for different axial positions from the grid of the experimental installation [9] (the grid is used to separate the region of enhanced ion density from the background one in a *Q* machine device). The profiles of the perturbations are shown by bold lines. The sets of thin lines indicate some steepening (shock formation). The computational results presented in Fig. 2 are in good qualitative and quantitative agreement with the experimental ones shown in Fig. 2b in [9]. In particular, this concerns the width of the shock front (as mentioned, the calculated value corresponds to the observed one). Furthermore, the experimental profiles of the perturbations at large distances from the grid (60, 65, and 70 cm) are similar to each other (see Fig. 2b in [9]). This indicates the fact that at large distances from the grid a quasi-steady-state shock structure is formed. An analogous statement for the theoretical results can be made on the basis of Fig. 2. Finally, the comparison of these two figures allows us to conclude that the velocity of perturbation predicted by theory on the basis of the ionization-source model is close to the experimentally observed value.

To summarize, we have considered the nonstationary problem of the evolution of perturbation and its transformation into nonlinear wave structure. From this consideration, we have developed the one-dimensional (ionization-source) model which takes into account the variation of ion density and the ion-momentum dissipation due to dust-particle charging, as well as the source of plasma particles due to the ionization process. We have performed the consideration of the evolution of a nonmoving region with a constant enhanced ion density within the framework of the ionization-source model for the data of the laboratory experiment [9]. This consideration has shown that this model allows one to obtain shock structures as a result of evolution of an initial perturbation and to explain the experimental value of the width of the shock-wave front, as well as the shock-wave speed. This indicates that the shocks observed in [9] are related to the anomalous dissipation due to the dust-particle charging process. In the future, we intend to carry out the description of the experiment [9] in more detail using the modified ionization-source model, which additionally includes the effects of Landau damping of ion acoustic waves and ion–neutral collisions.

This work was supported by the INTAS (grant no. 97-2149) and the INTAS-RFBR (grant no. IR-97-775).

REFERENCES

1. V. N. Tsytovich, Usp. Fiz. Nauk **167**, 57 (1997) [Phys. Usp. **40**, 53 (1997)].
2. Ya. B. Zel'dovich and Yu. P. Raizer, *Physics of Shock Waves and High-Temperature Hydrodynamic Phenomena* (Nauka, Moscow, 1966, 2nd ed.; Academic, New York, 1967).
3. R. Z. Sagdeev, in *Reviews of Plasma Physics*, Ed. by M. A. Leontovich (Atomizdat, Moscow, 1964; Consultants Bureau, New York, 1966), Vol. 4, p. 23.
4. S. I. Popel, M. Y. Yu, and V. N. Tsytovich, Phys. Plasmas **3**, 4313 (1996).
5. S. I. Popel, V. N. Tsytovich, and M. Y. Yu, Astrophys. Space Sci. **256**, 107 (1998); in *Plasma Physics*, Ed. by P. Martin and J. Puerta (Kluwer, Dordrecht, 1998), p. 107.
6. S. I. Popel, A. A. Gisko, A. P. Golub', *et al.*, Phys. Plasmas **7**, 2410 (2000).
7. Y. Nakamura, H. Bailung, and P. K. Shukla, Phys. Rev. Lett. **83**, 1602 (1999).
8. P. K. Shukla, Phys. Plasmas **7**, 1044 (2000).
9. Q.-Z. Luo, N. D'Angelo, and R. L. Merlino, Phys. Plasmas **6**, 3455 (1999).
10. S. I. Popel and V. N. Tsytovich, Astrophys. Space Sci. **264**, 219 (1999).
11. J. Goree, G. E. Morfill, V. N. Tsytovich, and S. V. Vladimirov, Phys. Rev. E **59**, 7055 (1999).
12. S. I. Popel and M. Y. Yu, Contrib. Plasma Phys. **35**, 103 (1995).
13. S. I. Popel and M. Y. Yu, Phys. Rev. E **50**, 3060 (1994).
14. F. F. Chen, in *Plasma Diagnostic Techniques*, Ed. by R. H. Huddlestone and S. L. Leonard (Academic, New York, 1965), Chap. 4.
15. M. S. Barnes, J. H. Keller, J. C. Forster, *et al.*, Phys. Rev. Lett. **68**, 313 (1992).
16. S. Benkadda, P. Gabbai, V. N. Tsytovich, and A. Verga, Phys. Rev. E **53**, 2717 (1996).
17. M. A. Lieberman and A. J. Lichtenberg, *Principles of Plasma Discharges and Material Processing* (Wiley, New York, 1994), p. 454.

JETP Letters, Vol. 73, No. 5, 2001, pp. 228–231. Translated from Pis'ma v Zhurnal Éksperimental'noĭ i Teoreticheskoĭ Fiziki, Vol. 73, No. 5, 2001, pp. 263–267.

Band Gap Collapse and Ultrafast "Cold" Melting of Silicon during Femtosecond Laser Pulse

S. I. Kudryashov and V. I. Emel'yanov

International Laser Center, Faculty of Physics, Moscow State University, Moscow, 119899 Russia

e-mail: sergeikudryashov@chat.ru

Received January 18, 2001

It is established experimentally that a high concentration of electron–hole plasma produced in silicon by femtosecond laser pulse induces a sequential "collapse" of the band gap in the [111] and [100] directions and leads to the formation of a "cold" metallic liquid phase during the pulse. © *2001 MAIK "Nauka/Interperiodica".*

PACS numbers: 78.47.+p

1. Femtosecond laser pulses are capable of producing high-density electron–hole plasma [1, 2] that destabilizes the crystal structure of semiconductors. Various types of subpicosecond structural transitions into a new crystal or metallic liquid phase were predicted for such a strongly excited semiconductor state [3–7].

Ultrafast structural transitions into the metallic liquid phase in Si, GaAs, and InSb and the crystal phase in amorphous $Ge_{0.04}Sb_{0.96}$ were repeatedly observed with a time delay of several hundreds of femtoseconds after the pump pulse (see [8] for bibliography) and interpreted as nonthermal phenomena. An alternative explanation for transitions with such a time delay consists in the ultrafast transfer of kinetic energy to the lattice in an amount exceeding the enthalpy of melting in a substance [5, 7] and destabilizing the acoustic phonon-mode continuum.

Owing to the instability of some optical or acoustic modes, the nonthermal structural transitions may proceed in a time on the order of a period of lattice vibrations (10^{-13} s), with the transition time decreasing as the concentration of electron–hole plasma increases [6]. Consequently, one may, in principle, observe the nonthermal structural transitions for a laser pulse of a duration of 100 fs, provided that the energy density per pulse far exceeds the instability threshold for certain lattice modes in a semiconductor. To our knowledge, this possibility has not been experimentally implemented so far.

In this work, experimental data were obtained by the time-resolved methods of femtosecond pump-pulse self-reflection (FH, $\hbar\omega = 1.56$ eV) and linear reflection of probing second-harmonic (SH, $\hbar 2\omega = 3.12$ eV) and analyzed to prove that plasma-induced band-gap (E_g) "collapse" and nonthermal silicon melting occur during a laser pulse of 100 fs.

2. A standard femtosecond laser setup of the Institute of Laser and Plasma Physics (Essen, Germany), analogous to that described in [9], was used in the work. The laser output at a wavelength of 800 nm (FH), (Gaussian) pulse duration $\tau = 100$ fs (FWHM), a repetition rate of 10 Hz, and relative amplitudes of spurious pulses no higher than 5–7% was 1.5 mJ per pulse (TEM_{00}) and led into the pump and probe channels.

The FH in the pump channel was focused and directed at an angle of 45° onto an undoped silicon Si(100) target placed on a two-coordinate stepping motor-driven translational (from pulse to pulse) stage. The energies of mirror-reflected *s*- and *p*-polarized pump beams were measured by a pyroelectric detector. The time delay in the probe channel was set optically, and after frequency doubling SH was filtered and used at normal incidence on the Si target for probing, through the lens of optical microscope, the target area excited by the pump pulse [10]. A mirror-reflected-SH image of the target was recorded by a synchronized video camera. The characteristics of the probe channel allowed the target reflectivity transients to be studied with a spatial resolution of 2 μm and a time resolution of about 100 fs.

In the experiments, the pump-beam (FH, ω) self-reflectivity was studied as a function of the pulse energy for both beam polarizations and the reflectivity transients of the probe SH (2ω) were examined at a fixed maximum fluence of the *p*-polarized pump pulse.

3. The coefficients R_s^ω and R_p^ω of the pump-beam self-reflection from silicon were measured as functions of pulse energy for both beam polarizations, and the corresponding dependences were processed using the appropriate spatial transformation (*X* transformation) to obviate the averaging of this coefficient because of the inhomogeneity of the fluence *F* in the beam spot on the target (Gaussian distribution with parameters $\sigma_x = 73$ μm and $\sigma_y = 43$ μm). The resulting R_{1s}^ω and R_{1p}^ω coefficients are presented in Fig. 1 as functions of the

effective (pulse-integrated) pulse fluence $F_{\text{eff}} = (1 - R^{\omega}_{1s,\,p})F$. This representation allows the portions of the R^{ω}_{1s} and R^{ω}_{1p} curves corresponding to the identical excitation conditions to be juxtaposed in a common plot.

Due to the laser "self-action" effect [2, 4], which manifests itself in the variation of optical characteristics of a semiconductor during the pump pulse, the dependences of R^{ω}_{1s} and R^{ω}_{1p} on F_{eff} prove to be averaged over the pulse time. These curves were subjected to the additional graphical processing (temporal T transformation) according to the formulas

$$R_1(F_{\text{eff}}) = \frac{\int_{F_{\text{eff1}}}^{F_{\text{eff2}}} R_2(F')dF'}{\int_{F_{\text{eff1}}}^{F_{\text{eff2}}} dF'}, \quad (1)$$

$$R_2(F_{\text{eff}}) = R_1(F_{\text{eff}}) + (dR_1(F_{\text{eff}})/dF_{\text{eff}})F_{\text{eff}}, \quad (2)$$

where R^{ω}_{2s} and R^{ω}_{2p} (Fig. 1) are the "true" silicon reflectivities corresponding to the instantaneous $F_{\text{eff}}(t)$ value equal to the emission intensity integrated to time t of the pulse and the F_{eff1} and F_{eff2} values define the integration limits for which this transformation is valid. Note that, according to Eqs. (1) and (2), the T transformation of the R^{ω}_{1s} and R^{ω}_{1p} functions of F_{eff} implies that excitation is a transient process for which the diffusion and recombination contributions to the kinetic equation for electron–hole plasma density can be ignored. The first can be done if $\alpha l_{\text{dif}} \ll 1$, where $l_{\text{dif}} \sim 10$ nm is the plasma diffusion length during the pulse and α^{-1} is the skin depth of the excited semiconductor. The second (recombination) contribution can be ignored at a moderate ($F_{\text{eff}} \le 0.5$ J cm^{-2}) fluence of a femtosecond pulse for which the density of the electron–hole plasma reaches a value (on the order of 10^{22} cm^{-3} [5]) that is critical for the destabilization of the semiconductor lattice but still lower than the equilibrium plasma density for the competing optical-generation and Auger processes (see below).

Optical diagnostics of the excited Si was also carried out at a normal incidence of the probe SH. The reflected-probe-beam images of the silicon sample were normalized, with the use of a computer program, to the image of the unexcited sample for several time delays between the pump and probe pulses and represented, after calibration, a two-dimensional array of reflection coefficients distributed symmetrically about the center of the pump beam spot. After the reduction of space coordinates, the vertical cross sections passing through the center of the spot in the normalized images

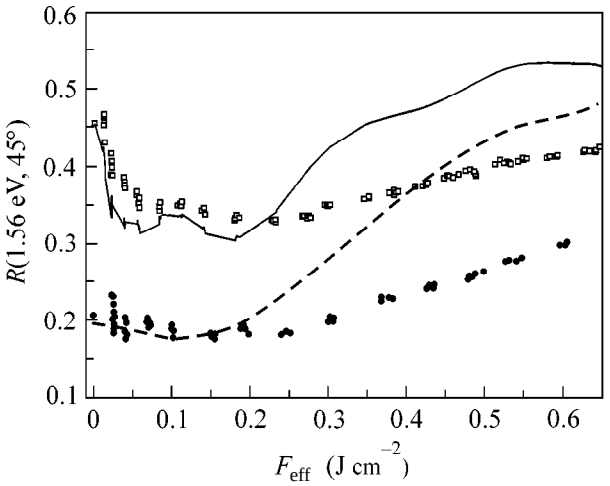

Fig. 1. Self-reflection coefficients of Si for the *s*- and *p*-polarized pump beams (FH) vs. the integrated effective fluence F_{eff}: (light squares) R^{ω}_{1s} and (dark circles) R^{ω}_{1p}. The same as functions of the instantaneous effective fluence $F_{\text{eff}}(t)$: (solid line) R^{ω}_{2s} and (dashed line) R^{ω}_{2p}.

characterize the dependence of $R_1^{2\omega}$ on the integrated F_{eff} characteristic (Fig. 2). Inasmuch as the probe- and pump-pulse durations were virtually identical, the time resolution higher than 100 fs was obtained for small time delays (–100–100 fs) by applying the procedure of obviating the averaging of $R_1^{2\omega}$ for times shorter than the probe-pulse duration; in so doing, the probe-pulse shape was approximated by a rectangle with a width of 100 fs (FWHM of the real pulse). The T transformation described above was applied to the $R_1^{2\omega}$ curve for zero time delay, i.e., for the coinciding probe and pump pulses.

The resulting $R^{\omega}_{2s}(F_{\text{eff}}(t))$ and $R^{\omega}_{2p}(F_{\text{eff}}(t))$ curves exhibit a single broad minimum for the *p* polarization and two narrow minima in the same region for the *s* polarization at small $F_{\text{eff}}(t) \le 0.15$ J cm^{-2} values and a sharp rise at higher $F_{\text{eff}}(t)$ values (Fig. 1). Likewise, the dependence of $R_2^{2\omega}$ on $F_{\text{eff}}(t)$, shown by the heavy line in Fig. 2, shows two small minima preceded by maxima at the same $F_{\text{eff}}(t)$ values in the indicated region. It is worth noting that a single minimum followed by the ascending portion was repeatedly observed in the experimental linear reflectivity vs. fluence curves of semiconductors and treated as an indication of reaching the plasma reflection edge [1, 2]. However, the presence of two resolved minima observed for R^{ω}_{2s} in this work calls for new interpretation of these features. To this end, the R^{ω}_{2s} and R^{ω}_{2p} dependences were used to calculate the optical constants n^{ω} and k^{ω} of excited Si

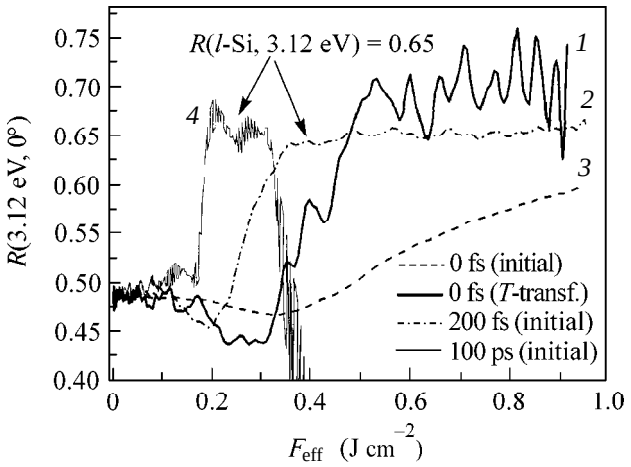

Fig. 2. Reflection coefficient of Si for the probe SH beam vs. the effective fluence for different time delays: (*1, 2*) $R_1^{2\omega}(F_{\text{eff}})$ (initial) and $R_2^{2\omega}(F_{\text{eff}}(t))$ (*T*-transformed) for zero time delay; (*3*) $R_1^{2\omega}(F_{\text{eff}})$ for a time delay of 200 fs; and (*4*) $R_1^{2\omega}(F_{\text{eff}})$ for a time delay of 100 ps. The peak in curve *4* corresponds to the reflectivity of the silicon melt area not subjected to ablation.

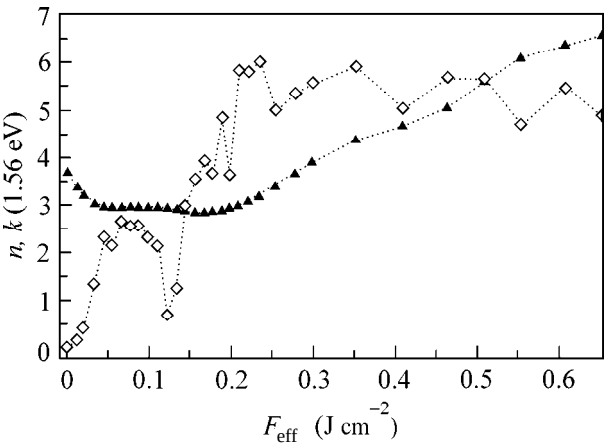

Fig. 3. Real n^{ω} (dark triangles) and imaginary k^{ω} (light rhombi) parts of the refractive index of Si vs. the instantaneous fluence density $F_{\text{eff}}(t)$.

for different $F_{\text{eff}}(t)$ values (Fig. 3). The calculations were carried out by using the Fresnel formulas and choosing those pairs of n^{ω} and k^{ω} values which minimize the difference between the calculated and experimental values of R_{2s}^{ω} and R_{2p}^{ω}.

One can see from Fig. 3 that two minima in the R_{2s}^{ω} curve correspond to two intense linear absorption bands at $F_{\text{eff}}(t) \approx 0.07$ and 0.17 J cm^{-2}. Note that the two-photon absorption and the free-carrier absorption can be ignored for Si in the range 0.05–0.2 J cm^{-2} [11] because both are weaker than the residual absorption between the peaks in the $k^{\omega}(F_{\text{eff}}(t))$ curve. The position and height of the first maximum in $k^{\omega}(F_{\text{eff}}(t))$ agree well with the data in [11], but the second maximum has not been observed previously. Taking into account the effect of plasma-induced red shift in the linear absorption spectra of semiconductors with high-density electron–hole plasma [12, 13], we assume that both interband absorption bands E_1 and E_2 ($L_3 \longrightarrow L_1$ and $X_4 \longrightarrow X_1$ transitions in Si) with maxima at, respectively, 3.4 and 4.3 eV [14] are recorded during the pump pulse in this work. An analysis carried out using the sum rule for the optical conductivity $\sigma(F_{\text{eff}}(t))$ of excited silicon and frequency-dependent $\sigma(\omega)$ of unexcited silicon (constructed using the data in [14]) showed that the peaks in the $k^{\omega}(F_{\text{eff}}(t))$ curve in Fig. 3 correlate with the silicon $E_{1,2}$ bands to within 5%. In particular, the red shift of the $L_{3'} \longrightarrow L_1$ transition is initiated by two-photon absorption [11], which then gives way to the intense linear absorption as E_g[111] decreases.

It is also evident from the $n^{\omega}(F_{\text{eff}}(t))$ and $k^{\omega}(F_{\text{eff}}(t))$ curves that the intense generation of electron–hole plasma above the threshold $F_{\text{eff}}(t) \approx 0.23$ J cm^{-2} initiates the ultrafast nonthermal melting in Si during the laser pulse (jumps in R_{2s}^{ω} and R_{2p}^{ω} in Fig. 1). This follows from the correspondence of the $n^{\omega}(F_{\text{eff}}(t))$ and $k^{\omega}(F_{\text{eff}}(t))$ values calculated in the range $F_{\text{eff}}(t) \geq 0.23$ J cm^{-2} (Fig. 3) to the optical constants of the equilibrium liquid phase *l*-Si: $n(1.5\text{ eV}) = 3.3$ and $k(1.5\text{ eV}) = 5.7$ [15]. The ratio of the thermal melting threshold $F_{\text{eff}} \approx 0.16$ J cm^{-2} (peak in the $R_1^{2\omega}$ curve for 100 ps in Fig. 2) to the nonthermal melting threshold $F_{\text{eff}}(t) \approx 0.23$ J cm^{-2} in Si equals approximately 1.5 and corresponds to the analogous data for Si and GaAs [16]. Note that, compared to the R_{2s}^{ω} and R_{2p}^{ω} curves in Fig. 1, the $R_2^{2\omega}$ curve for zero time delay has an additional minimum at $F_{\text{eff}}(t) \geq 0.23$ J cm^{-2} (Fig. 2). This feature of $R_2^{2\omega}$ can be explained by the metal–insulator transition near the plasma frequency ω_p of a cold metallic Si melt, provided that $\omega < \omega_p \leq 2\omega$. Finally, the $R_2^{2\omega}$ curve in Fig. 2, as also R_{2s}^{ω} and R_{2p}^{ω} in Fig. 1, tends at $F_{\text{eff}}(t) \geq 0.5$ J cm^{-2} to a saturation at a level of 0.66, corresponding to the reflection coefficient of the equilibrium thermal *l*-Si melt at a time delay of 100 ps and its nonequilibrium melt at 200 fs (Fig. 2). The above-mentioned plateaus in $R_2^{2\omega}$, R_{2s}^{ω}, and R_{2p}^{ω} correspond to a "resistively saturated" liquid phase of Si, for which $\omega\tau_{ee} \ll 1$ (τ_{ee} is the characteristic time of electron–electron collisions). This conclusion follows from the fact that the photoconductivity σ^{ω} calculated with the use of the $n^{\omega}(F_{\text{eff}}(t))$ and $k^{\omega}(F_{\text{eff}}(t))$ dependences tends at

$F_{\text{eff}}(t) \geq 0.5$ J cm^{-2} to a value equal to the static conductivity of equilibrium *l*-Si (10.9 PHz [15]) as a result of a strong decrease in τ_{ee} upon melt heating.

A steady decrease in E_g for the $L_{3'} \longrightarrow L_1$ and $X_4 \longrightarrow X_1$ transitions in Si with increasing $F_{\text{eff}}(t)$, as is evident from the sequential appearance of the $E_{1,2}$ bands, can be induced by both electronic [13] and structural [3, 5–6] effects. The upper bounds for the densities of electron–hole plasma at the blue edges of the $E_{1,2}$ bands [$F_{\text{eff}}(t) \approx 0.1$ and 0.2 J cm^{-2}] can be estimated from the condition that the rates of optical generation and Auger processes ($\gamma_A = 4 \times 10^{-31}$ cm^6 s^{-1} [6]) are equalized. That is, at the upper limit of applicability of the *T* transformation, the expression

$$N_{e-h}(F_{\text{eff}}) = \sqrt[3]{\frac{\alpha(F_{\text{eff}})F_{\text{eff}}}{\hbar\omega\gamma_A\tau}} \qquad (3)$$

yields, respectively, 1.4×10^{22} and 2×10^{22} cm^{-3} for the corresponding values of $F_{\text{eff}}(t)$ and absorption coefficient $\alpha = 2\omega k^{\omega}/c$ of excited Si (data for k^{ω} are in Fig. 3). These plasma densities satisfy both the condition for the collapse of a $E_g \approx 3$–4 eV band gap as a result of ion-core screening and many-particle interactions in the electron–hole plasma [13] and the condition for lattice destabilization in Si [3, 5]. In the latter case, the steady decrease in E_g in the [111] or [100] direction during the laser pulse can be explained by the fact that the interatomic distances almost simultaneously increase within the skin depth, as is evident from the instantaneous formation of an "optically thick" layer in the melt (Fig. 3). This is caused by the presence of the appropriate "soft" longitudinal optical modes [6]. The presence of a soft mode is an indication of a structural second- order phase transition from the metastable diamond structure of excited Si, probably, to the orthorhombic structure of a semimetal ($E_g[111] = 0$) and, with a further increase in $F_{\text{eff}}(t)$, to a disordered liquid metallic phase. The formation of a metallic phase with the tetragonal structure of optical tin [3], whose optical constants are unknown to us, is also possible. It should be noted that the phenomena described in this work were also observed by us in a GaAs(100) sample.

4. In summary, the effects of sequential band-gap collapse in the [111] and [100] directions of Si followed by the formation of a cold metallic liquid phase during the 100-fs laser pulse have been experimentally observed in this work.

We are grateful to D. von der Linde, K. Sokolowski-Tinten, and V.V. Temnov for fruitful discussions an assistance in experiments and to the German Academic Exchanges Service for a partial support (in 1999–2000).

REFERENCES

1. C. V. Shank, R. Yen, and C. Hirliman, Phys. Rev. Lett. **50**, 454 (1983).
2. K. Sokolowski-Tinten and D. von der Linde, Phys. Rev. B **61**, 2643 (2000).
3. Yu. V. Kopaev, V. V. Menyaĭlenko, and S. N. Molotkov, Fiz. Tverd. Tela (Leningrad) **27**, 3288 (1985) [Sov. Phys. Solid State **27**, 1979 (1985)].
4. S. V. Govorkov, V. I. Emel'yanov, and I. L. Shumay, Laser Phys. **2**, 77 (1992).
5. P. Stampfli and K. H. Bennemann, Phys. Rev. B **42**, 7163 (1990).
6. V. I. Emel'yanov and D. V. Babak, Fiz. Tverd. Tela (St. Petersburg) **41**, 1462 (1999) [Phys. Solid State **41**, 1338 (1999)].
7. A. Gambirasio, M. Bernasconi, L. Colombo, *et al.*, Phys. Rev. B **61**, 8233 (2000).
8. K. Sokolowski-Tinten, J. Solis, J. Bialkowski, *et al.*, Phys. Rev. Lett. **81**, 3679 (1998).
9. *Femtosecond Laser Pulses: Principles and Experiments*, Ed. by C. Rulliere (Springer-Verlag, Berlin, 1998).
10. M. C. Downer, R. L. Fork, and C. V. Shank, J. Opt. Soc. Am. B **42**, 595 (1985).
11. D. H. Reitze, T. R. Zhang, Wm. M. Wood, *et al.*, J. Opt. Soc. Am. B **7**, 84 (1990).
12. E. N. Glezer, Y. Siegal, L. Huang, *et al.*, Phys. Rev. B **51**, 6959 (1995).
13. K. F. Berggren and B. E. Sernelius, Phys. Rev. B **24**, 1971 (1981).
14. *Handbook of Optical Constants of Solids*, Ed. by E. D. Palik (Academic, Orlando, 1985).
15. K. M. Shvarev, B. A. Baum, and N. V. Gel'd, Fiz. Tverd. Tela (Leningrad) **16**, 3246 (1974) [Sov. Phys. Solid State **16**, 2111 (1974)].
16. K. Sokolowski-Tinten, J. Bialkowski, M. Boing, *et al.*, Phys. Rev. B **58**, 11805 (1998).

Translated by V. Sakun

JETP Letters, Vol. 73, No. 5, 2001, pp. 232–236. Translated from Pis'ma v Zhurnal Éksperimental'noĭ i Teoreticheskoĭ Fiziki, Vol. 73, No. 5, 2001, pp. 268–273.

Fermi-Condensate Quantum Phase Transition in High-T_c Superconductors

M. Ya. Amusia[1,3] and V. R. Shaginyan[2,3]

[1] *Ioffe Physicotechnical Institute, Russian Academy of Sciences, Politekhnicheskaya ul. 26, St. Petersburg, 194021 Russia*
[2] *Institute of Nuclear Physics, Russian Academy of Sciences, Gatchina, Leningradskaya region, 188350 Russia*
e-mail: vrshag@thd.pnpi.spb.ru
[3] *The Racah Institute of Physics, Hebrew University, Jerusalem 91904, Israel*

Received January 22, 2001

The effect of a quantum phase transition associated with the appearance of fermionic condensation in an electron liquid on the properties of superconductors is considered. It is shown that the electron system in both superconducting and normal states exhibits characteristic features of a quantum protectorate after the point of this Fermi-condensate quantum phase transition. The single-particle spectrum of a superconductor can be represented by two straight lines corresponding to two effective masses M^*_{FC} and M^*_L. The M^*_{FC} mass characterizes the spectrum up to the binding energy E_0, which is of the order of the superconducting gap in magnitude, and M^*_L determines the spectrum at higher binding energies. Both effective masses are retained in the normal state; however, $E_0 \simeq 4$ T. These results are used to explain some remarkable properties of high-T_c superconductors and are in good agreement with recent experimental data. © *2001 MAIK "Nauka/Interperiodica".*

PACS numbers: 71.27.+a; 74.20.Fg; 74.25.Jb

Recent experiments using angle-resolved photoemission electron spectroscopy gave accurate data on the dispersion of single-particle excitations over a wide range of binding energies [1–3]. These experiments were carried out with high-T_c superconductors $Bi_2Sr_2CaCu_2O_{8+\delta}$ differing in the doping level both at temperatures T below the critical temperature T_c of the decay of the superconducting state and at $T_c \le T$. It was inferred that the dispersion of quasiparticle excitations $\varepsilon(p)$, where p is the momentum, can be described in the energy range (–200–0) meV by two straight lines intersecting at the binding energy $E_0 \sim$ (50–70) meV [2, 3]. This circumstance directly points to the existence of a new energy scale in the self-energy part of the quasiparticle excitations at temperatures $T \le T_c$ and $T_c \le T$ [2]. Therefore, new additional constraints can be imposed on the theories that are in principle applicable to the description of properties of high-T_c superconductors. For example, such a scale is absent in the theories of normal [4] and marginal [5] Fermi liquids, as well as in the theory based on the idea of quasiparticle spin–charge separation [6]. The kink in the quasiparticle dispersion law described above could be explained by the interaction of quasiparticles with collective magnetic excitations [3, 7] that was observed in high-T_c superconductors in experiments on inelastic neutron scattering at $T \le T_c$ and described in the literature; see, for example, [8]. However, a dispersion kink is also observed at $T_c \le T$, when these collective excitations disappear. Moreover, these excitations are successfully described as inelastic neutron scattering from Cooper pairs [9], which is confirmed by other experimental results [10, 11]. With regard to this explanation of the physics of magnetic excitations, it is unlikely that these excitations can significantly affect the single-electron dispersion. Experimental data on the single-particle electron spectra of high-T_c superconductors with d-wave symmetry indicate that the perturbation of the superconducting phase and single-particle spectra by phonons, collective states, or impurities is very small. Therefore, this state can be described as a strongly collectivized quantum state or as a "quantum protectorate" [6, 12, 13]. From here, it may be inferred that the kink description proposed in [3, 7] is very likely contradictory to the quantum protectorate concept.

In this letter, we show that the dispersion kink can be explained based on the assumption that the electron system of high-T_c superconductor is after the point of the Fermi-condensate quantum phase transition. Thus, the Fermi-condensate quantum phase transition serves as the point separating a normal Fermi liquid from a strongly correlated liquid of a new type [14, 15] that fulfills the quantum protectorate requirements.

Let us start with a brief description of the properties of an electron system with a fermionic condensate. Consider a two-dimensional electron liquid in the superconducting state at $T = 0$ on a simple square crystal lattice, which we replace temporarily by a uniform positive charge. Then, the ground state energy

$E_{gs}[\kappa(\mathbf{p}), n(\mathbf{p})]$ is a functional of the order parameter of the superconducting state $\kappa(\mathbf{p})$ and occupation numbers $n(\mathbf{p})$ [16] and is determined by the known equation

$$E_{gs}[\kappa(\mathbf{p}), n(\mathbf{p})] = E[n(\mathbf{p})] + \int V_{pp}(\mathbf{p}_1, \mathbf{p}_2)\kappa(\mathbf{p}_1)\kappa^*(\mathbf{p}_2)\frac{d\mathbf{p}_1 d\mathbf{p}_2}{(2\pi)^4}. \quad (1)$$

The pairing interaction $V_{pp}(\mathbf{p}_1, \mathbf{p}_2)$ is assumed to be weak. The ground-state energy $E[n(\mathbf{p})]$ of the normal Fermi liquid is a functional of occupation numbers $n(\mathbf{p})$ [4], which, at $T = 0$, are related to the order parameter by the simple equation

$$n(\mathbf{p}) = v^2(\mathbf{p}); \quad \kappa(\mathbf{p}) = v(\mathbf{p})\sqrt{1 - v^2(\mathbf{p})}. \quad (2)$$

Minimizing the energy E_{gs} in Eq. (1) with respect to occupation numbers and taking into account Eq. (2), we obtain the equation

$$\varepsilon(\mathbf{p}) - \mu = \Delta(\mathbf{p})\frac{1 - 2v^2(\mathbf{p})}{2\kappa(\mathbf{p})}, \quad (3)$$

where the single-particle energy $\varepsilon(\mathbf{p})$ is determined by Eq. [4]

$$\varepsilon(\mathbf{p}) = \frac{\delta E[n(\mathbf{p})]}{\delta n(\mathbf{p})}, \quad (4)$$

and μ is the chemical potential. The superconducting gap is given by the equation

$$\Delta(\mathbf{p}) = -\int V_{pp}(\mathbf{p}, \mathbf{p}_1)\kappa(\mathbf{p}_1)\frac{d\mathbf{p}_1}{4\pi^2}. \quad (5)$$

Let us assume that the interaction $V_{pp} \longrightarrow 0$. Then, the gap $\Delta(\mathbf{p}) \equiv 0$, and Eq. (3) is reduced to the equation proposed in [14]

$$\varepsilon(\mathbf{p}) - \mu = 0, \quad \text{if} \quad 0 < n(\mathbf{p}) < 1; \quad p_i \le p \le p_f. \quad (6)$$

This equation defines a Fermi liquid of a new type for which the order parameter $\kappa(\mathbf{p})$ differs from zero in the L_{FC} range of momenta $p_i \le p \le p_f$; the occupation numbers $n(\mathbf{p}) = 1$ and 0 outside the L_{FC} range, as must be in the normal Fermi liquid. It follows from Eq. (6) that the effective mass M^*_{FC} of quasiparticles in the fermionic condensate is infinitely large in the L_{FC} range:

$$\frac{1}{M^*_{FC}} = \frac{1}{p}\frac{d\varepsilon(p)}{dp} = 0. \quad (7)$$

The effective mass M^*_L of normal quasiparticles with momenta $p < p_i$ is finite and is defined by the known equations [4]

$$\frac{1}{M^*_L} = \frac{1}{p}\frac{d\varepsilon(p)}{dp}\bigg|_{p \le p_i}. \quad (8)$$

It follows from Eqs. (7) and (8) that a fermionic system with a Fermi condensate is broken into two quasiparticle subsystems: the dispersionless part of the single-particle spectrum is occupied by the Fermi condensate in the momentum range L_{FC} and is adjoined by the subsystem that is occupied by quasiparticles of finite mass with momenta $p < p_i$. We will assume for simplicity that the Fermi condensate occupies a small part of the Fermi sphere $p_f - p_i \ll p_F$, where the Fermi momentum is related by the common equation $p_F = (3\pi^2\rho)^{1/3}$ to the particle density ρ. The Fermi condensate appears in an electron system at a low density when the effective electron–electron interaction constant is sufficiently large. In a common electron liquid, this constant is directly proportional to the dimensionless parameter $r_s = 9\pi/4p_F a_B$, where a_B is the Bohr radius. For simplicity, we will assume that it equals r_s. It was shown in [17] that the appearance of a Fermi condensate occurs in a system at a certain $r_s = r_{FC} < r_{\text{cdw}}$ and precedes the appearance of a charge-density wave, which takes place in a two-dimensional electron liquid at $r_{\text{cdw}} \simeq 6$–8 [18]. Thus, the Fermi-condensate phase transition occurs at $T = 0$ when the parameter r_s attains its critical value r_{FC} and represents a quantum phase transition. At $r_s > r_{FC}$ and $r_s - r_{FC} \ll r_{FC}$, the region $p_f - p_i$ occupied by the Fermi condensate is $(p_f - p_i)/p_F \sim r_s - r_{FC}$. This estimate is confirmed by calculations for simple models [19, 20].

Because the order parameter of a Fermi-condensate phase transition is $\kappa(\mathbf{p})$, the maximum value of the superconducting gap Δ_1 in a system with a Fermi condensate $\Delta_1 \sim V_{pp}$, as it follows from Eq. (5). It is pertinent to note that $\kappa(\mathbf{p})$ is determined in this case by the relatively strong particle–hole interaction or by the Landau amplitudes F_L. Therefore, the perturbation of the parameter $\kappa(\mathbf{p})$ can be neglected in the first order in $V_{pp}/F_L \ll 1$. It is self-evident that we assume the L_{FC} range to be sufficiently large, so that its perturbation is small compared with the size of this range. Considering that $T_c \simeq \Delta_1/2$ in the weak-coupling theory of superconductivity [20, 21], we obtain high T_c values for systems with a Fermi condensate [14]. At the same time, the single-particle spectrum in the range L_{FC} occupied by the Fermi condensate will be disturbed by the interaction V_{pp}. This perturbation is quite notable for the effective mass, because the value of $1/M^*_{FC}$ becomes finite. Simultaneously, the perturbation of the single-particle spectrum at $p < p_i$, as well as the effective mass M^*_L, can be neglected.

Let us use Eq. (3) for calculating M^*_{FC} by differentiating both sides of this equation with respect to the momentum p at $p = p_F$

$$\frac{p_F}{M^*_{FC}} \simeq \frac{\Delta_1}{4\kappa^3(p)}\frac{1}{p_f - p_i} = \frac{2\Delta_1}{p_f - p_i}. \quad (9)$$

When obtaining Eq. (9), we took into account the facts that $\kappa(p) = 1/2$ at $p = p_F$, the gap $\Delta(\mathbf{p})$ has a maximum

at the Fermi surface, and, hence, its derivative there equals zero. The derivative $dv(p)/dp$ was calculated with the use of Eq. (2) and the simple estimate $dn(p)/dp \simeq -1/(p_f - p_i)$. We may conclude that the electron system with a Fermi condensate in the superconducting state is, as before, characterized by two effective masses, and that the single-particle dispersion at $p \sim p_F$ can be approximated by two straight lines. Let us estimate the binding energy E_0 at which these lines intersect. Multiplying both sides of Eq. (9) by the difference $p_f - p_i$, we obtain

$$E_0 \simeq \frac{(p_f - p_i)p_F}{M^*_{FC}} \simeq 2\Delta_1. \quad (10)$$

It follows from this equation that the intersection point of the two straight lines approximating the spectrum does not depend on the difference $p_f - p_i$, although the effective mass M^*_{FC} is proportional to this difference. The calculation of M^*_{FC} at $T \longrightarrow T_c$ is completely similar to the preceding calculation; one should only take into account that now [21]

$$v^2(\mathbf{p}) = \frac{n(\mathbf{p}) - f(\mathbf{p})}{1 - 2f(\mathbf{p})}, \quad (11)$$

where

$$f(\mathbf{p}) = \frac{1}{1 + \exp(E(\mathbf{p})/T)};$$
$$E(\mathbf{p}) = \sqrt{(\varepsilon(\mathbf{p}) - \mu)^2 + \Delta^2(\mathbf{p})}. \quad (12)$$

With regard to the facts that the function $f(\mathbf{p})$ has a maximum at $p = p_F$ (and its derivative equals zero there) and $E(\mathbf{p}) \ll T$, simple transformations of Eqs. (11) and (12) give

$$\frac{d(v^2(p))}{dp} \simeq -\frac{2T}{E(p)(p_f - p_i)}. \quad (13)$$

Differentiating both sides of Eq. (3) with respect to the momentum and taking into account Eq. (13), we obtain

$$\frac{p_F}{M^*_{FC}} \simeq \frac{4T}{p_f - p_i}. \quad (14)$$

It directly follows from Eq. (14) that

$$E_0 \simeq \frac{(p_f - p_i)p_F}{M^*_{FC}} \simeq 4\ \mathrm{T}. \quad (15)$$

Considering that $2\Delta_1 \simeq T_c$, we conclude by comparing Eqs. (10) and (14) that the effective mass M^*_{FC} and E_0 weakly depend on the temperature at $T \leq T_c$.

It follows from the above consideration that the form of the single-particle spectrum $\varepsilon(\mathbf{p})$ and the order parameter $\kappa(\mathbf{p})$ are determined by the Fermi-condensate quantum phase transition and, therefore, their forms are universal. Actually, the amplitudes F_L define only the region L_{FC} occupied by the condensate after the point of the Fermi-condensate phase transition. These amplitudes are determined by the properties of the system under consideration, which already include the contribution from impurities, phonons, and other collective excitations. Finally, we may conclude that a system with a Fermi condensate is characterized by a universal form of the single-particle spectrum and possesses quantum protectorate features at $T \leq T_c$.

We now turn to the description of the system at $T > T_c$, which is given by the equation of the Fermi-liquid theory [4]

$$\frac{\delta(F - \mu N)}{\delta n(\mathbf{p}, T)} = \varepsilon(\mathbf{p}, T) - \mu(T) - T\ln\frac{1 - n(\mathbf{p}, T)}{n(\mathbf{p}, T)} = 0. \quad (16)$$

Here, F is free energy, which, as well as the energy E, is a functional of the occupation numbers $n(\mathbf{p}, T)$. The occupation numbers now depend on momentum and temperature, and the quasiparticle energy $\varepsilon(\mathbf{p}, T)$ is defined by Eq. (4). Assuming that $T_c = 0$ and $T \longrightarrow 0$ in Eq. (16) and that the occupation numbers differ from zero and unity in the range L_{FC}, we obtain that the term $T\ln(\ldots) \longrightarrow 0$, and Eq. (16) is reduced to Eq. (6) for a Fermi condensate [14]. If the interaction $V_{pp} = 0$, the Fermi-condensate phase transition is absent at any finite temperature. Actually, as shown above, the order parameter $\kappa(\mathbf{p})$ after the point of the Fermi-condensate phase transition differs from zero in the region L_{FC}, and the gap $\Delta(\mathbf{p}) \equiv 0$. From here, it is clear that the critical temperature of this transition equals zero. However, a trace of this quantum phase transition persists in its radical effect on the properties of the system up to temperatures $T \ll T_f$, where T_f is a temperature at which the effect of this phase transition disappears. For example, the system entropy can be taken as such a property, resulting in the estimate [20]

$$\frac{T_f}{\varepsilon_F} \sim \frac{p_f^2 - p_i^2}{p_F^2} \sim \frac{\Omega_{FC}}{\Omega_F}, \quad (17)$$

where Ω_{FC} is the volume occupied by the Fermi condensate, Ω_F is the volume of the Fermi sphere, and ε_F is the Fermi energy. Taking into account that the occupation numbers at $T \ll T_f$ are defined by Eq. (6) and $n(\mathbf{p}, T) = n(\mathbf{p})$, we obtain from Eq. (16)

$$\varepsilon(\mathbf{p}, T) - \mu(T) = T\ln\frac{1 - n(\mathbf{p})}{n(\mathbf{p})} \simeq T\frac{1 - 2n(\mathbf{p})}{n(\mathbf{p})}\Big|_{p \simeq p_F}. \quad (18)$$

Differentiating both sides of Eq. (18) with respect to the momentum p and using the estimate $dn(p)/dp \simeq -1/(p_f - p_i)$, we obtain the approximate value for the effective mass

$$\frac{p_F}{M^*_{FC}} \simeq \frac{4T}{p_f - p_i}\Big|_{T \ll T_f}. \quad (19)$$

Multiplying both sides of Eq. (19) by the difference $p_f - p_i$, we obtain for the parameter

$$E_0 \simeq 4\ \mathrm{T}. \tag{20}$$

Equations (19) and (20) indicate that the mass M^*_{FC} and the energy E_0 start to depend on temperature at $T_c \le T \ll T_f$. However, this dependence is very weak at $T \simeq T_c$, as is evident from a comparison of Eqs. (14), (15) and (19), (20). We may conclude that the system under consideration still possesses quantum protectorate features at these temperatures, because the spectrum of the system is determined by the solutions of Eq. (6) and the temperature. It is evident from Eqs. (18), (19), and (20) that this spectrum has a universal character and is weakly affected by phonons, collective states, etc.

We now turn to the description of the experimental data [2] using the results presented above. We return to the consideration of an electron system on a square lattice. Experimental studies showed that the Fermi surface in the case of the $Bi_2Sr_2CaCu_2O_{8+\delta}$ metal has the shape of an approximately regular circle with the center at the point (π, π) of the Brillouin zone filled with hole states [22]. A van Hove singularity is located in the vicinity of the $(\pi, 0)$ point, and an almost dispersionless section of the spectrum is observed in this region (see, for example, [22]). This allows the suggestion to be made that the Fermi condensate is disposed in the vicinity of this point [23]. The straight line $Y\Gamma$, which is known as the line of zeros of the Brillouin zone, passes through the points (π, π)–$(0, 0)$ at an angle of $\pi/4$ to the straight line $Y\overline{M}$ passing through the points (π, π)–$(\pi, 0)$. The density of states attains a minimum at the point of intersection of the $Y\Gamma$ line and the Fermi surface. The single-particle spectrum was measured along the lines parallel to $Y\Gamma$ [2] and $Y\overline{M}$ [3], from the line of zeros to the $Y\overline{M}$ line. As a result, it was shown that the parameter E_0 is constant for a given sample; that is, it does not depend on the angle ϕ reckoned from the line of zeros to $Y\overline{M}$. The angle (kink) between the straight line characterizing the part of the spectrum with the binding energy lower than E_0 and the straight line related to the spectrum with the binding energy higher than E_0 grows with increasing ϕ and with a decreasing doping level [2, 3]. This general pattern is retained at $T > T_c$ [2].

To describe these experimental data, we assume the following model: the volume of the Fermi condensate Ω_{FC} depends on the angle ϕ, $\Omega_{FC}(\phi) \sim (p_f(\phi) - p_i(\phi))p_F$, increases with increasing ϕ, and attains a maximum at $(\pi, 0)$. In addition, r_s grows with decreasing doping level and exceeds the critical value r_{FC} in the optimal doping region. Note that the values of r_s corresponding to the optimal doping level are close to r_{FC} [17, 24, 25], whereas strong fluctuations of the charge density or charge-density waves are observed in undoped samples [26]. From here, we may conclude that the formation of a Fermi condensate in copper oxides is a determinate process stemming from the general properties of a low-density electron liquid.

It follows from Eq. (15) that the energy E_0 does not depend on the angle ϕ at $T \le T_c$. It also follows from Eq. (14) that the kink increases with increasing ϕ, because the effective mass linearly depends on the difference $(p_f(\phi) - p_i(\phi))$. Comparing Eqs. (9), (10) and (14), (15), one can conclude that these properties weakly depend on temperature at $T \le T_c$. Equations (19) and (20) demonstrate that this behavior persists at $T_c \le T$; however, a temperature dependence appears. According to experimental data, $E_0 \simeq$ (50–70) meV [2, 3], which is in agreement with Eqs. (10) and (20), because $E_0 \simeq 2\Delta_1$ in these materials. The volume of the phase condensate Ω_{FC} in our model grows with increasing r_s, and the mass M^*_{FC} correspondingly increases, as evident from Eqs. (9) and (14). Hence, the dispersion kink in the single-particle spectrum must increase with increasing doping level. Because $E_0 \simeq 2\Delta_1$, the kink point must shift towards higher binding energies as the doping level decreases. All these results are in good agreement with experimental data [2, 3].

The line shape of a single-particle excitation is another important characteristic property of this excitation that can be measured experimentally. The line shape $L(q, \omega)$ is a function of two variables. Measurements carried out at a fixed binding energy $\omega = \omega_0$, where ω_0 is the energy of the single-particle excitation under study, determine the line shape $L(q, \omega = \omega_0)$ as a function of momentum q [1]. As shown above, the effective mass M^*_{FC} is finite at finite temperature. Therefore, the system behaves as a normal Fermi liquid characterized by a certain effective mass at energies $\omega \le 4$ T (or $\omega \le 2\Delta_1$ if $T < T_c$). Quasiparticles with energies of the order of temperature will be involved in rescattering processes, which determine the width of the single-particle excitation. As follows from Eq. (20), these are precisely the quasiparticles with mass M^*_{FC}, which leads to a width of the order of T [20]. It was this behavior that was observed in experiments on measuring the line shape at a fixed energy, when well-defined quasiparticles at the Fermi level were found even in the region of the $(\pi, 0)$ point [1]. The line shape can be determined differently as a function of the energy ω at a fixed momentum q [27]. At small ω, the line will have a characteristic maximum and width as well as in the case of fixed energy ω. At energies $\omega \ge 4$ T (or $\omega \ge 2\Delta_1$ if $T < T_c$), quasiparticles of mass M^*_L will come into play, which will lead to a growth of the function that determines the line shape. Thus, this line will have a characteristic shape: a maximum [24, 25], then a minimum, and then again a flat maximum. At the same time, one can use the Kramers–Krönig relations for con-

structing the imaginary part of the quasiparticle excitation self-energy, provided that the real part is known [3]. One can see from above that the real part is formed by two effective masses M^*_{FC} and M^*_L. As a result, we again arrive at the characteristic shape: a maximum, a minimum, and then again a flat maximum. This result is in qualitative agreement with the experiment [3, 27].

V. R. Sh. is grateful to the Racah Institute of Physics, Hebrew University of Jerusalem for hospitality.

This work was supported in part by the Russian Foundation for Basic Research, project no. 01-02-17189.

REFERENCES

1. T. Valla, A. V. Fedorov, P. D. Johnson, *et al.*, Science **285**, 2110 (1999); T. Valla, A. V. Fedorov, P. D. Johnson, *et al.*, Phys. Rev. Lett. **85**, 828 (2000).
2. P. V. Bogdanov, A. Lanzara, S. A. Kellar, *et al.*, Phys. Rev. Lett. **85**, 2581 (2000).
3. A. Kaminski *et al.*, cond-mat/0004482.
4. L. D. Landau, Zh. Éksp. Teor. Fiz. **30**, 1058 (1956) [Sov. Phys. JETP **3**, 920 (1956)].
5. C. M. Varma, P. B. Littlewood, S. Schmitt-Rink, *et al.*, Phys. Rev. Lett. **63**, 1996 (1989); C. M. Varma, P. B. Littlewood, S. Schmitt-Rink, *et al.*, Phys. Rev. Lett. **64**, 497 (1990); E. Abrahams and C. M. Varma, cond-mat/0003135.
6. P. W. Anderson, *The Theory of Superconductivity in the High T_c Cuprates* (Princeton Univ. Press, Princeton, 1997).
7. M. Eschrig and M. R. Norman, Phys. Rev. Lett. **85**, 3261 (2000).
8. H. F. Fong, P. Bourges, Y. Sidis, *et al.*, Nature **398**, 588 (1999).
9. A. A. Abrikosov, Physica C (Amsterdam) **244**, 243 (1995); A. A. Abrikosov, Phys. Rev. B **57**, 8656 (1998).
10. H. He *et al.*, cond-mat/0002013.
11. A. A. Abrikosov, Phys. Rev. B **52**, R15738 (1995); A. A. Abrikosov, cond-mat/9912394.
12. R. B. Laughlin and D. Pines, Proc. Natl. Acad. Sci. USA **97** (1), 28 (2000).
13. P. W. Anderson, cond-mat/0007185; cond-mat/0007287.
14. V. A. Khodel' and V. R. Shaginyan, Pis'ma Zh. Éksp. Teor. Fiz. **51**, 488 (1990) [JETP Lett. **51**, 553 (1990)].
15. G. E. Volovik, Pis'ma Zh. Éksp. Teor. Fiz. **53**, 208 (1991) [JETP Lett. **53**, 222 (1991)].
16. V. R. Shaginyan, Phys. Lett. A **249**, 237 (1998).
17. V. A. Khodel, V. R. Shaginyan, and M. V. Zverev, Pis'ma Zh. Éksp. Teor. Fiz. **65**, 242 (1997) [JETP Lett. **65**, 253 (1997)].
18. L. Świerkowski, D. Neilson, and J. Szymański, Phys. Rev. Lett. **67**, 240 (1991).
19. V. A. Khodel, V. R. Shaginyan, and V. V. Khodel, Phys. Rep. **249**, 1 (1994).
20. J. Dukelsky *et al.*, Z. Phys. **102**, 245 (1997); V. A. Khodel and V. R. Shaginyan, Condens. Matter Theor. **12**, 222 (1997).
21. E. M. Lifshitz and L. P. Pitaevskiĭ, *Course of Theoretical Physics*, Vol. 5: *Statistical Physics* (Nauka, Moscow, 1978; Pergamon, New York, 1980), Part 2.
22. H. Ding, A. F. Bellman, J. C. Campuzano, *et al.*, Phys. Rev. Lett. **76**, 1533 (1996); J. Mesot *et al.*, cond-mat/9910430.
23. V. A. Khodel, J. W. Clark, and V. R. Shaginyan, Solid State Commun. **96**, 353 (1995).
24. S. A. Artamonov and V. R. Shaginyan, Zh. Éksp. Teor. Fiz. **119**, 331 (2001) [JETP **92**, 287 (2001)]; cond-mat/0006013.
25. M. Ya. Amusia and V. R. Shaginyan, Phys. Lett. A **275**, 124 (2000).
26. G. Grüner, *Density Waves in Solids* (Addison-Wesley, Reading, 1994).
27. M. R. Norman, H. Ding, J. C. Campuzano, *et al.*, Phys. Rev. Lett. **79**, 3506 (1997).

Translated by A. Bagatur'yants

JETP Letters, Vol. 73, No. 5, 2001, pp. 237–241. From Pis'ma v Zhurnal Éksperimental'noĭ i Teoreticheskoĭ Fiziki, Vol. 73, No. 5, 2001, pp. 274–278.

Ginzburg–Landau-Type Theory of Antiphase Boundaries in Polytwinned Structures[1]

V. G. Vaks

Russian Research Center Kurchatov Institute, pl. Kurchatova 1, Moscow, 123182 Russia

e-mail: vaks@mbslab.kiae.ru

Received January 24, 2001

The conventional Ginzburg–Landau theory of interphase boundaries is generalized to values of order parameters that are not small, with application to polytwinned structures characteristic of cubic–tetragonal-type phase transitions. Explicit expressions for the structure and energy of antiphase boundaries via the functions entering the free-energy functional are given. A peculiar dependence of equilibrium orientations of antiphase boundaries on the interaction type is predicted, and it qualitatively agrees with the available experimental data. © *2001 MAIK "Nauka/Interperiodica".*

PACS numbers: 64.70.Kb; 61.50.Ks; 05.70.Fh

Ordering phase transitions between the cubic disordered and the tetragonal ordered phases are observed in many different solids. The known examples are the transitions between the disordered FCC phase (A1 phase) and the CuAu I-type ordered tetragonal phase ($L1_0$ phase) in a number of metallic alloys [1–3]; the ferroelectric transitions between the cubic paraelectric and the tetragonal ferroelectric phase in $BaTiO_3$-type perovskites [4], etc. A characteristic feature of such transitions is the formation in the ordered phase of so-called polytwinned structures consisting of arrays of ordered bands separated by antiphase boundaries (APBs) with (110)-type orientation, while the tetragonal axes of antiphase-ordered domains (APDs) in the adjacent bands have twin-related (100) and (010)-type orientations. As an example, Fig. 1 shows a typical microstructure of the $L1_0$ phase in CoPt alloys observed by Leroux *et al.* [1]. The formation of polytwinned structures is explained by the elimination of the volume-dependent part of the elastic energy for such structures [4–7] discussed below.

Studies of microstructural features of polytwinned structures, such as the properties and distribution of APBs, attract interest from both fundamental and applied points of view, in particular in connection with applications of such structures in various magnetic devices for which the structure and the distribution of APBs are very important [1–3]. Below, I present a Ginzburg–Landau-type theory that enables one to explicitly calculate the characteristics of APBs in polytwinned structures, both phenomenologically and microscopically.

To be definite, we consider the A1 $\longrightarrow$ $L1_0$ transition in a binary alloy A_cB_{1-c}. Different distributions of atoms over lattice sites i are described by the occupation numbers $\{n_i\}$, where $n_i = n_{Ai}$ is unity when the site i is occupied by atom A and zero otherwise. The mean occupation $\langle n_i \rangle = c_i = c(\mathbf{r}_i)$ (where $\mathbf{r}_i$ is the FCC lattice vector) in the homogeneous $L1_0$ phase can be written in terms of three long-ranged order parameters η_α, see, e.g., [7]:

$$c_i = c + \eta_1 \exp(i\mathbf{k}_1\mathbf{r}_i) + \eta_2 \exp(i\mathbf{k}_2\mathbf{r}_i) + \eta_3 \exp(i\mathbf{k}_3\mathbf{r}_i), \quad (1)$$

where $\mathbf{k}_\alpha$ is the superstructure vector corresponding to η_α:

$$\mathbf{k}_1 = [100]2\pi/a, \quad \mathbf{k}_2 = [010]2\pi/a, \quad \mathbf{k}_3 = [001]2\pi/a, \quad (2)$$

and a is the FCC lattice constant. Within each $L1_0$-ordered domain with a tetragonal axis α, only one nonzero parameter η_α is present, being either positive or negative. Therefore, six types of ordered domains are possible with two types of APB. The APB separating two APDs with the same tetragonal axis will be called for brevity the shift-APB, and the APB separating the APDs with perpendicular tetragonal axes will be called the flip-APB.

Below, I consider the weakly inhomogeneous states, for which quantities c and η_α in Eq. (1) are not constants but slowly varying functions of coordinates $\mathbf{r} = \mathbf{r}_i$

[1] This article was submitted by the author in English.

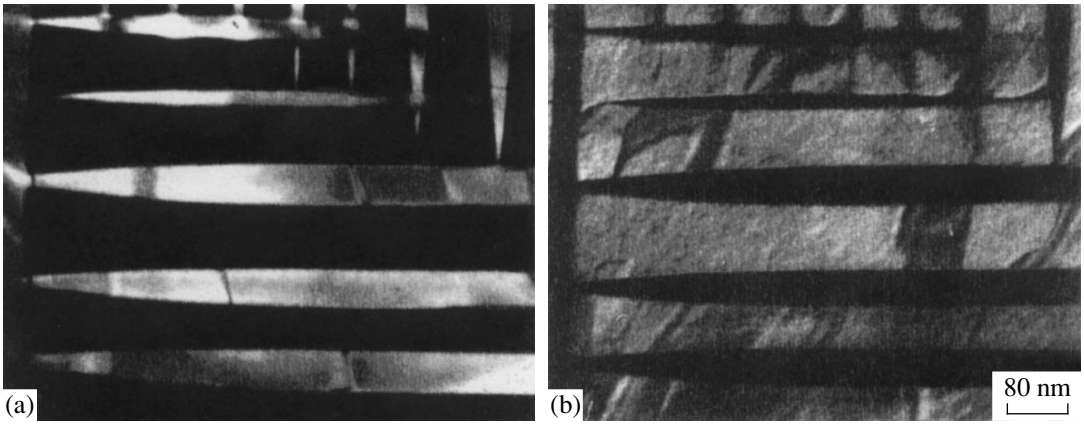

Fig. 1. Typical microstructure of the $L1_0$ phase in CoPt [1], with the (001) direction normal to the plane of the figure and the (110) direction lying horizontally in the plane of the figure. Bright areas in frame (a) or (b) correspond to ordered domains oriented along the (100) or (010) direction, respectively.

with the characteristic length l (which in this problem is the APB width δ) far exceeding the interatomic distance $l_0 = a/\sqrt{2}$. Both theoretical and experimental studies of APBs show that the inequality $l \gg l_0$ is usually fulfilled in alloy systems of practical interest, particularly in systems with an extended interaction range or for small values of order parameters; see, e.g., [8]. The weakly inhomogeneous states can be described within the Ginzburg–Landau approach using the gradient expansion of the free-energy density f.

Let us suppose for simplicity that the concentration c is close to the stoichiometric value $c_s = 0.5$. Then, variations $\delta c = c(\mathbf{r}) - c$ of local concentrations $c(\mathbf{r})$ in the APB region are very small, which is illustrated, for example, by the results of computer simulation [9]. The smallness of δc follows from the symmetry of the free-energy density for the homogeneous $L1_0$ ordering, $f_{0h}(c, \eta_\alpha)$ with respect to the substitution $(c - c_s) \longrightarrow (c_s - c)$, which implies that variations δc are proportional to the small factor $(c - c_s)$. Therefore, in the gradient expansion one can neglect δc and keep only terms with the order-parameter gradients $\nabla\eta_\alpha$ and the elastic strain $u_{\alpha\beta} = (\partial u_\alpha/\partial x_\beta + \partial u_\beta/\partial x_\alpha)/2$. Then the Ginzburg–Landau functional F for the problem takes the form

$$F = \int d^3r \Bigg[f_{0h} + \sum_{\alpha,\beta,\gamma,\delta=1}^{3} \Bigg(g_{\alpha\beta\gamma\delta} \frac{\partial\eta_\alpha}{\partial x_\beta}\frac{\partial\eta_\gamma}{\partial x_\delta} - q_{\alpha\beta\gamma\delta}\eta_\alpha\eta_\beta u_{\gamma\delta} + \frac{1}{2}c_{\alpha\beta\gamma\delta}u_{\alpha\beta}u_{\gamma\delta} \Bigg) \Bigg]. \tag{3}$$

Terms with $q_{\alpha\beta\gamma\delta}$ in Eq. (3) will be called the striction terms, by analogy with the terminology used in the theory of ferroelectricity or magnetism [4]. The microscopic expression for coefficients $q_{\alpha\beta\gamma\delta}$ [9] shows that, in usual approximations neglecting many-atom effective interactions (which are usually small [10]), these coefficients do not depend on the order parameters η_α. Variation of elastic constants $c_{\alpha\beta\gamma\delta}$ with ordering is also usually small, and it will be neglected for simplicity. However, coefficients $g_{\alpha\beta\gamma\delta}$ in Eq. (3) can generally strongly vary with η_α.

Taking into account the crystal symmetry, one can write the integrand in Eq. (3) as

$$f = f_{0h}(\eta_\alpha) + \sum_{\alpha,\beta,\gamma,\delta} g_{\alpha\beta\gamma\delta}\frac{\partial\eta_\alpha}{\partial x_\beta}\frac{\partial\eta_\gamma}{\partial x_\delta} - \sum_\alpha u_{\alpha\alpha}\Bigg(q_{11}\eta_\alpha^2 + q_{12}\sum_{\beta\neq\alpha}\eta_\beta^2\Bigg) + \frac{1}{2}c_{11}\sum_\alpha u_{\alpha\alpha}^2 + c_{12}\sum_{\alpha\neq\beta}u_{\alpha\alpha}u_{\beta\beta} + c_{44}\sum_{\alpha<\beta}u_{\alpha\beta}^2. \tag{4}$$

Here, elastic strains $u_{\alpha\beta}$ are counted from their values in the disordered cubic phase, and the usual Voigt-type notation [4] for coefficients q and c is used.

The equilibrium distribution of strains $u_{\alpha\beta}(\mathbf{r})$ is determined by the equation $\delta F/\delta u_\alpha = 0$:

$$c_{11}\frac{\partial^2 u_\alpha}{\partial x_\alpha^2} + c_{12}\sum_{\beta\neq\alpha}\frac{\partial^2 u_\beta}{\partial x_\alpha x_\beta} + c_{44}\sum_{\beta\neq\alpha}\Bigg(\frac{\partial^2 u_\alpha}{\partial x_\beta^2} + \frac{\partial^2 u_\beta}{\partial x_\alpha x_\beta}\Bigg) = q_{11}\frac{\partial\eta_\alpha^2}{\partial x_\alpha} + q_{12}\sum_{\beta\neq\alpha}\frac{\partial\eta_\beta^2}{\partial x_\alpha}, \tag{5}$$

while the distribution of order parameters $\eta_\alpha(\mathbf{r})$ is determined by the equation $\delta F/\delta\eta_\alpha = 0$, to be discussed below.

Let us first find the spontaneous strain $\bar{u}_{\alpha\beta}$ in the homogeneous (100)-ordered domain with the $|\eta_\alpha| = |\eta_1|$ value equal to the equilibrium order parameter $\eta_e = \eta_e(c, T)$. The nonzero strains $\bar{u}_{11}$ and $\bar{u}_{22} = \bar{u}_{33}$ in this case can be found from the zero-stress condition $\sigma_{\alpha\beta} = \partial f/\partial u_{\alpha\beta} = 0$, which yields:

$$\begin{aligned} \bar{\varepsilon} &= \bar{u}_{11} - (\bar{u}_{22} + \bar{u}_{33})/2 = q_-\eta_e^2/c_-; \\ \bar{u} &= \bar{u}_{11} + \bar{u}_{22} + \bar{u}_{33} = q_+\eta_e^2/c_+, \end{aligned} \tag{6}$$

where $q_- = q_{11} - q_{12}$, $c_- = c_{11} - c_{12}$, $q_+ = q_{11} + 2q_{12}$, and $c_+ = c_{11} + 2c_{12}$.

Analogous expressions for $\bar{u}_{\alpha\beta}$ can be obtained when several nonzero homogeneous η_α are present. After substitution of these $\bar{u}_{\alpha\beta}$ into Eq. (4), the function f can be written as the sum of the renormalized function f_h for the homogeneous ordering, the gradient term, and the elastic energy E_{el}, with the following expressions for f_h and E_{el}:

$$\begin{aligned} f_h(\eta_\alpha) &= f_{0h}(\eta_\alpha) - \frac{q_+^2}{6c_+}\sum_{\alpha,\beta}\eta_\alpha^2\eta_\beta^2 \\ &- \frac{q_-^2}{3c_-}\left(\sum_\alpha \eta_\alpha^4 - \sum_{\alpha<\beta}\eta_\alpha^2\eta_\beta^2\right), \end{aligned} \tag{7}$$

$$\begin{aligned} E_{el} &= \frac{1}{6}c_+(u-\bar{u})^2 + \frac{1}{3}c_-(\varepsilon-\bar{\varepsilon})^2 \\ &+ \frac{1}{4}c_-(\zeta-\bar{\zeta})^2 + c_{44}(u_{12}^2 + u_{23}^2 + u_{31}^2). \end{aligned} \tag{8}$$

Here, $u = u_{11} + u_{22} + u_{33}$, $\varepsilon = u_{11} - (u_{22} + u_{33})/2$, and $\zeta = u_{22} - u_{33}$ while $\bar{u}$, $\bar{\varepsilon}$, and $\bar{\zeta}$ are expressed via η_α as follows:

$$\begin{aligned} \bar{u} &= q_+(\eta_1^2 + \eta_2^2 + \eta_3^2)/c_+, \\ \bar{\varepsilon} &= q_-[\eta_1^2 - (\eta_2^2 + \eta_3^2)/2]/c_-, \\ \bar{\zeta} &= q_-(\eta_2^2 - \eta_3^2)/c_-. \end{aligned} \tag{9}$$

Let us note that the strictive renormalization $f_h - f_{0h}$ in Eq. (7) is proportional to the ordering-induced elastic energy per atom, E_d, which usually is small. For example, for CoPt alloys [1] the tetragonal distortion $\bar{\varepsilon}$ is about 0.03; $\bar{u} \simeq 6 \times 10^{-4}$; and E_d is about 0.01 of the transition temperature T_c.

Let us apply Eq. (5) to the strains $u_{\alpha\beta}(\mathbf{r})$ near a plane flip-APB that is normal to vector $\mathbf{n} = (\sin\theta\cos\varphi, \sin\theta\sin\varphi, \cos\theta)$ and separates the (100)- and (010)-ordered domains. Then the functions u_α and η_α^2 in Eq. (5) depend only on the coordinate $\xi = \mathbf{rn}$ and at $\xi \longrightarrow -\infty$ the nonzero η_α^2 in Eq. (5) is $\eta_1^2 = \eta_e^2$, while at $\xi \longrightarrow \infty$ the nonzero η_α^2 is $\eta_2^2 = \eta_e^2$. The strain $(u_{\alpha\beta} - \bar{u}_{\alpha\beta})$ should vanish at both $\xi \longrightarrow \pm\infty$, otherwise the elastic energy E_{el} in Eq. (8) increases proportionally to the total volume of the ordered domain. Integrating Eq. (5) over ξ from $\xi = -\infty$ to ∞, one finds that the above-mentioned conditions for elastic strains lead to the following equations for angles θ and φ:

$$\begin{aligned} c_{44}\bar{\varepsilon}[\cos^2\theta + \sin^2\theta(\sin^2\varphi - \cos^2\varphi)] &= 0; \\ c_{44}\bar{\varepsilon}[\cos^2\theta + \sin^2\theta(\cos^2\varphi - \sin^2\varphi)] &= 0, \end{aligned} \tag{10}$$

which implies that $\cos\theta = 0$ and $\sin^2\varphi = \cos^2\varphi$. Therefore, an equilibrium flip-APB should have the (110)-type orientation, in accordance with experimental observations and theoretical considerations mentioned above [1–7]. The present Ginzburg–Landau-type approach is just a reformulation of previous theoretical treatments [5–7], but it is also convenient for studies of other properties of polytwinned structures.

Let us now consider the structure of a plane shift-APB in the (100)-ordered twin band with the APB plane normal to vector $\mathbf{m} = (\cos\alpha, \sin\alpha\cos\varphi, \sin\alpha\sin\varphi)$. The elastic equilibrium Eqs. (5) now have a local equilibrium solution $u_{\alpha\beta} = \bar{u}_{\alpha\beta}(\eta_\gamma)$ for any orientation $\mathbf{m}$. Therefore, in finding the order parameters $\eta_\alpha(\mathbf{r})$ (which here depend only on $\xi = \mathbf{rm}$), one can retain only the first two terms on the right-hand sides of Eqs. (3) and (4), with the substitution of f_{0h} by the renormalized function f_h from Eq. (7).

From a consideration of the symmetry, the only nonzero component η_α is $\eta_1 = \eta(\xi)$, which varies, say, from $\eta = -\eta_e$ at $\xi = -\infty$ to $\eta = \eta_e$ at $\xi = \infty$. Let us denote coefficients g_{1111} and $g_{1212} = g_{1313}$ of nonzero gradient terms by g_{11} and g_{12}, respectively. Then functional (3) per unit area normal to the APB plane takes the form:

$$F = \int d\xi[f_h(\eta) + g(\eta)(d\eta/d\xi)^2], \tag{11}$$

where

$$g(\eta) = g_{11}(\eta)\cos^2\alpha + g_{12}(\eta)\sin^2\alpha. \tag{12}$$

The equation $\delta F/\delta\eta = 0$ for functional (11) can be written as

$$2gdy/d\xi + g'y^2 = f_h', \tag{13}$$

where y is $d\eta/d\xi$, and prime means the derivative with respect to η. Writing the derivative $dy/d\xi$ as $ydy/d\eta$ and

integrating Eq. (13) over η from η_e to η, one obtains:

$$y = d\eta/d\xi = [\Delta f_h(\eta)/g(\eta)]^{1/2}. \quad (14)$$

Here, $\Delta f_h(\eta) = f_h(\eta) - f_h(\eta_e)$ and it is taken into account that $y = y(\xi = \infty) = 0$ at $\eta = \eta_e$. Equations (14) and (11) enable one to find both the coordinate dependence $\eta(\xi)$ and the APB surface energy σ:

$$\xi = \int_0^\eta d\eta'[g(\eta')/\Delta f_h(\eta')]^{1/2}, \quad (15)$$

$$\sigma = F\{\eta\} - F\{\eta_e\} = 4\int_0^{\eta_e} d\eta[g(\eta)\Delta f_h(\eta)]^{1/2}. \quad (16)$$

The conventional Landau–Ginzburg theory corresponds to the case of small η when $f_h(\eta)$ is $(-a\eta^2 + b\eta^4)$, η_e^2 is $a/2b$, and g does not depend on η. Then Eqs. (15) and (16) yield the known expressions [11]: $\eta(\xi) = \eta_e\tanh(\xi/\delta)$, $\delta = (g/b\eta_e^2)^{1/2}$, and $\sigma = 8\eta_e^3(gb)^{1/2}/3$. Equations (11)–(16) generalize the conventional Ginzburg–Landau theory to the case of order parameters that are not small, which is most interesting for applications.

Let us now discuss the orientation dependence of APB energies. For an isolated shift-APB, this dependence is determined by the function $g(\eta)$ in Eq. (16), i.e., by the ratio of coefficients g_{12} and g_{11} in Eq. (12). The relation $g_{12} \simeq g_{11}$ corresponds to an approximately isotropic σ, and this case is typical of alloy systems with extended-range interatomic interactions [9]. On the contrary, in the short-range-interaction systems, where the nearest-neighbor interaction V_1 far exceeds the not-nearest-neighbor ones V_n, one has: $g_{12} \ll g_{11}$. It can be illustrated, for example, by the estimates of $g_{1\alpha}$ using the mean-field approximation (MFA), which show that g_{12} is proportional to V_n. The APB energy $\sigma(\alpha)$ for such systems is strongly anisotropic, and its minimum value $\sigma_{\min} \sim (g_{12})^{1/2}$ corresponds to $\alpha = \pi/2$, i.e., to the APB plane parallel to the tetragonal axis, while the APB width δ in this case, according to Eq. (15), is also small: $\delta \sim (g_{12})^{1/2}$. These conclusions qualitatively agree with the results of more precise studies of APBs in the short-range-interaction systems [9], although at small δ under consideration the gradient expansion used above becomes quantitatively inapplicable.

Let us now take into account that the evolution of shift-APBs in polytwinned structures actually occurs within a twin band formed at very first stages of phase transformation. These orientations of APBs tend to minimize their total excess free energy F_e not at a fixed APB area S but at a fixed cross section of the twin hand, S_b. Therefore, the APB energy in this case is more adequately characterized by the quantity $\sigma_b = F_e/S_b$ rather than by $\sigma = F_e/S$ given by Eq. (16). Taking also into account the relation $S_b = (\mathbf{mn}_b)S$, where the vector $\mathbf{n}_b = (1, 1, 0)2^{-1/2}$ describes the orientation of the twin band, one obtains:

$$\sigma_b = \sigma_b(\alpha, \varphi) = \sigma\sqrt{2}/(\cos\alpha + \sin\alpha\cos\varphi), \quad (17)$$

where $\sigma = \sigma(\alpha)$ is given by Eq. (16).

Minimization of Eq. (17) with respect to φ yields $\varphi = 0$; i.e., equilibrium APBs are oriented normally to the (100) plane, while minimization over α gives the equation:

$$\cot\alpha = \left(\int_0^{\eta_e} d\eta g_{12}(\Delta f_h/g)^{1/2}\right)\Big/\left(\int_0^{\eta_e} d\eta g_{11}(\Delta f_h/g)^{1/2}\right). \quad (18)$$

If the dependence of the ratio g_{12}/g_{11} on η is weak, in particular, when g_{12} and g_{11} do not depend on η (as in the case of small η or in the MFA calculations), Eq. (18) is simplified:

$$\cot\alpha = g_{12}/g_{11}. \quad (19)$$

Equations (18) and (19) show that in the isotropic case $g_{12} = g_{11}$ the equilibrium shift-APBs should be normal to twin boundaries, while for the usual relation $g_{12} < g_{11}$ the APB plane should be tilted about the tetragonal axis. This seems to agree with the available experimental data. In particular, the figure shows a distinct tilt of shift-APBs about the tetragonal axes for both (100) and (010) twin bands, while in CuAu alloys (in which interatomic interactions seem to be short-ranged [9] and g_{12}/g_{11} is small) shift-APBs appear to be parallel to the tetragonal axes [12]. Equations (18) and (19) can also be used to estimate the ratio g_{12}/g_{11} from experimental data for the equilibrium tilt angles, which can provide both qualitative and quantitative information about interatomic interactions in an alloy.

I am grateful to I.R. Pankratov, G.D. Samolyuk, and K.D. Belashchenko for assistance. This work was supported by the Russian Foundation for Basic Research, project nos. 00-02-17692 and 00-15-96709.

REFERENCES

1. C. Leroux, A. Loiseau, D. Broddin, and G. van Tendeloo, Philos. Mag. B **64**, 57 (1991).
2. B. Zhang and W. A. Soffa, Phys. Status Solidi A **131**, 707 (1992).
3. C. Yanar, J. M. K. Wiezorek, and W. A. Soffa, in *Phase Transformations and Evolution in Materials*, Ed. by P. E. A. Turchi and A. Gonis (TMS, Warrendale, 2000).

4. F. Jona and G. Shirane, *Ferroelectric Crystals* (Pergamon, Oxford, 1962; Mir, Moscow, 1965), Chap. 4.
5. A. L. Roitburd, Fiz. Tverd. Tela (Leningrad) **10**, 3619 (1968) [Sov. Phys. Solid State **10**, 2870 (1969)].
6. A. G. Khachaturyan and G. A. Shatalov, Zh. Éksp. Teor. Fiz. **56**, 1037 (1969) [Sov. Phys. JETP **29**, 557 (1969)].
7. A. G. Khachaturyan, *Theory of Phase Transformations and Structure of Solid Solutions* (Nauka, Moscow, 1974), Chap. 5.
8. V. Yu. Dobretsov, G. Martin, F. Soisson, and V. G. Vaks, Europhys. Lett. **31**, 417 (1995).
9. K. D. Belashchenko, V. Yu. Dobretsov, G. D. Samolyuk, and V. G. Vaks, in *Phase Transformations and Evolution in Materials*, Ed. by P. E. A. Turchi and A. Gonis (TMS, Warrendale, 2000).
10. A. Zunger, in *Statics and Dynamics of Alloy Phase Transformations*, Ed. by A. Gonis and P. E. A. Turchi (Plenum, New York, 1994), NATO ASI Ser., Ser. B **319** (1994).
11. L. D. Landau and E. M. Lifshitz, *Course of Theoretical Physics*, Vol. 8: *Electrodynamics of Continuous Media* (Nauka, Moscow, 1982; Pergamon, New York, 1984), Parag. 43.
12. M. Guymont and J. Bonneaux, Scr. Metall. **36**, 1175 (1997).

JETP Letters, Vol. 73, No. 5, 2001, pp. 242–245. Translated from Pis'ma v Zhurnal Éksperimental'noĭ i Teoreticheskoĭ Fiziki, Vol. 73, No. 5, 2001, pp. 279–282.

Spiral Vortices in Ferromagnets

A. B. Borisov

Institute of Metal Physics, Ural Division, Russian Academy of Sciences, ul. S. Kovalevskoĭ 18, Yekaterinburg, 620019 Russia

Received July 3, 2000; in final form, January 30, 2001

New types of magnetic defects in two-dimensional ferromagnets are found in the exchange approximation, and the influence of magnetic anisotropy on their structure is analyzed. © *2001 MAIK "Nauka/Interperiodica".*

PACS numbers: 75.70.Kw; 75.30.Gw

It has been established experimentally in the last decade that the distribution of the magnetization vector $\mathbf{M}(\mathbf{r})$ [$\mathbf{M}(\mathbf{r})^2 = M_0^2$] in thin magnetic films with strong perpendicular anisotropy of the easy-axis type can undergo self-organization under certain conditions. Under the action of a harmonic or unipolar pulsed magnetic field, the labyrinth domain structure generates guiding centers (target-type structures, spiral domains, and domain structures with a high degree of translational and orientational ordering [1–5]) which can be observed using the magnetooptic Kerr effect. This phenomenon was interpreted in [1–3] as the transition from the chaotically moving domain boundaries to the dynamic magnetic structures similar to the dissipative structures in distributed active media [6]. Static stability and strong nonlinearity are the distinctive features of these magnetic structures. They do not disappear on switching off the magnetic field because the lifetimes of targets and spiral domains are several orders of magnitude longer than the period of magnetic field. Due to this property, magnetic structures of the target type and spiral domains can be considered as magnetic defects excited by pumping energy into magnetically-ordered media and relaxing to the thermodynamically equilibrium state during a rather long time [4].

Rotary helical waves and guiding centers are studied in detail in the self-oscillatory systems, where they are one of the main types of dissipative structures [7, 8]. For a ferromagnet with uniaxial anisotropy, only small-amplitude nonlinear helical waves have been described to date [3, 9], and it was shown that they can, in principle, be stabilized.

In this work, spiral domains and targets are considered as defects in magnetically ordered media. It is shown that structures of the spiral-vortex type are formed in a 2D ferromagnet even by the main (exchange) interaction. A broad class of new exact solutions of the corresponding equations are found, the structure and interaction of spiral vortices are studied, and the influence of remaining interactions on the structure of a spiral vortex is qualitatively analyzed.

In the continuous approximation, the stationary magnetic structures in a 2D ferromagnet are defined as solutions of the equation

$$\mathbf{M}(\mathbf{r}) \times [\alpha \Delta \mathbf{M}(\mathbf{r}) + \mathbf{H}] = 0, \quad \mathbf{M}^2(\mathbf{r}) = M_0^2, \qquad (1)$$

where α is the exchange interaction constant and the effective magnetic field H is determined by the energy of magnetic anisotropy and the magnetostatic field. In the absence of field H, Eqs. (1) coincide with the n-field ($D = 2$ and $N = 3$) and nematic equations in a single-constant approximation. Although these equations are integrable [10] and the "dressing" procedure is known for them [10–12], the construction of a desired class of solutions by using an analogue of the D'Alembert formula [11] presents serious difficulties.

Below, a broad class of exact solutions is considered, for which the fields $\Phi(x, y)$ and $\theta(x, y)$ parametrizing the magnetization vector $\mathbf{M}(x, y) = M_0\{\sin\Phi\cos\theta, \sin\theta\sin\Phi, \cos\theta\}$ depend on the functionally independent variables $a(x, y)$ and $b(x, y)$ as

$$\theta(x, y) = \theta(a(x, y)), \quad \Phi(x, y) = \Phi(b(x, y)). \qquad (2)$$

It then immediately follows from Eqs. (1) (with $H = 0$) that the fields $\theta(a)$ and $\Phi(b)$ satisfy the simple system of differential equations

$$\theta''(a) = \frac{\sin(2\theta(a))}{2}(\Phi'(b))^2, \quad \Phi''(b) = 0 \qquad (3)$$

provided that additional conditions hold for the fields a and b. These conditions can conveniently be written in the form of equations

$$\begin{aligned} &\partial_z \partial_{\bar{z}} \Omega = \partial_z \Omega \partial_{\bar{z}} \Omega = 0, \\ &z = x + iy = r\exp(i\varphi) \end{aligned} \qquad (4)$$

for the complex function $\Omega = a + ib$. Without loss of generality, one can choose $\Phi(x, y) = b(x, y)$ and take the

solutions for $\theta(a)$ in the form of a soliton lattice (cnoidal wave)

$$\cos\theta = \sigma \mathrm{sn}\left(\frac{a(R,\varphi)}{k}, k\right), \quad R = \ln r \qquad (\sigma = \pm 1, \quad 0 < k < 1). \tag{5}$$

Solutions (4) and (5) generalize the well-known class of Belavin–Polyakov multi-instanton solutions [13]. Indeed, $\cos\theta \longrightarrow \tanh(a)$ at $k \longrightarrow 1$, so that the complex field $\Psi = \cot[\theta/2]\exp[i\Phi] \longrightarrow \exp[i\Omega]$ satisfies, according to Eq. (4), the duality $\partial_{\bar{z}}\Psi = 0$ or antiduality $\partial_z\Psi = 0$ equation.

It follows from the uniqueness of magnetization and symmetry conditions $\mathrm{sn}(u, k) = \mathrm{sn}(u + 4K, k)$ and $\mathrm{sn}(u, k) = \mathrm{sn}(2K - u, k)$ [$K = K(k)$ is the complete elliptic integral of the first kind] that the function Ω must satisfy either of the conditions

$$\oint d\Omega = 4kKN + 2i\pi Q \quad (N, Q \in Z) \tag{6a}$$

or

$$\oint d\Omega = -2\Re(\Omega) + 2kK(2N+1) + i\pi(2Q+1) \qquad (N, Q \in Z), \tag{6b}$$

where integration goes around the center of magnetic defect. In what follows, condition (6a) is only considered. Then the general solution for the system of magnetic defects with centers at points z_j takes for $\Omega = \Omega(z)$ the form

$$\Omega = a + ib = \sum_j^n \left(\frac{2ikK}{\pi}N_j + Q_j\right)\ln(z - z_j) + w(z) \qquad (N_j, Q_j \in Z), \tag{7}$$

where $w(z)$ is an arbitrary meromorphic function. When going along the closed contour around the center of field defect, a and Φ acquire, respectively, the increments $-4kKN$ and $2\pi Q$, thereby ensuring, according to Eq. (5) and the magnetization definition, uniqueness of the $\mathbf{M}(x, y)$ field in the (x, y) plane. Solution (7) is characterized [at $w(z) = \mathrm{const}$] by $4n + 3$ parameters and describes the structure and interaction of magnetic defects. Notice that N may be a halfinteger for the director fields in a nematic. In hydrodynamics, the function Ω of the form (7) at $w(z) = \mathrm{const}$ is the sum of complex potentials of vorticity-source flow.

At $N_j = 0$ ($j = 1, 2, \ldots, n$), solution (5), (7) coincides with the multi-instanton solution (at $k = 1$) or describes a system of interacting magnetic targets (at $k \neq 1$). The isolated magnetic defect with discrete parameters σ, $N \neq 0$, and Q represents a spiral vortex with the normal magnetization component

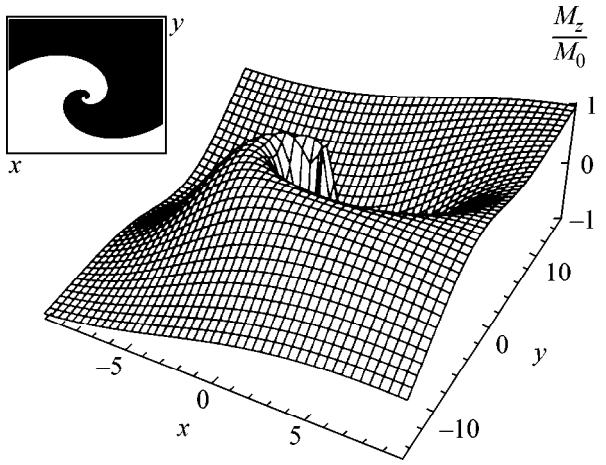

Fig. 1. Core structure of a single-turn spiral ($N = 1$) for $k = 1/2$ and $Q = 1$ ($r_0 = 0$). Inset: domains with positive (white) and negative (black) M_z values. The twisting of the spiral domain increases with a decrease in k.

$$M_z = M_0\sigma\,\mathrm{sn}\left(\frac{Q\ln(r/r_0)}{k} - \frac{2K}{\pi}(\varphi - \varphi_0)N, k\right) \tag{8}$$

and azimuthal angle

$$\Phi = Q(\varphi - \varphi_0) + \frac{2kK(k)}{\pi}N\ln(r/r_0). \tag{9}$$

According to the classification given in [3], solution (8) corresponds to a spiral domain, because it can be obtained in the (R, φ) space from the regular band structure with period $d = 4kK(k)$ by applying the Volterra procedure [14] consisting of the relative shift of cut edges by Nd periods, the 2π rotation, and the free relaxation. The dependence of Eq. (9) on the polar angle φ is typical of the 2D magnetic vortices [15], so that the solutions of the form (8), (9) will hereafter be called spiral vortices. It is notable that the magnetic vortices arise on the nonmagnetic defects and solutions (8), (9) are valid within the distances on the order of the defect radius d.

For $N = 1$, solution (8) represents two oppositely magnetized spiral domains separated by two logarithmic spirals (Fig. 1). For the arbitrary N, Eq. (8) describes an N-turn logarithmic spiral whose chirality (sense of twisting) is determined by the N sign. The graph of the $M_z(x, y)$ field and the configuration of domains in a double-turn spiral are shown in Fig. 2. The width of spiral solitons (domain boundaries) depends on the k value and increases with moving away from the vortex center. At $k \longrightarrow 1$, the width of domain boundaries decreases to zero and the spiral vortex approximates to two domains (with constant magnetizations) with a boundary at $\varphi = \varphi_0$ and $\varphi = \varphi_0 + \pi$.

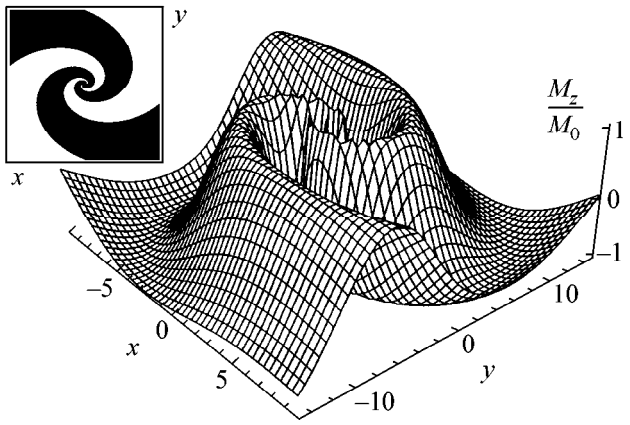

Fig. 2. Structure of a double-turn spiral for $k = 1/4$, $Q = 1$, and $N = 2$.

The energy W of a spiral vortex, as also of the other nonlocal structures of this type (dislocations and disclinations), depends logarithmically on the system size L and the radius d of the vortex core:

$$W = \frac{\alpha}{2}\int\int \nabla\mathbf{M}(\mathbf{r})\nabla\mathbf{M}(\mathbf{r})dxdy$$

$$= \alpha M_0^2\pi\left(\frac{Q^2}{k^2} + \frac{4N^2K^2}{\pi^2}\right)\left[k^2 - 1 + \frac{2E}{K}\right]\ln\left(\frac{L}{d}\right),$$

where E is the complete elliptic integral of the second kind and $N \neq 0$.

In the presence of the field **H**, Eqs. (1) are no longer scale-invariant and the exchange interaction determines the structure of spiral vortex only near its center. The spirals and targets are observed, in particular, in the films with large quality factor, for which the magnetostatic field can be ignored, as compared to the magnetic anisotropy field

$$\mathbf{H} = \beta\mathbf{n}(\mathbf{nM}) \quad \mathbf{n} = (0, 0, 1) \quad (\beta > 0).$$

In this case, the magnetization of a spiral vortex at large distances from its center tends to a homogeneous ground state [$\theta(x, y) \longrightarrow m\pi$, $m \in Z$]. Self-similar solutions (8), (9) are adequate for an isolated spiral vortex only at distances $r < l = \sqrt{\alpha/\beta}$. At larger distances ($r \gg l$), the domain boundary is smeared and one of the spiral domains breaks even in a weak external magnetic field. Numerical studies show [16] that the structure of magnetic target is described by solution (8), (9) for $N = 0$, where the r dependence of $k = k(r)$ should be taken into account. At distances shorter than magnetic length l, the k value remains constant, and it rapidly tends to unity at $r \gg l$. The asymptotic value of m (the number of ring domains reckoned from $r = l$) is uniquely defined by the numerical value $k(r)|_{r \to 0}$. The radius of the end ring increases with decreasing $k(r)|_{r \to 0}$.

As distinct from the multi-instanton solutions, the energy of the multivortex solution (5), (7) depends at $k \neq 1$ on the distances between the centers of spiral vortices, suggesting their interaction. Let us consider some types of vortex dipoles as an example. The interaction between two vortices with parameters (N, Q) and ($-N$, $-Q$) has the attractive character. The corresponding solution is localized: $\theta \longrightarrow \pi/2$ at $r \longrightarrow \infty$ (Fig. 3). The energy of this dipole is independent of the system size L (the energy density is inversely proportional to

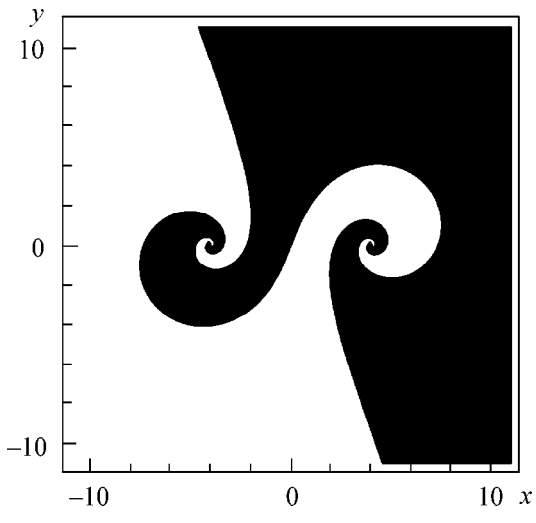

Fig. 3. A spiral dipole composed of two single-turn spirals with centers at $z_1 = 4$ and $z_2 = -4$ and parameters ($N_1 = 1$, $Q_1 = 1$) and ($N_2 = -1$, $Q_2 = -1$), respectively; $k = 3/8$.

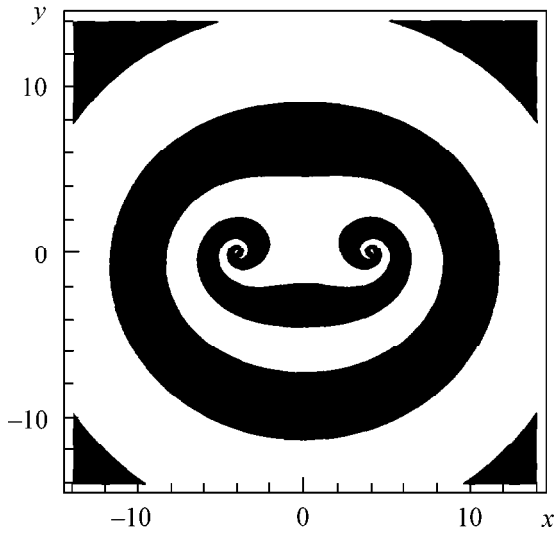

Fig. 4. A spiral dipole composed of two single-turn spirals with centers at $z_1 = 4$ and $z_2 = -4$ and parameters ($N_1 = -1$, $Q_1 = -1$) and ($N_2 = 1$, $Q_2 = -1$), respectively; $k = 1/4$.

r^4). This remarkable feature indicates that the dipoles may contribute to the thermodynamics of two-dimensional magnets. The spiral vortices with parameters (N, Q_1) and ($-N$, Q_2) are also attracted together because the corresponding solution transforms at large distances into a system of concentric (with respect to the R variable) ring domains—magnetic target (Fig. 4) with parameters (0, $Q_1 + Q_2$).

I am grateful to G.S. Kandaurova for clarifying the experimental data and stimulating discussions; to A.B. Shabat, V.G. Marikhin, and A.V. Mikhaĭlov for interest in the work; and to S.A. Zykov for discussions and assistance in computer graphics. This work was supported in part by the Russian Foundation for Basic Research (project no. 00-01-00366) and the INTAS (grant no. 99-1782).

REFERENCES

1. G. S. Kandaurova and A. É. Sviderskiĭ, Pis'ma Zh. Éksp. Teor. Fiz. **47**, 410 (1988) [JETP Lett. **47**, 490 (1988)].
2. G. S. Kandaurova and A. É. Sviderskiĭ, Pis'ma Zh. Tekh. Fiz. **14**, 777 (1988) [Sov. Tech. Phys. Lett. **14**, 346 (1988)].
3. G. S. Kandaurova, Dokl. Akad. Nauk **331**, 428 (1993) [Phys. Dokl. **38**, 342 (1993)].
4. I. E. Dikshteĭn, F. V. Lisovskiĭ, U. G. Mansvetova, *et al.*, Zh. Éksp. Teor. Fiz. **100**, 1606 (1991) [Sov. Phys. JETP **73**, 888 (1991)].
5. F. V. Lisovskiĭ, U. G. Mansvetova, E. P. Nikolaeva, *et al.*, Zh. Éksp. Teor. Fiz. **103**, 213 (1993) [JETP **76**, 116 (1993)].
6. A. Yu. Loskutov and A. S. Mikhaĭlov, *Introduction to Synergetics* (Nauka, Moscow, 1990).
7. M. C. Cross and H. C. Hohenberg, Rev. Mod. Phys. **65**, 851 (1993).
8. L. M. Pismen, *Vortices in Nonlinear Fields* (Clarendon Press, Oxford, 1999).
9. A. B. Borisov, V. A. Feĭgin, and B. N. Filippov, Fiz. Tverd. Tela (Leningrad) **33**, 2316 (1991) [Sov. Phys. Solid State **33**, 1304 (1991)].
10. S. P. Novikov, S. V. Manakov, L. P. Pitaevskiĭ, and V. E. Zakharov, *Theory of Solitons: the Inverse Scattering Method* (Nauka, Moscow, 1980; Consultants Bureau, New York, 1984).
11. I. M. Krichever, Dokl. Akad. Nauk SSSR **253**, 288 (1980).
12. A. B. Borisov and V. V. Kiseliev, Phys. Lett. A **107A**, 161 (1985).
13. A. A. Belavin and A. M. Polyakov, Pis'ma Zh. Éksp. Teor. Fiz. **22**, 503 (1975) [JETP Lett. **22**, 245 (1975)].
14. S. A. Sonin, *Introduction to Physics of Liquid Crystals* (Nauka, Moscow, 1983).
15. A. M. Kosevich, B. A. Ivanov, and A. S. Kovalev, *Nonlinear Magnetization Waves. Dynamic and Topological Solitons* (Naukova Dumka, Kiev, 1983).
16. S. A. Zykov, private communication (2000).

Translated by V. Sakun

JETP Letters, Vol. 73, No. 5, 2001, pp. 246–249. Translated from Pis'ma v Zhurnal Éksperimental'noĭ i Teoreticheskoĭ Fiziki, Vol. 73, No. 5, 2001, pp. 283–286.

Inhomogeneous Hall-Geometry Sample in the Quantum Hall Regime

V. B. Shikin

Institute of Solid-State Physics, Russian Academy of Sciences, Chernogolovka, Moscow region, 142432 Russia

Received November 20, 2000; in final form, February 1, 2001

A generalization of the known theory describing the Hall channels with integer filling factors in inhomogeneous 2D electronic samples to the case of a stationary nonequilibrium state (with a nonzero Hall voltage V_H across the 2D system) is proposed. For the central strip located near the extremum of the electron density, the theory predicts a change in its width and a shift of the whole strip from the equilibrium position as functions of V_H. The theoretical results are used to interpret recent experiments on measuring the local electric fields along the Hall samples both in equilibrium conditions and in the presence of transport in the quantum Hall regime.

PACS number: 73.43.Cd

The phenomenological theory [1–5] of Hall channels with integer filling factors in inhomogeneous 2D electron systems was developed for equilibrium conditions, with the electrochemical potential μ being constant along the sample. However, many experiments with inhomogeneous samples and, in particular, almost all measurements of the local characteristics of various 2D systems [6–10] were performed in a transport regime with a nonzero bias voltage V_H across the sample. In this case, the problem arises as to how the voltage $V_H \neq 0$ affects the characteristics of individual integer (incompressible) channels. To be more specific, one has to consider possible changes in the width $2a$ of the strips and their possible displacement Δ from the equilibrium position under the effect of V_H. Below, this problem is solved for the central incompressible channel in an inhomogeneous 2D electron system with an electron density profile $n(x)$ that is one-dimensional and symmetric about the center of the 2D system. In addition to the one-dimensionality of the problem, we will also use some simplifications (as in [1–5]), namely, we will assume that the transverse dimensions $2w \times 2L$ of the 2D system are sufficiently large (relative to the Bohr radius and the magnetic length), the screening electrodes are absent, the temperature is low but finite (to avoid the correlation effects, which lead to the fractional quantum Hall effect), and the Hall voltage V_H is less than or comparable with the cyclotron energy, $eV \ll \omega_c$ (where ω_c is the cyclotron frequency).

The general results obtained for the quantities $\Delta(V_H)$ and $a(V_H)$ are then used to interpret the experimental data [8–10] on the behavior of the local characteristics of Hall samples with an inhomogeneous profile $n(x)$ of contact origin.

1. We begin by considering the electrochemical potential μ. In nonequilibrium conditions, its value is not constant along the 2D system, and its behavior is determined by the requirements

$$\mathrm{div}\,\mathbf{j} = 0, \quad \mathrm{rot}\,\mathbf{j} = 0, \tag{1}$$

$$j_i = e^{-1}\sigma_{ik}\partial_\mu/\partial x_k, \tag{2}$$

where σ_{ik} is the conductivity tensor [3, Eq. (56); 11], Ohm's law contains the electric potential φ instead of the quantity μ). The combination of requirements (1) and (2) leads to the equation

$$\Delta\mu = 0 \tag{3}$$

even in the case where $\sigma_{xx} \longrightarrow 0$ (note that the authors of [11] do not agree with this statement).

From Eq. (3) and the inequality $w \ll L$, where L is the length of the Hall-geometry sample, it follows that, in the presence of the Hall voltage V_H, the function $\mu(x)$ is a linear function of the x coordinate in the region away from the contacts:

$$\begin{aligned} \mu(x) &= eV_H(x - \Delta + a)/2, \quad \sigma_{xy} \gg \sigma_{xx}, \\ -a + \Delta \le x &\le +a + \Delta, \quad a < w \end{aligned} \tag{4}$$

(the parameter Δ will be determined below (see Eqs. (7) and (14)).

Expression (4) together with the definition of $\mu(x)$ for electrons in the magnetic field form the basis for the formulation of the problem on the properties of incompressible strips in the presence of transport. To solve this problem in a simplified version, it is expedient (by analogy with [1–3]) to begin with modeling within an incompressible strip with the electron density $\delta n(x)$ selected in such a way that its effective value is constant and corresponds to an integer filling factor. Knowing $\delta n(x)$, we reconstruct the distribution $\varphi(x)$ with additional requirements that the tangential electric fields be

zero at the strip boundaries. The function $\varphi(x)$ is fitted in with the behavior of $\mu(x)$ at the same strip ends. The problem with $V_H \neq 0$ allows one to use such an algorithm only for the central strip. As for the side channels, the extension of the approach used in [1–3] to the case with transport encounters some difficulties that require special consideration.

Thus, we assume that

$$\begin{aligned} \delta n(x) &= (\nu_\Delta - l)n_H + n'_\Delta \xi + n''_\Delta \xi^2/2, \\ \xi &= x + \Delta, \quad l = 1, 2, 3, \ldots, \\ \nu(x) &= \pi l_H^2 n(x), \quad n_H = 1/(\pi l_H^2), \\ -a + \Delta &\le x \le +a + \Delta, \end{aligned} \tag{5}$$

where l_H is the magnetic length, Δ is the shift of the central strip as a whole relative to the origin of the coordinates, and $\nu_\Delta \equiv \nu(x = \Delta)$. In the limit $\Delta \longrightarrow 0$, Eq. (5) coincides with $\delta n(x)$ from [3].

The corresponding distribution $E_x(x)$ follows from the Poisson equation represented in the form that takes into account the constancy of the electrochemical potential outside the integer strip:

$$e\delta n(\xi) = -\frac{\kappa}{2\pi^2}\int_{-a}^{+a} ds \frac{E_x(s)}{\xi - s}.$$

As a result, we obtain

$$\begin{aligned} &E_x\sqrt{(1 - \xi^2/a^2)} \\ &= \frac{2\pi e}{\kappa}[(\nu_\Delta - l)n_H T_1(\xi/a) + n'_\Delta a T_2(\xi/a) \\ &\quad + n''_\Delta a^2 (T_3(\xi/a) + T_1(\xi/a))/8] + E_H, \end{aligned} \tag{6}$$

where $T_i(s)$ are the Chebyshev polynomials and E_H is an arbitrary constant; below, this constant will be related to V_H.

For field (6) to become zero at $\xi = \pm a$, the following conditions should be satisfied:

$$2\pi e n'_\Delta a + \kappa E_H = 0, \tag{7}$$

$$a^2 = -4[\nu_\Delta - l]n_H/(n''_\Delta), \quad l = 1, 2, 3, \ldots, \tag{8}$$

where $n(x)$ is the equilibrium electron density profile. The difference between Eq. (8) and the definition of a^2 from [3] is that, in the case under study, the quantity ν_Δ and the derivative n''_Δ are calculated at the point $x = \Delta$ rather than at the zero point.

The potential $\varphi(\xi)$ is obtained from Eq. (6) by a single integration. Taking into account Eqs. (7) and (8), we derive

$$\begin{aligned} \varphi(\xi) &= V_H(\zeta\sqrt{1 - \zeta^2} + \pi/2 + \arcsin\zeta)/\pi \\ &\quad + 2\pi e n''_\Delta a^2 (1 - \zeta^2)^{3/2}/6\kappa, \quad \zeta = \xi/a \end{aligned} \tag{9}$$

with the following requirement being satisfied:

$$-\pi^2 e n'_\Delta a^2/\kappa = V_H. \tag{10}$$

Requirement (10) in combination with Eq. (7) determines the constant $E_H = 2V_H/\pi a$. Equations (7)–(10) terminate the solution of the problem on the behavior of the main channel near the extremum of electron density with an even profile $n(x)$ in the presence of $V_H \neq 0$.

2. Recent experiments carried out for Hall-geometry samples in the quantum Hall regime with the use of scanned potential microscopy [9, 10] testify that the samples have an inhomogeneous but regular distribution of electron density in the form $n(x)$ (where x is the coordinate in the sample cross-section normal to the lines of current). The inhomogeneity of $n(x)$ is caused by the contact phenomena, which are very likely to occur in the experiments under discussion. In this case, for Hall-geometry samples with the dimensions $2w \times 2L$, where $L \gg w$, the distribution $n(x)$ away from the contacts has the form [12]

$$n(x) \simeq n_s + \frac{\kappa W}{ce^2\sqrt{w^2 - x^2}}, \quad c = 2\pi\ln(L/w). \tag{11}$$

Here, W is the contact energy between the 2D system and the metal terminals, and n_s is the mean electron density in the sample without contacts.

Using the explicit expression (11) for $n(x)$, we rewrite some of the definitions given above. The equilibrium distribution $\varphi(x)$ can be represented as

$$\begin{aligned} \varphi(x) &\propto (a^2 - x^2)^{3/2}, \\ a^2 &= \frac{4ce^2w^3[\nu(0) - l]n_H}{\kappa W}, \quad -a \le x \le +a, \\ \nu(0) &= [n(0)]\pi l_H^2. \end{aligned} \tag{12}$$

Here, $2a < 2w$ is the width of the incompressible strip. Its maximal value for the electron density in the form of Eq. (11) is

$$(a_{\max}/w)^3 = 3c\hbar\omega_c/\pi W, \tag{13}$$

where the quantity c is taken from Eqs. (11).

We note that the strip width is highly sensitive to the magnetic field: it varies from zero to the critical size given by Eq. (13) when the magnetic field grows and the maximal value of potential (12) at the channel center reaches the value ω_c; after that, the strip splits in two (the details of this process can be found in [3]).

The definition of Δ is

$$\Delta = -\frac{c}{\pi^2}\frac{eV_H}{W}\frac{w^3}{a^2}. \tag{14}$$

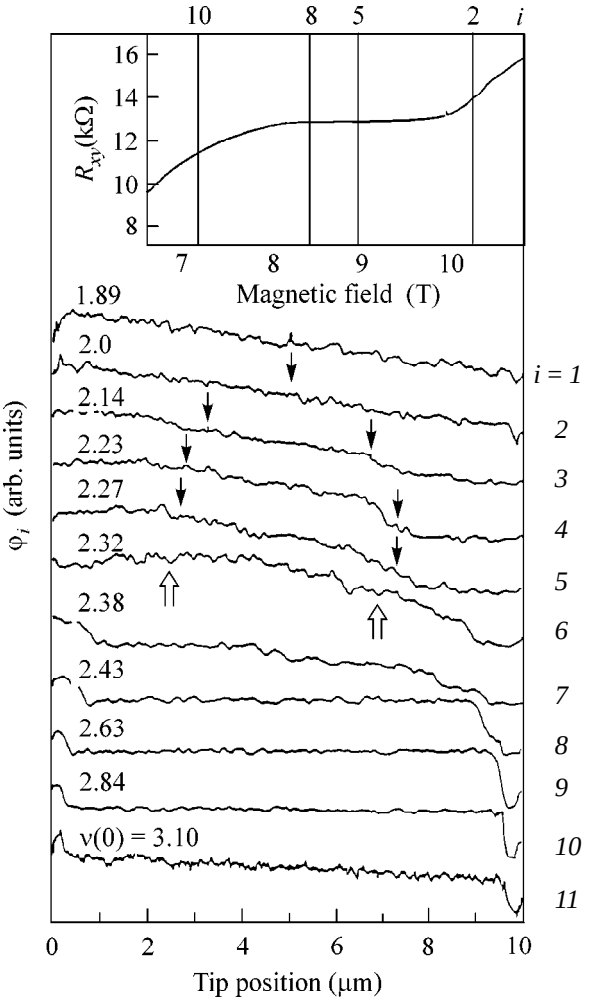

Records [10] of the local electric potential along one of the Hall cross sections in the middle part of the sample for different magnetic fields. The order numbers of the records are shown on the right, and the numbers on the left show the local values of the filling factor ν(0) at the point corresponding to the maximal electron density on the assumption that curve *2* corresponds to the filling factor ν(0) = 2 and the Hall voltage is sufficiently small. The ordinary arrows on curves *2–5* indicate the boundaries of the central incompressible strip in the absence of the transport current according to the calculations by Eq. (12). The double arrows on curve *6* illustrate the asymmetry that arises in the boundary positions under the effect of the transport current. The inset at the top shows the experimental data [10] on the Hall resistance of the sample for magnetic fields in the vicinity of the quantum plateau under consideration. Some of the curves (*1–11*) from the main plot are also shown in the inset, which allows one to make certain inferences about the relationship between the quality of the plateau and the width of the incompressible strips corresponding to these curves.

In addition, we note that the potential

$$\delta\varphi = \varphi(x, V_H) - \varphi(x) \simeq V_H[(x + \Delta) + a]/2, \quad -a + \Delta \le x \le +a + \Delta \tag{15}$$

behaves in a nearly linear way in the cross section of the central strip between the values 0 and V_H.

Turning to the experiments, we discuss the most complete Hall data from [10] (Fig. 2 from the cited paper) for the distribution $\delta\varphi(x)$ over the cross section of a Hall sample with a width of $2w = 10$ μm; the data were obtained in the middle part of the sample in different magnetic fields. The experiment was performed using a scanning microscope, which made it possible to work in the linear region $eV_H \le \omega_c$. However, the tunneling technique proved to be inappropriate for equilibrium measurements (as in [7]). Therefore, the cited paper [10] contains only the difference data for $\delta\varphi(x)$, which correspond to Eq. (15). The experimental dependences are shown in the figure with our own notation. The numbers *1* to *11* on the right indicate the order numbers of the records of $\delta\varphi(x)$ obtained for different values of magnetic field. Some of these numbers are also shown in the inset, which illustrates the behavior of R_{xy} of the given sample in the vicinity of the Hall plateau.

The numbers on the left show the local values of the filling factor ν(0) for each of the given curves (*i*). These values differ from those presented in [10] by a linear shift and are selected to achieve the self-consistency of the contact scenario. In our version of the process, the quasi-symmetric incompressible strip first appears in the vicinity of curve *2* (curve *1* contains no indications of the strip presence, whereas curve *3* already corresponds to a finite width of the strip). Hence, on this curve, the quantity ν(0) must be equal to two, which is taken as the basis for the normalization of the values of ν(0). As the number (*i*) increases, the magnetic field decreases and the width of the central strip increases. Such a behavior of $a(H)$ is possible only when the local density $n(x)$ decreases away from the middle of the sample. In other words, the data on the behavior of $a(H)$ on curves *2–6* testify to the type of the contact interaction that leads to a depletion of the 2D system.

The positions of the boundaries $\pm a(H)$ determined for different magnetic fields by using approximation (12) are shown by arrows on curves *3–6*. The free parameter $W/\hbar\omega_c$ is chosen so that, in conditions *6* corresponding to the splitting of the central strip into two satellites, the value of $a_{\max}$ determined by Eq. (13) is approximately equal to (as one can see from the figure) half the value of *w*. This condition in combination with Eq. (13) yields

$$W/(\hbar\omega_c) = \frac{3c}{\pi}\left(\frac{w}{a_{\max}}\right)^3 = 24c/\pi. \tag{16}$$

The variation of $\delta\varphi(x)$ observed in experiment [10] mainly occurs in the region between the arrows. From expression (15), it follows that this distribution is approximately linear between the strip edges. A small asymmetry is caused by the effect of the Hall voltage on the boundaries of the central incompressible strip. Its estimate is obtained with the use of Eq. (14) for Δ. Taking into account Eq. (16), the characteristic scale of the cyclotron energy on curve *5*, and the experimental

value of $eV_H \simeq 0.01eV \leq \hbar\omega_c^{(5)}$ (see [10]), we obtain for Δ:

$$\Delta_5 \leq 0.1w. \quad (17)$$

The Δ-corrected positions of the boundaries of the central strip are shown by double arrows for curves *5* and *6*.

The current asymmetry is most pronounced on curves *7–11*. Here, the central part is transformed to the "normal" state, i.e., it is equipotential, while the incompressible satellites asymmetrically adjoin the boundaries of the Hall-geometry sample. Unfortunately, the equilibrium language [3] allows no generalization to the case of the side satellites at $V_H \neq 0$. This fact was mentioned above, and, hence, there is no point in discussing the data on the splitting of the central channel (curves *7–11*) in the framework of our study.

Thus, this paper proposes a formalism that generalizes the results reported in [1–3] for integer (incompressible) strips in inhomogeneous 2D systems to the case of a finite Hall voltage $V_H \neq 0$. The theoretical results are used to interpret the experimental data [7, 10] with the help of the hypothesis that the inhomogeneity of the Hall sample is caused by the contact effects. This hypothesis proved to be effective in discussing the equilibrium properties of inhomogeneous Corbino disks with integer strips (see [13, 14]). The appearance of this kind of channels in Hall-geometry samples seems to be quite natural.

Qualitatively, the theoretical picture is fairly close to the experimental observations, which allows an explanation of some specific experimental results. In particular, for the samples studied in the experiments [10], we determined the sign of the contact energy that corresponds to the depletion of the 2D region; we also determined the characteristic scale of the contact energy, which proved to be much greater than the cyclotron energy (see the quantity W in Eq. (16)). An explanation is found for the shift Δ of the central strip due to the voltage $V_H \neq 0$ (Eqs. (14), (17)), as well as for the not yet clearly observable shift of the extremum of $\varphi(x)$ under the effect of $V_H \neq 0$.

I am grateful to Professor V.F. Gantmakher for discussing the results of this study. The work was supported in part by the Russian Foundation for Basic Research, project no. 01-02-16467.

REFERENCES

1. D. Chklovskii, B. Shklovskii, and L. Glazman, Phys. Rev. B **46**, 4026 (1992).
2. D. Chklovskii, B. Shklovskii, and L. Glazman, Phys. Rev. B **46**, 15606 (1992).
3. D. B. Chklovskii, K. F. Matveev, and B. I. Shklovskii, Phys. Rev B **47**, 12605 (1993).
4. D. Chklovskii and P. Lee, Phys. Rev. B **48**, 18060 (1993).
5. M. Fogler and B. Shklovskii, Phys. Rev. B **50**, 1656 (1994).
6. P. F. Fontein, P. Hendriks, F. A. P. Bloom, *et al.*, Surf. Sci. **263**, 91 (1992).
7. R. Knott, W. Dietsche, K. von Klitzing, *et al.*, Semicond. Sci. Technol. **10**, 117 (1995).
8. W. Dietsche, K. von Klitzing, and K. Ploog, Surf. Sci. **361/362**, 289 (1996).
9. K. McCormick, M. Woodside, M. Huang, *et al.*, Phys. Rev. B **59**, 4654 (1999).
10. P. Weitz, E. Ahlswede, J. Weis, *et al.*, Physica E (Amsterdam) **6**, 247 (2000).
11. A. H. MacDonald, T. M. Rice, and W. F. Brinkman, Phys. Rev. B **28**, 3648 (1983).
12. V. Shikin and Yu. Shikina, Fiz. Tverd. Tela (St. Petersburg) **42**, 222 (2000) [Phys. Solid State **42**, 2295 (2000)].
13. V. Shikin, Pis'ma Zh. Éksp. Teor. Fiz. **69**, 64 (1999) [JETP Lett. **69**, 71 (1999)].
14. V. Shikin and Yu. Shikina, Pis'ma Zh. Éksp. Teor. Fiz. **71**, 95 (2000) [JETP Lett. **71**, 65 (2000)].

Translated by E. Golyamina

JETP Letters, Vol. 73, No. 5, 2001, pp. 250–254. From Pis'ma v Zhurnal Éksperimental'noĭ i Teoreticheskoĭ Fiziki, Vol. 73, No. 5, 2001, pp. 287–291.

The Period Map for Pulse Propagation in Nonlinear Optical DM Fibers[1]

A. V. Mikhailov* and V. Yu. Novokshenov**

** University of Leeds, UK and Landau Institute for Theoretical Physics, Russian Academy of Sciences, ul. Kosygina 2, Moscow, 117940 Russia*

*** Institute of Mathematics, Russian Academy of Sciences, Ufa, 450025 Bashkortostan, Russia*

Received February 9, 2001

We have derived a simple recursion formula for the amplitude and chirp of the optical pulse propagating over a Dispersion Managed fiber with zero mean dispersion. We neglect dissipation and assume that the dispersion is constant along the adjacent legs of the waveguide, thus providing the applicability of the integrable nonlinear Schrödinger models within each leg. Choosing the legs long enough to ensure the formation of a self-similar profile, we apply the well-known asymptotic formulas for the nonsoliton initial pulses. Matching them through the interfaces of the legs, we get recursion formulas for the pulse amplitude and chirp. Our analytical results are justified by numerical simulations. © *2001 MAIK "Nauka/Interperiodica".*

PACS numbers: 42.81.Dp

We consider the problem of the propagation of nonlinear electromagnetic pulses in optical fibers with periodically alternating dispersion (so-called Dispersion Managed, or DM, fibers) and absence of dissipation. If the mean dispersion over the period vanishes and the amplitude of the pulse is small, then, according the linear theory, complete compensation of the chromatic spreading would be achieved. In this case, the map over the period of the DM fiber would be an identical transformation and the pulses would completely restore their profiles. However, to provide a low-error transmission and increase the signal-to-noise ratio one should use optical pulses of relatively high amplitude; thus, the nonlinear effects become important and have to be accounted in the theoretical description.

The solution of the above problem is very challenging theoretically and important for many applications including industrial ones (see, for example, [1]). Many interesting results in this direction have already been obtained numerically. Probably, the most advanced analytical results were established on the basis of the Gabitov–Turitsyn approximation [2–4].

Our approach to the problem is entirely different. We use the fact that the corresponding nonlinear Schrödinger equations (NLS) with positive and negative dispersion are completely integrable systems. The integration scheme {the Inverse Scattering Transformation (IST), see [5]}, first developed by V.E. Zakharov and A.B. Shabat in 1971, provides an adequate tool to monitor in details the pulse dynamics. We also assume that the length z_0 of each leg of the fiber is long enough; this enables us to use the asymptotic methods for the solution of the direct and inverse scattering problems (cf. [6]). Our goal is to find an explicit map of the pulse over the period of the DM fiber. Suppose that we have a pulse profile $\hat{u}_n(t)$ at the entrance of the nth leg (for example, with negative dispersion) and we want to find the profile $\hat{u}_{n+1}(t)$ of the pulse at the exit of the consequent leg with positive dispersion. We propose the following scheme:

(a) Using the Lax operator L^- corresponding to the NLS equation with negative dispersion with the potential $u_n^-(t, -z_0/2) = \hat{u}_n(t)$, we solve the direct problem to determine the scattering data.

(b) The scattering data have a simple evolution law; it is thus easy to find the corresponding data at the exit of the nth leg with negative dispersion.

(c) By solving the inverse scattering problem, we find the profile $u_n^-(t, z_0/2)$ at the exit of the nth leg, which serves as initial data for the next leg (with positive dispersion).

(d) Using the Lax operator L^+ corresponding to the NLS equation with positive dispersion with the potential $u_n^+(t, -z_0/2) = u_n^-(t, z_0/2)$, we solve the direct problem to determine the scattering data.

(e) Find the corresponding scattering data at the exit of the leg with positive dispersion.

[1] This article was submitted by the authors in English.

(f) Solve the inverse problem in order to find the emerging pulse $\hat{u}_{n+1}(t) = u_n^+(t, z_0/2)$ after the period of the DM fiber.

We would like to emphasize that all the above-mentioned steps can be explicitly performed and we also can totally control the accuracy of asymptotic solutions to the direct and inverse scattering problems. As the result, we obtain an explicit recurrent relation that enables us to determine the propagation of a pulse over many periods of the DM fiber.

We have compared our analytical solution with the direct computer simulation of the problem and found a good agreement of the results. Moreover, it immediately follows from our solution that the nonlinear contribution to the chirp of the pulse accumulates with distance. This observation is in excellent agreement with numerical simulations as well.

1. Basic facts and notations. The basic model for describing optical fibers is the nonlinear Schrödinger equation, which can be written in the dimensionless form

$$iu_z \pm u_{tt} + 2|u|^2 u = 0, \quad u = u^{\pm}(t, z), \tag{1}$$

after proper rescaling. The plus and minus signs stand for the positive and negative dispersion legs, respectively. The NLS equation is known to be integrable; the corresponding Lax operators

$$L^{\pm} = \begin{pmatrix} \partial_t + \dfrac{i\lambda}{2} & \mp i\bar{u} \\ -iu & \partial_t - \dfrac{i\lambda}{2} \end{pmatrix}, \quad L^{\pm}\Psi = 0, \tag{2}$$

for the spectral transform were found by V.E. Zakharov and A.B. Shabat about thirty years ago. We will consider pulses rapidly decaying as $|t| \longrightarrow \infty$ and assume that the spectral problem (2) does not have discrete eigenvalues. This is the most interesting region of pulse parameters which are commonly used in optical systems of telecommunications [1]. The continuous spectral data yield the standard z-evolution [5]

$$\Psi \longrightarrow \begin{pmatrix} 0 \\ \exp\left(\dfrac{i\lambda t}{2}\right) \end{pmatrix}, \quad t \longrightarrow +\infty,$$

$$\Psi \longrightarrow \begin{pmatrix} b^{\pm}(\lambda) e^{\pm i\lambda^2 z} \exp\left(-\dfrac{i\lambda t}{2}\right) \\ a^{\pm}(\lambda) \exp\left(\dfrac{i\lambda t}{2}\right) \end{pmatrix}, \quad t \longrightarrow -\infty, \tag{3}$$

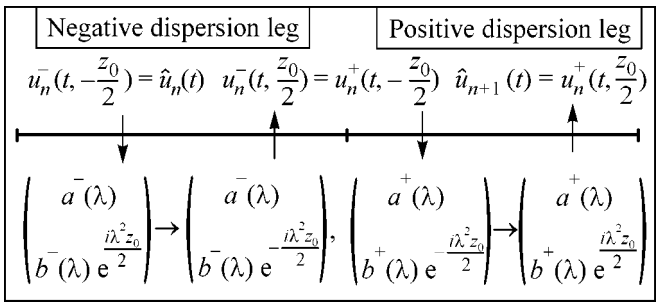

Fig. 1.

and satisfy the unitary condition $|a^{\pm}|^2 \pm |b^{\pm}|^2 = 1$ together with the analysis of the $a^{\pm}$ functions in the upper half-plane $\mathrm{Im}\lambda > 0$.

Here, we will assume that both legs with positive and negative dispersions have equal length z_0 and $\delta = z_0^{-1}$ is a small dimensionless parameter of our theory $\delta \ll 1$. It is convenient to introduce a notation for the small parameter $\varepsilon = z_0^{-1} \ln z_0$.

Suppose that we have a pulse $u(t, 0)$ at the middle of a leg with positive dispersion. We assume that this initial state does not contain solitons. Then at the exit of the leg, i.e., at $z = z_0/2$, it evolves into the following asymptotic form (see [7–10])

$$u\left(t, \frac{z_0}{2}\right) = \delta^{1/2}\left[\alpha(\xi) - \varepsilon\frac{(\alpha^4(\xi))_{\xi\xi}}{4\alpha(\xi)} + O(\delta)\right] \times \exp i\left\{\frac{\xi^2}{2\delta} + \varepsilon\frac{2\alpha^2(\xi)}{2\delta} + O(1)\right\}, \quad \xi = t\delta, \tag{4}$$

where the amplitude $\alpha(\xi)$ can be expressed in terms of scattering data $\alpha^2(\xi) = -\dfrac{1}{\pi}\ln|a^+(\xi)|$ for the corresponding spectral problem.

Solution (4) suggests the following forms for functions $u_n^-(t, -z_0/2)$, $u_n^-(t, z_0/2) = u_n^+(t, -z_0/2)$, and $u_n^+(t, z_0/2)$ (see Fig. 1):

$$u_n^-(t, -z_0/2) = \delta^{1/2}(A_n^-(\xi, \varepsilon) + O(\delta))\exp\left\{\frac{iS_n^-(\xi, \varepsilon)}{2\delta}\right\}, \tag{5}$$

$$u_n^-(t, z_0/2) = u_n^+(t, -z_0/2) = \delta^{1/2}(A_n(\xi, \varepsilon) + O(\delta))\exp\left\{\frac{iS_n(\xi, \varepsilon)}{2\delta}\right\}, \tag{6}$$

$$u_n^+(t, z_0/2) = \delta^{1/2}(A_n^+(\xi, \varepsilon) + O(\delta))\exp\left\{\frac{iS_n^+(\xi, \varepsilon)}{2\delta}\right\}, \tag{7}$$

where

$$S_n^{\pm}(\xi, \varepsilon) = \xi^2 + 2\varepsilon\gamma_n^{\pm}(\xi) + \delta\varphi_n^{\pm} + O(\varepsilon^2),$$

$$S_n(\xi, \varepsilon) = \xi^2 + 2\varepsilon\gamma_n(\xi) + \delta\varphi_n + O(\varepsilon^2).$$

We call functions $\gamma_n(\xi)$ and $\gamma_n^{\pm}(\xi)$ the nonlinear logarithmic phases and $A_n(\xi, \varepsilon)$ and $A_n^{\pm}(\xi, \varepsilon)$ the amplitudes. Representations (5)–(7) can rigorously be justified by the asymptotic solutions of the corresponding inverse scattering problems, provided that the conditions

$$\varepsilon\left|\frac{d^2\gamma_n^{\pm}}{d\xi^2}\right| < 1, \quad \varepsilon\left|\frac{d^2\gamma_n}{d\xi^2}\right| < 1 \tag{8}$$

hold.

We call conditions (8) the small nonlinear chirp conditions. The origin of these conditions is the following. We apply the WKB method to solve the corresponding direct and inverse scattering problems, and conditions (8) guarantee that only one turning point contributes to the result.

2. In items a–f, which correspond to the steps described in Fig. 1, we work with one period of the DM fiber and omit the index n in our notations. We will restore this index in the item devoted to the recursion relation.

a. In order to solve the direct scattering problem corresponding to potential $u_n^-(t, -z_0/2)$, we substitute Eq. (5) in the spectral problem (2), (3) and change the variables. As the result, we get

$$\sqrt{\delta}\psi_1' = -iA^-\exp\left\{\frac{-iS^-(\xi, \varepsilon) + 2i\lambda\xi}{2\delta}\right\}\psi_2,$$

$$\sqrt{\delta}\psi_2' = iA^-\exp\left\{\frac{-iS^-(\xi, \varepsilon) - 2i\lambda\xi}{2\delta}\right\}\psi_1, \tag{9}$$

where $' = d/d\xi$ and $\Psi = (\psi_1 e^{it\lambda/2}, \psi_2 e^{-it\lambda/2})^T$,

$$\begin{pmatrix}\psi_1\\ \psi_2\end{pmatrix}_{t\to+\infty} \longrightarrow \begin{pmatrix}0\\ 1\end{pmatrix};$$

$$\begin{pmatrix}\psi_1\\ \psi_2\end{pmatrix}_{t\to-\infty} \longrightarrow \begin{pmatrix} b^-\left(\lambda, -\frac{z_0}{2}\right)\exp\left\{\frac{i\lambda^2}{2\delta}\right\} \\ 2\delta a^-\left(\lambda, -\frac{z_0}{2}\right)\end{pmatrix}. \tag{10}$$

Following the pioneer work of V.E. Zakharov and S.V. Manakov, we solve system (9) by the WKB method. The stationary (or turning) points are found from the equation $S_+' - 2\lambda = 0$, which reads

$$\xi + \varepsilon\gamma_+'(\xi) - \lambda = 0. \tag{11}$$

Condition (8) guarantees that there is only one turning point

$$a^-\left(\lambda, -\frac{z_0}{2}\right) = \exp\left\{-i\int_{-\infty}^{+\infty}\frac{A_+^2(p, \varepsilon)}{p - \lambda + \varepsilon\gamma_+'(p)}dp\right\}, \quad \mathrm{Im}\lambda > 0, \tag{12}$$

$$b^-\left(\lambda, -\frac{z_0}{2}\right) = \beta^-(\lambda)\exp\left(\frac{-2i\varepsilon A_+^2(\lambda, \varepsilon) - 2i\varepsilon\gamma_+(\lambda)}{2\delta}\right), \quad \mathrm{Im}\lambda = 0, \tag{13}$$

where the function $\beta^-(\lambda)$ can be found explicitly, but we do not use it in the following consideration.

c. Using the asymptotic solution of the inverse scattering problem for operator L^- (following the original method prosed in [6]), we can relate the amplitude $A(\xi, \varepsilon)$ and the logarithmic phase $\gamma(\xi)$ at the exit of the leg with negative dispersion with $A^-(\xi, \varepsilon)$ and $\gamma^-(\xi)$

$$(A^-(\xi, 0))^2 + (A(-\xi, 0))^2 + \gamma^-(\xi) - \gamma(-\xi) = 0, \tag{14}$$

$$\int_{-\infty}^{+\infty}\frac{(A(p, \varepsilon))^2}{p + \lambda + i0 - \varepsilon(\gamma(p))'}dp = \int_{-\infty}^{+\infty}\frac{(A^-(p, \varepsilon))^2}{p - \lambda - i0 + \varepsilon(\gamma^-(p))'}dp, \tag{15}$$

where $\mathrm{Im}\lambda = 0$.

Under the assumption of the *small chirp* (8), it is easy to solve the integral in Eq. (15). Since each functional equation

$$\xi = \mu + \varepsilon(\gamma^-(\mu))', \quad \xi = \nu + \varepsilon(\gamma(-\nu))'$$

has only one root, the real parts of the singular integrals (15) yield

$$(A(\nu, \varepsilon))^2 = \frac{1 - \varepsilon(\gamma(\nu))''}{1 + \varepsilon(\gamma^-(\mu))''}(A^-(\mu, \varepsilon))^2. \tag{16}$$

Equations (14) and (16) can easily be solved in order to express $A(\xi, \varepsilon)$ and $\gamma(\xi)$ in terms of $A^-(\xi, \varepsilon)$ and $\gamma^-(\xi)$.

d–f. Similar to the items a–c, we solve the direct and inverse scattering problems for the operator L^+ in the leg with positive dispersion. This enables us to relate the amplitude $A(\xi, \varepsilon)$ and logarithmic phase $\gamma(\xi)$ given at the entrance of the leg with the exit values $A^+(\xi, \varepsilon)$ and $\gamma^+(\xi)$. The result is very similar to Eqs. (14) and (15):

$$(A^+(\xi, 0))^2 + (A(-\xi, 0))^2 + \gamma(\xi) - \gamma^+(\xi) = 0, \tag{17}$$

$$\int_{-\infty}^{+\infty} \frac{(A^+(p,\varepsilon))^2}{p-\lambda-i0+\varepsilon(\gamma^+(p))'}dp = \int_{-\infty}^{+\infty} \frac{(A(p,\varepsilon))^2}{p+\lambda+i0-\varepsilon(\gamma(p))'}dp, \quad (18)$$

where $\mathrm{Im}\lambda = 0$.

Considering the small-chirp condition (8), Eq. (18) can be easily solved

$$(A^+(\mu,\varepsilon))^2 = \frac{1+\varepsilon(\gamma^+(\mu))''}{1-\varepsilon(\gamma(\nu))''}(A(\nu,\varepsilon))^2, \quad (19)$$

where μ and ν are the unique solutions of the equations

$$\xi = \mu + \varepsilon(\gamma^+(\mu))', \quad \xi = \nu + \varepsilon(\gamma(-\nu))'.$$

3. Collecting the results obtained in the previous items and restoring the index n which enumerates the legs of the DM fiber, we arrive at the recursion relations for the amplitudes and logarithmic phases of the pulse

$$(A_n^-(\xi,0))^2 + (A_n(-\xi,0))^2 + \gamma_n^-(\xi) - \gamma_n(-\xi) = 0,$$

$$(A_n^+(\xi,0))^2 + (A_n(-\xi,0))^2 + \gamma_n(-\xi) - \gamma_n^+(\xi) = 0,$$

$$(A_n^-(\nu_n,\varepsilon))^2 = \frac{1-\varepsilon(\gamma_n^-(\nu_n))''}{1+\varepsilon(\gamma_n(\hat{\mu}_n))''}(A_n(\hat{\mu}_n,\varepsilon))^2,$$

$$(A_n^+(\mu_n,\varepsilon))^2 = \frac{1+\varepsilon(\gamma_n^+(\mu_n))''}{1-\varepsilon(\gamma_n(\hat{\nu}_n))''}(A_n(\hat{\nu}_n,\varepsilon))^2,$$

$$A_{n+1}^-(\xi,\varepsilon) = A_n^+(\xi,\varepsilon),$$

$$\gamma_{n+1}^-(\xi) = \gamma_n^+(\xi).$$

Here, ν_n, $\hat{\mu}_n$, μ_n, and $\hat{\nu}_n$ are the solutions of the following equations:

$$\xi = \hat{\mu}_n + \varepsilon(\gamma_n(\hat{\mu}_n))', \quad \xi = \nu_n + \varepsilon(\gamma_n^-(-\nu_n))',$$

$$\xi = \mu_n + \varepsilon(\gamma_n^+(\mu_n))', \quad \xi = \hat{\nu}_n + \varepsilon(\gamma_n(-\hat{\nu}_n))'.$$

These solutions are unique, provided the small-chirp conditions (8) hold.

It follows from the above recursion relation that the small-chirp condition is not uniformly valid and will break at some distance, even if it satisfies the input pulse. Indeed, suppose that the initial profile is of form (4)

$$\gamma_1^-(\xi) = \alpha^2(\xi), \quad A_1^-(\xi,\varepsilon) = \alpha(\xi) - \varepsilon\frac{(\alpha^4(\xi))_{\xi\xi}}{4\alpha(\xi)}$$

and satisfies condition (8). It follows from the above recursion relations that after n periods of propagation we obtain

$$\gamma_{n+1}(\xi) = (2n+1)\alpha^2(\xi),$$

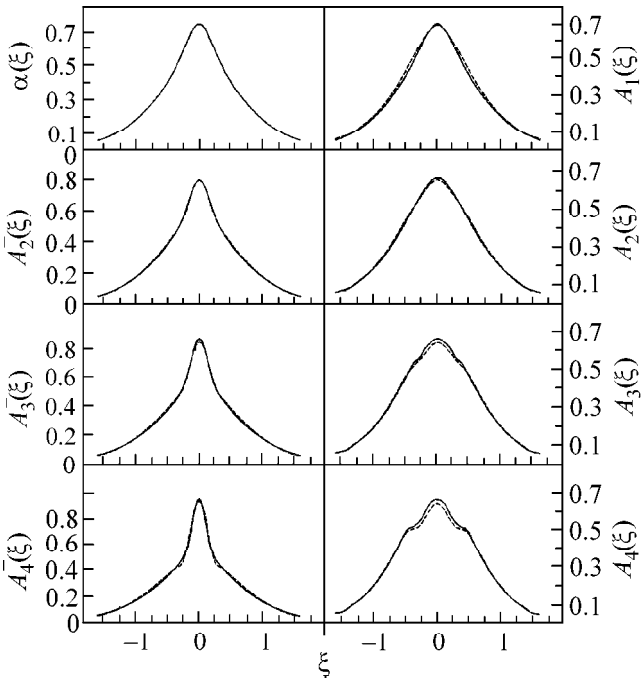

Fig. 2. The subsequent pulse amplitude profiles. The solid line corresponds to numeric simulation; dashed line, to asymptotic expansions by the recurrence formulas.

$$A_{n+1}(\xi,\varepsilon) = \alpha(\xi) - \varepsilon\frac{(2n+1)(\alpha^4(\xi))_{\xi\xi}}{4\alpha(\xi)} + O(\varepsilon^2),$$

$$\gamma_{n+1}^+(\xi) = (2n+3)\alpha^2(\xi),$$

$$A_{n+1}^+(\xi,\varepsilon) = \alpha(\xi) + \varepsilon\frac{(2n+3)(\alpha^4(\xi))_{\xi\xi}}{4\alpha(\xi)} + O(\varepsilon^2).$$

It is clear that for $n \sim \max((\gamma^-(\xi))'')\varepsilon^{-1}$, condition (8) fails and we have to take into account other turning points in the WKB analysis, which is beyond the scope of this paper. According to our theory, the nonlinear contribution to the chirp ($\gamma''(\xi)$) increases as the pulse propagates along the DM fiber.

4. Direct numerical simulations of the NLS equation with alternating dispersion are in good agreement with our analytical results. The standard split-step pseudospectral scheme was used for the numerical solution of the problem. The initial condition was taken in the form

$$u(t,0) = 0.42\exp\left(-\frac{t^2}{16} + \frac{it}{4}\right). \quad (20)$$

By the numerical solution of the direct scattering problem, we have checked that the spectral problem with potential (20) does not have discrete eigenvalues. The

length of each leg was taken to be large enough, $z_0 = 400$, so that

$$\delta = \frac{1}{400} = 0.0025, \quad \varepsilon = \frac{\ln 400}{400} \approx 0.015.$$

We compared the numerical profiles of the pulse at the interface points with the analytical expressions obtained via the recurrence relations. The results are shown in Fig. 2. The increase in the nonlinear contribution to the chirp obtained analytically is in a perfect agreement with our numerical simulations.

5. Conclusion. The study of the DM maps is a new approach to the problem of description of pulse propagation in optical fibers with dispersion management. Our paper is the first and quite modest step in this direction, but we believe that it can be useful for further understanding and even description of the optical pulse evolution over a number of initial DM periods of its propagation in DM systems. It is very important that we can rigorously control the accuracy (more precisely, the residue terms) in our asymptotic formulas. Small nonlinear chirp condition (8) poses natural limitations on the applicability of our theory. We are still unable to analytically control the formation of true DM solitons. There are significant difficulties in the application of the WKB asymptotic technique while dealing with multiple stationary points, which contribute to the solutions of the corresponding direct and inverse scattering problems. Work in this direction is currently in progress. We hope to overcome this drawback and obtain a functional discrete dynamical system for the corresponding amplitudes and phases, which would have the DM soliton as its attractor. This would also open the perspective to solve the challenging problem of description of the DM-soliton interaction.

Another promising direction of the development is the study of systems with amplifiers and filters at the junction points of the legs with different dispersion. It is easy to control the pulse dynamics through multiplying the transmission coefficient $a(\lambda)$ by a fixed constant (the amplification factor), or even by a function (filtering). One can also make obvious modifications of the above theory to describe DM systems with a near-constant profile of dispersion.

We thank participants of the seminar at the Landau Institute for useful and critical discussion. This work was supported in part by the Russian Foundation for Basic Research (project no. 99-01-00431) and the INTAS (grant no. 99-1782). V.Yu.N acknowledges the support of the Leeds University (Dept. Appl. Math.). We are grateful to the Royal Society for the support of the joint project with the Landau Institute for Theoretical Physics.

REFERENCES

1. *Optical Solitons. Theoretical Challenges and Industrial Perspectives*, Ed. by V. E. Zakharov and S. Wabnitz (Springer, 1999), EDP Sciences.
2. I. Gabitov and S. Turitsin, Opt. Lett. **21**, 327 (1996).
3. V. E. Zakharov and S. V. Manakov, Pis'ma Zh. Éksp. Teor. Fiz. **70**, 573 (1999) [JETP Lett. **70**, 578 (1999)].
4. S. Turitsin and V. Mezentsev, Pis'ma Zh. Éksp. Teor. Fiz. **67**, 616 (1998) [JETP Lett. **67**, 640 (1998)].
5. *Theory of Solitons*, Ed. by S. P. Novikov (Nauka, Moscow, 1980).
6. V. E. Zakharov and S. V. Manakov, Zh. Éksp. Teor. Fiz. **71**, 203 (1976) [Sov. Phys. JETP **44**, 106 (1976)].
7. A. Hasegava, *Solitons in Optics* (Academic, New York, 1995).
8. V. Yu. Novokshenov, Dokl. Akad. Nauk SSSR **251**, 799 (1980).
9. A. R. Its, A. G. Izergin, V. E. Korepin, and G. G. Varzugin, Physica D (Amsterdam) **54**, 351 (1992).
10. P. A. Deift and X. Zhou, Commun. Math. Phys. **165**, 175 (1994).

JETP Letters, Vol. 73, No. 5, 2001, pp. 255–261. Translated from Pis'ma v Zhurnal Éksperimental'noĭ i Teoreticheskoĭ Fiziki, Vol. 73, No. 5, 2001, pp. 292–299.

Strong Correlations in a Model of a Gauged (2 + 1)-Dimensional Nonlinear Schrödinger Equation

A. P. Protogenov

Institute of Applied Physics, Russian Academy of Sciences, ul. Ul'yanova 46, Nizhni Novgorod, 603155 Russia
e-mail: alprot@appl.sci-nnov.ru

Received January 3, 2001

Phenomena caused by strong correlations between nonlinear modes in planar systems are briefly reviewed. The analysis is restricted to the model of a nonlinear Schrödinger equation. Stationary field distributions are found. The number of particles is obtained as a function of a parameter characterizing the degree of linking of the world lines of excitations. It is shown that, for small values of this parameter, a two-dimensional lattice is characterized by universal attraction, which can be a dynamical cause for the transition to the coherent state. The relation between the chiral nonlinear edge modes and breaking of the Galilei invariance in the system under consideration is discussed. © *2001 MAIK "Nauka/Interperiodica"*.

PACS numbers: 71.10.Pm; 11.10.Lm

Strong electron correlations in spatially two-dimensional systems are extensively studied nowadays. In [1–4], the correlation effects were examined in the model described by the gauged nonlinear Schrödinger equation (NSE). This equation was applied to various problems [5–8]. Two basic reasons for applying NSE to the examination of strong correlations in (2 + 1)-dimensional systems are noteworthy. The first methodological reason is that the equations of motion in the case of stationary states coincide with the equations derived by varying the Ginzburg–Landau functional supplemented by the Chern–Simons term. This approach was extensively used [9, 10] for analyzing quantum states in a strongly correlated medium such as an incompressible Fermi liquid in the fractional quantum Hall effect.

The second reason is that we are interested in the effect of the short-wave quantum dynamics of particles on the behavior of observables in the infrared limit. Because the phase of the complex order parameter is sensitive to long distances, an analysis of the dynamics of this phase in the long-wave limit provides additional information about the origin of small-scale strongly correlated states. This is facilitated by the fact that the dynamics of the Chern–Simons gauge fields, which reflects the specific character of (2 + 1)-dimensional systems, makes a considerable contribution to the phase of the order parameter. Nonlocal statistical Chern–Simons interaction in the (2 + 1)D Fermi system in the long-wave description encodes the quantum-group structure of quantum states. Along with the large value of the coupling constant, it presents the basic content of what we mean when talking about strong correlations.

The correlation contribution from the Chern–Simons gauge field to the spatial structure of the order parameter is greatest in the static case [11]. Indeed, let us consider a (2 + 1)D system with the Lagrangian density

$$\mathcal{L} = \frac{k}{2}\varepsilon^{\alpha\beta\gamma}A_\alpha\partial_\beta A_\gamma + i\Psi^*(\partial_t + iA_0)\Psi - \frac{1}{2}|\mathbf{D}\Psi|^2 + \frac{g}{2}|\Psi|^4. \quad (1)$$

It gives the equations of motion

$$i\partial_t\Psi = -\frac{1}{2}\mathbf{D}^2\Psi + A_0\Psi - g|\Psi|^2\Psi, \quad (2)$$

$$[\nabla\times\mathbf{A}]_\perp = -\frac{1}{k}|\Psi|^2, \quad (3)$$

$$\partial_t A_i + \partial_i A_0 = -\frac{1}{k}\varepsilon_{ij}j_j, \quad (4)$$

where k is the Chern–Simons coefficient, g is the coupling constant, $\mathbf{j} = \Im(\Psi^*\mathbf{D}\Psi)$ is the current density, and $\mathbf{D} = \nabla - i\mathbf{A}$. From these equations, the gauge potential A_μ, which is an auxiliary variable, can be expressed in terms of the function Ψ as

$$\mathbf{A}(\mathbf{r}, t) = \frac{1}{k}\int d^2\mathbf{r}'\mathbf{G}(\mathbf{r}-\mathbf{r}')|\Psi(\mathbf{r}', t)|^2, \quad (5)$$

$$A_0(\mathbf{r}, t) = \frac{1}{k}\int d^2\mathbf{r}'\mathbf{G}(\mathbf{r}-\mathbf{r}')\mathbf{j}(\mathbf{r}', t), \quad (6)$$

where the Green's function satisfying the equation

$$\nabla\times\mathbf{G}(\mathbf{r}) = -\delta^2(\mathbf{r}) \quad (7)$$

has the form

$$G_i(\mathbf{r}) = \frac{1}{2\pi}\frac{\varepsilon_{ij}x_j}{r^2}. \quad (8)$$

It is seen from Eqs. (5) and (6) that, to pass to the classical NSE, where the contributions from the gauge fields are neglected, it is necessary to use the limit $k \longrightarrow \infty$.

The Chern–Simons coefficient k has a meaning of the number of links of the world lines of excitations. Its fermion value $k = 1$ [12] corresponds to the unlinked world lines. The case where the parameter k is a matrix is more informative. For some systems [13], it coincides with the matrix of Haldane's statistical interaction [14] in his formulation of the generalized state exclusion principle. For simplicity, it will be assumed in this study that the coefficient k is a number.

The system under consideration possesses a rich variety of symmetry transformations and the corresponding constants of motion [15, 16]. In particular, the number of particles and the Hamiltonian are

$$N = \int d^2\mathbf{r}|\Psi|^2 \quad (9)$$

and

$$H = \frac{1}{2}\int d^2\mathbf{r}(|\mathbf{D}\Psi|^2 - g|\Psi|^4), \quad (10)$$

respectively. For convenience, the sign of the coupling constant g in Eq. (10) corresponds to attraction, i.e., to a negative scattering length in the s-wave channel. Below, the following conserved generator of conformal transformations is used:

$$K = -t^2H + 2tD + \frac{1}{2}\int d^2\mathbf{r}r^2|\Psi|^2, \quad (11)$$

which is expressed through the Hamiltonian H, the conserved generator D of time scale transformations, and the average value of the Ψ-field distribution width squared. For static distributions, the width of the field distribution is independent of time. Because the quantity K is conserved, it follows from Eq. (11) that both D and H are equal to zero for static fields.

By using the identity [11, 15]

$$\begin{aligned}|\mathbf{D}\Psi|^2 &= |(D_x - iD_y)\Psi|^2 \\ &- [\nabla\times\mathbf{A}]_\perp|\Psi|^2 - [\nabla\times\mathbf{j}]_\perp,\end{aligned} \quad (12)$$

the Hamiltonian is represented in the form

$$H = \frac{1}{2}\int d^2\mathbf{r}\left(|(D_x - iD_y)\Psi|^2 - \left(g - \frac{1}{|k|}\right)|\Psi|^4\right), \quad (13)$$

which indicates that the greatest changes in the effective coupling constant $g_{\text{eff}} = g - 1/|k|$ occur at $|k| = 1/g$. In this case, the nonlinear term $|\Psi|^4$ in Eq. (13) cancels out and this effect clearly demonstrates the role of the Chern–Simons correlations. In this case, the Hamiltonian is equal to zero on the Ψ-field distributions satisfying the equations

$$(D_x - iD_y)\Psi = 0. \quad (14)$$

The gauge potential $\mathbf{A}(\mathbf{r})$ in Eqs. (14) obeys Gauss' law (3).

The substitution $\Psi(\mathbf{r}) = \rho(r)e^{i\alpha(r,\vartheta)}$, $A_x = \partial_y\rho + \partial_x\alpha$, and $A_y = -\partial_x\rho + \partial_y\alpha$ transforms the self-duality equations (14) and Eq. (3) into the Liouville equation

$$\nabla^2\ln\rho = -\frac{1}{k}\rho^2, \quad (15)$$

which has the exact n-soliton solution [11, 15, 17]

$$\Psi_n(r,\vartheta) = \frac{2\sqrt{k}}{r}n\left(\left(\frac{r_0}{r}\right)^n + \left(\frac{r}{r_0}\right)^n\right)^{-1}e^{i(1-n)\vartheta}, \quad (16)$$

where r_0 is the scale and $n = 1, 2, \ldots$. The number of particles N for this solution is $4\pi nk$.

Stationary States

1. Equations of motion. Solutions of duality equations (14) are first-order equations and only a part of the set of solutions of the equations of motion. Now we are interested in the correlation contribution to the observables from those solutions of the equations of motion which do not coincide with the solutions of the duality equations. In order to determine this contribution, we consider stationary states.[1] In this case, the spatial distributions of the field $\Psi(\mathbf{r}, t)$ acquire mass and become narrower because the asymptotic behavior at far distances changes from power law [as in Eq. (16)] to exponential. For this reason, it should be expected that contribution of the gauge fields to the correlation effects increases in magnitude.

Let us assume that

$$\Psi(\mathbf{r}, t) = |k|^{3/2}\rho(x, y)e^{i\mu t + i\alpha(x,y,t)},$$

where $\alpha(x, y, t)$ is an arbitrary function and μ is the constant chemical potential. To compensate ambiguity in the choice of the phase $\alpha(x, y, t)$ of the field $\Psi(x, y, t)$, we represent the solutions for the gauge potential components in the form [19]

$$\begin{aligned}A_0 = -\frac{k^2}{2}w + \partial_t\alpha, \quad A_x = -ku + \partial_x\alpha, \\ A_y = -kv + \partial_y\alpha\end{aligned} \quad (17)$$

and perform the scale transformation of the coordinates:

$$t \longrightarrow \left(\frac{2}{k|k|}\right)t, \quad x \longrightarrow \frac{x}{|k|}, \quad y \longrightarrow \frac{y}{|k|}. \quad (18)$$

[1] Recall [18] that the equations for the stationary field distributions in systems with the constant number of particles coincide with the equations describing the static field configurations in the systems with varying number of particles.

Then, equations of motion (2)–(4) can be expressed in terms of the functions $\rho \equiv \rho(x, y)$, $w \equiv w(x, y, t)$, $u \equiv u(x, y, t)$, and $v \equiv v(x, y, t)$ of the new variables x, y, and t as

$$\rho_{xx} + \rho_{yy} - \mu\rho = -2C\rho^3 + \rho(u^2 + v^2 - w), \quad (19)$$

where $C = g|k|$,

$$u_y - v_x = -\rho^2, \quad (20)$$

$$u_t - w_x = -2v\rho^2, \quad (21)$$

$$v_t - w_y = 2u\rho^2. \quad (22)$$

Gauss (20) and Hall (21), (22) laws immediately result in the conservation law for the number of particles

$$\rho_t^2 = 2((u\rho^2)_x + (v\rho^2)_y). \quad (23)$$

For $C = 1$ in the static limit and with $u = (\ln\rho)_y + \partial_x\alpha$, $v = -(\ln\rho)_x + \partial_y\alpha$, and $w = -\rho^2$, these equations coincide with the Liouville equation (14). Taking into account that the field amplitude ρ, the characteristic scale L of the field, and the constant C obey the relations

$$\rho_{\mu\neq 1}^2 = \sqrt{\mu}\rho_{\mu=1}^2, \quad L_{\mu\neq 1} = \frac{1}{\sqrt{\mu}}L_{\mu=1}, \quad C_{\mu\neq 1} = \sqrt{\mu}C_{\mu=1}, \quad (24)$$

one can set $\mu = 1$ in Eq. (19) without loss of generality.

It follows[2] from Eq. (11) that $\partial^2/\partial t^2 \int d^2\mathbf{r}\, r^2|\Psi|^2 = 4H$. Therefore, if the effective width of the field Ψ increases with time according to a parabolic law for $H > 0$, the field width is zero at a certain time for $H < 0$. This phenomenon indicates that the field distribution in the system may collapse, which was studied in this context in [21]. It was found that the nonstationary states in the automodeling variables satisfy the equations coinciding in form with Eq. (19). Nonintegrability of this equation in the general case was tested in [19] by the adapted Painlevé test [22] with separating solution singularities belonging to two-dimensional nonstationary manifolds.

As is seen, the value $H = 0$ is a boundary separating two different time regimes of field behavior. Below, we will be interested in those field configurations $\rho(x, y)$ for which the Hamiltonian is equal to zero and in their contribution to Eq. (9) for the number of particles. After the substitution of the solutions of Eqs. (19)–(22) into Eq. (9), the result will depend on the only parameter C of the problem, and the magnitude of this contribution will determine the relative role of different sectors of the theory, which correspond to different values of the coefficient k.

The methods and results of numerical integration of the set of equations (19)–(22) and the configurations of the fields ρ, u, and w are presented in [1, 2]. The line a in the figure is the critical number of particles N_{cr} calculated as a function of the parameter C for the states with $H = 0$ using the found field distributions $\rho(x, y)$.

Let us comment on the dependence $N_{cr}(C)$ and the origin of its divergence. Because the second term $\rho(u^2 + v^2 - w)$ on the right-hand side of Eq. (19) is positive[3] and, therefore, describes the correlation repulsion, it effectively reduces the coupling constant g entering into the first term in this equation and into the second term in the Hamiltonian. For this reason, the reconstruction of the zero value of Hamiltonian (10) requires larger Ψ-field values, as compared to the case $k \longrightarrow \infty$. This leads to an increase in the critical number of particles $N_{cr}(C)$ compared to the value $N_{cr}(\infty) = 11.703$. The position of the line $N_{cr}(C)$ over the asymptotic line $N_{cr}(\infty)$ testifies to the existence of the repulsion due to the correlation interaction between field configurations in the model.

Another feature is that with a decrease in the parameter $C = g|k|$, the function $N_{cr}(C)$ increases until it diverges at $C_{cr} = 2.83$. This phenomenon is caused by the fact that the relative contribution from the term $\rho(u^2 + v^2 - w)$ to the solutions increases with decreasing C and the contributions from the first and second terms in Eq. (19) to the solution become equal to each other at $C = C_{cr}$. At this point, a change in the sign of the right-hand side of Eq. (19) and the sign of the chemical potential is accompanied by changing the spectral properties of the operators of the problem, resulting in the divergence of the function $N_{cr}(C)$ at $C = C_{cr}$.

The effect of the divergence of the function $N_{cr}(C)$ upon strong renormalization of the bare interaction represented by the first term on the right-hand side of Eq. (19) arises due to the exaggerated contribution from the large-amplitude gauge fields, because it is proportional to the unrestricted function $u^2 + v^2 - w$. This expression is valid, strictly speaking, in the long-wave limit when the gauge fields are small. To correctly take into account the contribution from gauge fields arbitrarily large in amplitude and to solve the problem of existence for the function $N_{cr}(C)$ at small values of parameter C, it is necessary to formulate the lattice analogue of the model described by Eqs. (19)–(22). The lattice compactification of the model restricts the contribution of the gauge field in the absolute value but retains arbitrarily large values of the gauge fields.

2. Discrete dynamics. Lattice gauge theory implies the use of the derivatives

$$\nabla_k^+\rho(\mathbf{r}) \equiv e^{iA_k(\mathbf{r})}\rho(\mathbf{r} + \mathbf{e}_k) - \rho(\mathbf{r}), \quad (25)$$

$$\nabla_k^-\rho(\mathbf{r}) \equiv \rho(\mathbf{r}) - e^{-iA_k(\mathbf{r})}\rho(\mathbf{r} - \mathbf{e}_k) \quad (26)$$

[2] This statement is referred to in the literature as Talanov theorem [20].

[3] This term scales as l^5 and [after replacing $\rho \longrightarrow l\rho$, the first term on the right-hand side of Eq. (19) is proportional to l^3] describes the renormalization of the chemical potential μ.

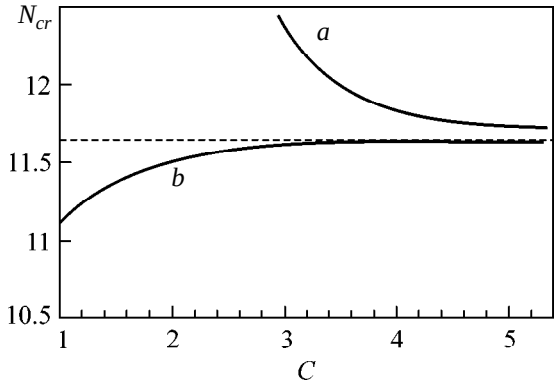

Critical number of particles vs. the parameter $C = g|k|$ for line *a* continuous, Eq. (19), and line *b* lattice, Eq. (29), gauged NSE models. The dashed straight line is the $N_{cr} = 11.605$ value obtained for the critical number of particles on a lattice by neglecting the Chern–Simons correlations.

and the Laplacian

$$\Delta(A) \equiv \nabla_k^+ \nabla_k^- = \hat{t}_x + \hat{t}_y + \text{h.c.} - 4. \tag{27}$$

Here, the subscript k indicates the direction of the unit vector $\mathbf{e}_k$ in the lattice; $\hat{t}_x \equiv e^{\frac{\partial}{\partial m} + iA_{\hat{m},n}}$ is the operator of magnetic translations; and the notation $A_{\hat{m},n}$ means that the gauge-potential component $A_x(m, n)$ defined on a link with the coordinates of the ends (m, n) and $(m + 1, n)$ depends on the coordinates $(m, n) \in \mathbb{Z}^2$ of a lattice site. According to the rules of lattice gauge theory, the density of the particle number $\rho^2_{m,n}$ is defined at the sites of the dual lattice.

The reason that forced us to formulate the theory on a spatial lattice due to the intense vector potential also dictates the necessity for the introduction of a discrete time. With allowance made for the gauge invariance, the following replacement in the equation of motion (2) for the stationary states $\Psi = \rho_{m,n} e^{it}$

$$\left(i\frac{\partial}{\partial t} - A_0\right)\Psi \longrightarrow \frac{i}{2}\left(e^{\frac{\partial}{\partial t} + iA_0} - e^{-\frac{\partial}{\partial t} - iA_0}\right)\Psi = -\Psi \sin(A_0 + 1) \tag{28}$$

satisfies the above-listed requirements to the theory. It is seen that the transition to the uniform representation e^{iA_μ} of the contribution from all components of gauge connectednesses A_μ, i.e., the use of both Wilson e^{iA_k} and Polyakov e^{iA_0} exponentials, together with the requirement of the gauge invariance, forces us to treat the time t as a discrete variable. When considering a hyperbolic operator in the sine-Gordon equation, Faddeev [23] stated that the motion in the spatial lattice needs the discrete evolution. Since A_0 plays the role of the chemical potential, the representation e^{iA_0} for its contribution physically means that the system energy cannot change by an arbitrarily large value when the system is added by one particle with energy A_0.

By using Eqs. (27) and (28), the equation of motion in the model described by the discrete gauged NSE takes the following form for stationary states:

$$\left(e^{\frac{\partial}{\partial m} + iA_{\hat{m},n}} + e^{\frac{\partial}{\partial n} + iA_{m,\hat{n}}} + \text{h.c.} - 4\right)\rho_{m,n} = -2C\rho^3_{m,n} + \rho_{m,n}\sin(w_{m,n} - 1). \tag{29}$$

In contrast to the Hofstadter problem of the states and spectrum of a particle on a lattice in an external magnetic field [24], the vector-potential components $A_k(m, n) = (A_{\hat{m},n}, A_{m,\hat{n}})$ entering into the Laplacian in this equation are determined by the function on which the Laplacian acts:

$$A_{\hat{m},n} = \sum_{m',n'} \nabla_2 G(m - m', n - n')\rho^2_{m',n'}. \tag{30}$$

The scalar potential for the lattice analogue of Eqs. (6) and (17) is equal to

$$w_{m,n} = \sum_{m',n'} [(\nabla_2 G(m - m', n - n')) \times (\rho^2_{m',n'} + \rho^2_{m',n'+1})A_{m',\hat{n}'} - (\nabla_1 G(m - m', n - n'))(\rho^2_{m',n'} + \rho^2_{m'+1,n'})A_{\hat{m}',n'}], \tag{31}$$

where

$$G(m - m', n - n') = \int_{-\pi}^{\pi} \frac{d^2k}{(2\pi)^2} \frac{e^{i\{k_x(m-m') + k_y(n-n')\}} - 1}{4 - 2\cos k_x - 2\cos k_y} \tag{32}$$

is the Green's function on the lattice and $\nabla_{1,2} f(\mathbf{r}) \equiv f(\mathbf{r} + \mathbf{e}_{1,2}) - f(\mathbf{r})$.

The set of equations (29)–(32) was numerically solved in [3, 4], where the function $N_{cr}(C)$ was calculated by using the found distributions. The line *b* in the figure displays this function. The compaction removed the divergence of the function $N_{cr}(C)$ at $C = C_{cr}$ and allowed us to perform the calculations in the range $1 \le C \le 2.83$. The field configurations were found to be qualitatively similar to those existing in the continuous case. However, the sign of the correlation interaction proved to be opposite to that in the continuous model. The position of the $N_{cr}(C)$ curve under the asymptotic line $N_{cr}(\infty)$ indicates that there is an universal correlation attraction between the field configurations in the system. This effect was found when the symmetry of the ground state was analyzed using the perturbation theory with $k \gg 1$ [25–27].

This phenomenon can be explained as follows. In the continuous limit, there is a competition between the bare NSE interaction and the Chern–Simons gauge interaction in its long-wave polynomial representation. Now, one more opponent of the bare NSE interaction—the gauge-field action on the dispersion—appears. This gauge-field effect reduces the derivatives of the function Ψ, so it also reduces the kinetic term in the Hamiltonian. Under the condition $H = 0$, this reduces the Ψ-field amplitude and, therefore, N_{cr}. In the long-wave approximation, a decrease in the Ψ-field amplitude in Eq. (10) at a constant H value can only be compensated by increasing the coupling constant g.

Expanding the operator $\Delta(A)$ in powers of derivatives, we find the term

$$\cos A_x \frac{\partial^2}{\partial x^2} + \cos A_y \frac{\partial^2}{\partial y^2} \tag{33}$$

describing the long-wave representation of Laplacian (27). It is seen from this term that several effects occur in the system. First, the finite gauge-field values make the coefficients appearing in Eq. (33) less than unity, i.e., they increase the mass of quasiparticles. Second, the nonzero gauge-field values in the multipliers in Eq. (33) form the field distribution $\rho_{m,n}$ with broken axial symmetry, which was confirmed by the numerical calculations. In this case, the relative change in the characteristic size of the soliton core of the field $\rho_{m,n}$ for $C \gtrsim 1$ is less than two percent. Because the maximum change $(N_{cr}(1) - N_{cr}(\infty))/N_{cr}(\infty)$ is also only a few percent, the addition to the coupling constant in the systems with an energy scale of about 1 eV is of the order of 100 K in physical units.

Chiral Modes

The problem of existence of the dimensional reductions of the generally nonintegrable problem (19)–(22) [28] and the solution of static equation (15) with the use of the method proposed in [22] and the Bäcklund transformation were discussed in detail in [29, 30]. Here, we only focus on some properties that are related to the features of exact solutions in the spatially one-dimensional systems.

The simplest one-dimensional integrable case [19] arises when all functions in Eqs. (19)–(22) depend on the combination $\xi = a_1 x + a_2 y$ of the coordinates x and y, where one of the constants a_1 and a_2 may be zero. Then, for, e.g., $a_1 = 1$ and $a_2 = \gamma$, the phase $\alpha(\xi, t)$ of the function $\Psi(\xi, t) = \rho(\xi, t)e^{-i\alpha(\xi, t)}$ can be introduced such that $\partial_\xi \alpha = (u + \gamma v)/(1 + \gamma^2)$ and $\partial_t \alpha = w - u^2 - v^2 + (u + \gamma v)/(1 + \gamma^2)$. In this case, the function $\Psi(\xi, t)$ will satisfy the (1 + 1)D NSE

$$i\frac{\partial \Psi}{\partial t} + (1 + \gamma^2)\frac{\partial^2 \Psi}{\partial \xi^2} = -2C|\Psi|^2\Psi, \tag{34}$$

which has the exact solution $\alpha(\xi, t) = r_0^2 t,$,

$$\begin{aligned} \rho &= \frac{r_0}{\cosh\dfrac{r_0\xi}{\sqrt{1+\gamma^2}}}, \quad v = \frac{r_0}{\sqrt{1+\gamma^2}}\tanh\frac{r_0\xi}{\sqrt{1+\gamma^2}}, \\ w &= r_0^2\left(\tanh^2\frac{r_0\xi}{\sqrt{1+\gamma^2}} - 1\right), \quad u = -\gamma v, \end{aligned} \tag{35}$$

where r_0 is the integration constant.

We analyze the properties of the one-dimensional chiral field configurations in the (1 + 1)D NSE model [31]

$$i\frac{\partial \Psi}{\partial t} = -\frac{1}{2}\frac{\partial^2 \Psi}{\partial x^2} - \lambda j \Psi, \tag{36}$$

where nonlinearity is represented by the current $j = \Im\Psi^*\partial_x\Psi$ rather that by the density $|\Psi|^2$, as in Eq. (34). By expressing the current density $j = \rho^2\partial_x\alpha$ in terms of the absolute value and the phase of the function $\Psi = \rho e^{i\alpha}$, we obtain the ordinary NSE, in which so-called coupling constant $g(x, t) = \lambda\partial_x\alpha$ is modulated due to a spatial change in the phase. For a traveling wave $\alpha(x, t) = \kappa x - \omega t$, the current density is $j = v\rho^2$, where $v \equiv \kappa$ so that $g = \lambda v$. It follows from the condition $g > 0$ for soliton existence that $v > 0$. Thus, the soliton

$$\Psi(x, t) = \frac{a}{\sqrt{\lambda v}\cosh[a(x - vt)]}e^{iv(x - ut)} \tag{37}$$

for which $a = v\sqrt{1 - 2u/v}$ and $u = \omega/\kappa$ is the phase velocity can only move rightwards, i.e., represents the chiral field distribution.

The factor $1/\sqrt{v}$ in Eq. (37) means that the soliton velocity should be positive. In particular, the soliton cannot be stopped. Because the velocity cannot be changed arbitrarily, the Galilei invariance is broken in this system.

The properties of the chiral edge modes with the linear dispersion law in a phenomenon such as the fractional Hall effect are described by using the Chern–Simons term in the Lagrangian. By applying a spatial reduction, let us demonstrate, following [31], that the model with the equation of motion (36) partially corresponds to the Chern–Simons model (1) without the term $g|\Psi|^4$. We assume that all fields in Eq. (1) are independent of the y coordinate and denote $A_y = B$. Then, Lagrangian (1) transforms into the Lagrangian of the B–F theory:

$$\begin{aligned} \mathcal{L}_{(1+1)} &= \frac{k}{2}B\varepsilon_{\mu,\nu}F_{\mu,\nu} + i\Psi^*(\partial_t + iA_0)\Psi \\ &\quad -\frac{1}{2}|(\partial_x + iA_x)\Psi|^2 - \frac{1}{2}B^2|\Psi|^2, \end{aligned} \tag{38}$$

where $F_{\mu,\nu} = \partial_\mu A_\nu - \partial_\nu A_\mu$, $x^\mu = \{t, x\}$, and $A_\mu = (A_0, A_x)$. Since this expression does not include the kinetic term for the fields B and A_μ, these fields can completely be removed by choosing the phase of the field Ψ. In this case, we obtain the Lagrangian of the system in which all interactions disappear [see Eq. (34)]. In order for the fields Ψ to interact with each other through the gauge fields, the potential A_μ and the field B should be made dynamical by adding the kinetic term of the field B to Eq. (38). Taking the Lagrangian $\mathcal{L}_B = \partial_t B \partial_x B$ [29], we obtain the sum $\mathcal{L}_B + \mathcal{L}_{(1+1)}$, which is equivalent to the Lagrangian

$$\mathcal{L} = i\Psi^*\partial_t\Psi - \frac{1}{2}\left|\left(\partial_x + i\frac{\lambda}{2}|\Psi|^2\right)\Psi\right|^2 \qquad (39)$$

with $\lambda = 2k^2$, where k is the coefficient in the Chern–Simons action. Variation of Eq. (39) leads to the equation of motion [31], which, after substituting $\Psi(x, t) \longrightarrow \exp\left\{i\frac{\lambda}{2}\int_0^x ds|\Psi(s, t)|^2\right\}\psi(x, t)$ and taking into account the continuity equation $\partial_t|\Psi|^2 + \partial_x j = 0$, coincides with Eq. (36) of the chiral model. In this case, the Galilei noninvariance obviously arises due to the term $\mathcal{L}_B$.

Conclusion

The function Ψ in the NSE models analyzed above has the meaning of the order parameter in the effective Ginzburg–Landau theory describing some coherent state [see Eqs. (16), (37)]. This function is a classical variable at distances $L \gtrsim \xi$ in strongly correlated planar lattice systems, where the spatial correlation scale ξ is larger than the lattice constant by only one order of magnitude. However, by calculating the momentum $P_i = \partial\mathcal{L}/\partial A_i$ in Eq. (1) and using the canonical Poisson bracket for the coordinate and momentum, one obtains the following Poisson bracket for the coordinates $X \equiv A_x$ and $Y \equiv A_y$ of the system:

$$\{X, Y\} = 1/k, \qquad (40)$$

which reflects the noncommutative geometry of the plane. Jackiw and Nair [32] discussed the physical consequences of this geometry and demonstrated that the second parameter in the two-parameter central extension of the Galilei group in (2 + 1) dimension is spin $s = 1/k$. Duval and Horváthy [33] also examined this effect by using Peierls substitution $\partial_\mu + iA_\mu \longrightarrow e^{\partial_\mu + iA_\mu}$ Eqs. (25)–(27) and Hall dynamics (21), (22).

In quantum theory, the Poisson bracket is replaced by a commutator and the gauge potential A_μ is a vector operator whose spatial components do not commute with each other in the general case because of Eq. (40). Therefore, the field A_μ can be treated as a classical variable only for the state for which the right-hand side of Eq. (40) is zero. This coherent state, which is characterized by a reconstructed equivalence between the x and y directions, was implied in this paper. The mechanism of canceling the right-hand side of the commutator of canonically conjugate quantities—the x and y components of the translation operators—by virtue of the contribution from the edge modes has been discussed by Chen *et al.* [34]. However, the details of this mechanism are still an open topical problem.

I am grateful to S.N. Vlasov, V.E. Zakharov, E.A. Kuznetsov, A.G. Litvak, and V.I. Talanov for stimulating discussions. This study was supported in part by the Russian Foundation for Basic Research, project no. 98-02-16237.

REFERENCES

1. L. A. Abramyan and A. P. Protogenov, Pis'ma Zh. Éksp. Teor. Fiz. **64**, 807 (1996) [JETP Lett. **64**, 859 (1996)].
2. L. A. Abramyan, V. I. Berezhiani, and A. P. Protogenov, Phys. Rev. E **56**, 6026 (1997).
3. L. A. Abramyan, V. A. Verbus, and A. P. Protogenov, Zh. Éksp. Teor. Fiz. **114**, 747 (1998) [JETP **87**, 408 (1998)].
4. L. A. Abramyan, A. P. Protogenov, and V. A. Verbus, Pis'ma Zh. Éksp. Teor. Fiz. **69**, 839 (1999) [JETP Lett. **69**, 887 (1999)].
5. A. G. Litvak, in *Review of Plasma Physics*, Ed. by M. A. Leontovich (Atomizdat, Moscow, 1980; Consultants Bureau, New York, 1986), Vol. 11, p. 10.
6. *Singularities in Fluids, Plasmas and Optics*, Ed. by R. E. Caflisch and G. C. Papanicolaou (Kluwer, Dordrecht, 1993), NATO ASI Ser., p. 404.
7. V. E. Zhakharov, Zh. Éksp. Teor. Fiz. **62**, 1745 (1972) [Sov. Phys. JETP **35**, 908 (1972)].
8. E. A. Kuznetsov and S. K. Turitsyn, Zh. Éksp. Teor. Fiz. **82**, 1457 (1982) [Sov. Phys. JETP **55**, 844 (1982)]; Zh. Éksp. Teor. Fiz. **94** (8), 119 (1988) [Sov. Phys. JETP **67**, 1583 (1988)].
9. S. C. Zhang, H. T. Hansson, and S. Kivelson, Phys. Rev. Lett. **62**, 82 (1989).
10. E. Fradkin, C. Nayak, A. Tsvelik, and F. Wilczek, Nucl. Phys. B **516**, 704 (1998); E. Fradkin, C. Nayak, and K. Schoutens, Nucl. Phys. B **546**, 711 (1999).
11. R. Jackiw and S. Y. Pi, Phys. Rev. Lett. **64**, 2969 (1990); **66**, 2682 (1991).
12. A. M. Polyakov, Mod. Phys. Lett. A **3**, 325 (1988).
13. T. Fukui and N. Kawakami, Phys. Rev. B **51**, 5239 (1995); cond-mat/9504118.
14. F. D. M. Haldane, Phys. Rev. Lett. **67**, 937 (1991).
15. R. Jackiw and S. Y. Pi, Phys. Rev. D **42**, 3500 (1990); Prog. Theor. Phys. Suppl. **107**, 1 (1992).
16. I. V. Barashenkov and A. O. Harin, Phys. Rev. Lett. **72**, 1575 (1994); Phys. Rev. D **52**, 2471 (1995).
17. G. Dunne, *Self-Dual Chern-Simons Theories* (Springer-Verlag, Berlin, 1995); Lect. Notes Phys. **36** (1995).
18. E. M. Lifshitz and L. P. Pitaevskiĭ, *Course of Theoretical Physics*, Vol. 5: *Statistical Physics* (Nauka, Moscow, 1978; Pergamon Press, New York, 1980), Part 2.
19. M. Knecht, R. Pasquier, and J. Y. Pasquier, J. Math. Phys. **36** (8), 4181 (1995).

20. V. I. Talanov, Sov. Radiophys. **9**, 260 (1966); S. N. Vlasov, V. A. Petrishchev, and V. I. Talanov, Radiophys. Quantum Electron. **14**, 1062 (1974).
21. L. Bergé, A. de Bouard, and J. C. Saut, Phys. Rev. Lett. **74**, 3907 (1995).
22. J. Weiss, M. Tabor, and G. Carnevale, J. Math. Phys. **24**, 522 (1983); J. Weiss, J. Math. Phys. **24**, 1405 (1983).
23. L. D. Faddeev, *How Algebraic Bethe Ansatz Works for Integrable Model*, Les-Houches Lectures; hep-th/9605187.
24. P. B. Wiegmann and A. V. Zabrodin, Phys. Rev. Lett. **72**, 1890 (1994).
25. Ya. I. Kogan, Pis'ma Zh. Éksp. Teor. Fiz. **49**, 194 (1989) [JETP Lett. **49**, 225 (1989)].
26. Ya. I. Kogan and I.V. Polubin, Pis'ma Zh. Éksp. Teor. Fiz. **51**, 496 (1990) [JETP Lett. **51**, 560 (1990)].
27. D. V. Khveshchenko and Ya. I. Kogan, Pis'ma Zh. Éksp. Teor. Fiz. **50**, 137 (1989) [JETP Lett. **50**, 152 (1989)]; Mod. Phys. Lett. B **4**, 95 (1990).
28. D. Lévy, L. Vinet, and P. Winternitz, Ann. Phys. **230**, 101 (1994).
29. U. Aglietti, L. Griguolo, R. Jackiw, *et al.*, Phys. Rev. Lett. **77**, 4406 (1996).
30. P. A. Horvathy and J.-C. Yera, Phys. Rev. D **54**, 4171 (1996).
31. R. Jackiw, J. Non. Lin. Math. Phys. **4**, 241 (1997).
32. R. Jackiw and V. P. Nair, hep-th/0003130.
33. C. Duval and P. A. Horváthy, hep-th/0002233.
34. Y. H. Chen, F. Wilczek, E. Witten, and B. I. Halperin, Int. J. Mod. Phys. B **3**, 1001 (1989).

Translated by R. Tyapaev